

AD-A055 884

PHOTOMETRICS INC LEXINGTON MASS
ASSESSMENT AND EVALUATION OF SIMULATION DATA.(U)
NOV 77 I L KOFSKY, D P VILLANUCCI, G DAVIDSON

F/G 4/1

UNCLASSIFIED

PHM-01-78

DNA-4303F

DNA001-77-C-0208

NL

1 OF 2
ADA
0558 84



AD A 055884

FOR FURTHER TRANSMISSION

AD-E300 220
5/18

(18) DNA 4303F
SBIE

(19) AD-E300 220

**ASSESSMENT AND EVALUATION
OF SIMULATION DATA.
HAES REPORT No. 69**

(12) B.31

PhotoMetrics, Inc.
442 Marrett Road
Lexington, Massachusetts 02173

(14) PHM-01-78, DNA-HAES-69

DDC FILE COPY

(11) 15 Nov 1977

(12) 135 p.

Final Report, ~~dated~~ 1 March 1977 - 15 October 1977,

(9)

CONTRACT No. DNA 001-77-C-0208

(15)

I. h. / Kofsky,
D. P. / Villanucci
G. / Davidson

APPROVED FOR PUBLIC RELEASE;
DISTRIBUTION UNLIMITED.

THIS WORK SPONSORED BY THE DEFENSE NUCLEAR AGENCY
UNDER RDT&E RMSS CODE B322077462 25AAXY X96003 H2590D.

Prepared for
Director
DEFENSE NUCLEAR AGENCY
Washington, D. C. 20305

(16) X960
DDC
RECEIVED
JUL 3 1978
B

388 596

not

Destroy this report when it is no longer
needed. Do not return to sender.



UNCLASSIFIED

SECURITY CLASSIFICATION OF THIS PAGE (When Data Entered)

REPORT DOCUMENTATION PAGE		READ INSTRUCTIONS BEFORE COMPLETING FORM
1. REPORT NUMBER DNA 4303F	2. GOVT ACCESSION NO.	3. RECIPIENT'S CATALOG NUMBER
4. TITLE (and Subtitle) ASSESSMENT AND EVALUATION OF SIMULATION DATA HAES Report No. 69	5. TYPE OF REPORT & PERIOD COVERED Final Report for Period 1 Mar 77—15 Oct 77	
	6. PERFORMING ORG. REPORT NUMBER PhM-01-78	
7. AUTHOR(s) I. L. Kofsky D. P. Villanucci G. Davidson	8. CONTRACT OR GRANT NUMBER(s) DNA 001-77-C-0208 <i>New</i>	
9. PERFORMING ORGANIZATION NAME AND ADDRESS PhotoMetrics, Inc. 442 Marrett Road Lexington, Massachusetts 02173	10. PROGRAM ELEMENT, PROJECT, TASK AREA & WORK UNIT NUMBERS NWET Subtask I25AAXYX960-03	
11. CONTROLLING OFFICE NAME AND ADDRESS Director Defense Nuclear Agency Washington, D.C. 20305	12. REPORT DATE 15 November 1977	
	13. NUMBER OF PAGES 140	
14. MONITORING AGENCY NAME & ADDRESS (if different from Controlling Office)	15. SECURITY CLASS (of this report) UNCLASSIFIED	
	15a. DECLASSIFICATION/DOWNGRADING SCHEDULE	
16. DISTRIBUTION STATEMENT (of this Report) Approved for public release; distribution unlimited.		
17. DISTRIBUTION STATEMENT (of the abstract entered in Block 20, if different from Report)		
18. SUPPLEMENTARY NOTES This work sponsored by the Defense Nuclear Agency under RDT&E RMSS Code B322077462 I25AAXYX96003 H2590D.		
19. KEY WORDS (Continue on reverse side if necessary and identify by block number) Nuclear-Effects Simulation Radiation Transport Photometry of Aurora Excitation of Air Infrared Radiation Upper Atmosphere <i>microns</i>		
20. ABSTRACT (Continue on reverse side if necessary and identify by block number) Radiance data from the charged particle-stimulated ionosphere in the wave- length band 4.2-4.3 μm (from ICECAP/HAES multi-instrumented rocket A18.219-1, 1974) are evaluated; the performance of two diagnostic photo- meter systems flown on sounding rockets is assessed; a procedure for determining pointing relative to prompt and past air excitation of a rocket- borne interferometric spectrometer (on IC630.02-1A (HIRIS II), 1976) is developed; and photometry and positioning data for 1976 aircraft flights at <i>ova</i>		

UNCLASSIFIED

C 02(11)

SECURITY CLASSIFICATION OF THIS PAGE(When Data Entered)

20. ABSTRACT (Continued)

auroral latitudes to measure spatial structure in infrared radiance are presented.

The radiation flux near 4.3 ^(microns) μm at low elevation angles, ^(approximately 5-15 deg) ($\sim 5^\circ - 15^\circ$) has both layering irregularities and a component associated with prompt energy deposition in the atmosphere. The altitude structure is interpreted as an effect of adding collisional transfer of N_2 vibrational energy excited by aurora-producing particles to the population of CO_2 by transport of thermal radiation. Aeronomic mechanisms that could be responsible for the near-prompt infrared mechanism are reviewed critically, and further measurements to select among these processes and to identify the radiating molecular species are suggested.

A photometer with wavelength response designed to simulate that of calibrated photographic cameras, such as were used to image the glows from past nuclear explosions, is found to perform essentially as expected. One intended to determine column intensity in the weak $\text{N}^2\text{D} - ^2\text{S}$ doublet requires further modification. Zenith radiances from AFGL/DNA's NKC-135 aircraft in five auroral-emission features, two (or three) of which are applied in determining the altitudes at which energy is deposited, are presented for eight aircraft missions in which the spatial variations (and spectral distribution) of radiation near $2.8 \mu\text{m}$ were measured by instruments coaligned with the multichannel photometer.

ACCESS	
NTIS	DTIC SERVICE <input checked="" type="checkbox"/>
DDC	DTIC SERVICE <input type="checkbox"/>
UNCLASSIFIED	<input type="checkbox"/>
DISTRIBUTION/AVAILABILITY CODES	
IF	AVAIL. and/or SPECIAL
A	

UNCLASSIFIED

SECURITY CLASSIFICATION OF THIS PAGE(When Data Entered)

SUMMARY

The objective of the program reported here is to assess and evaluate in terms of nuclear explosion-induced sky backgrounds, optical/infrared radiation data from DNA-sponsored measurements on the disturbed auroral ionosphere. Six individual topics, involving observations of emission near $4.3\mu\text{m}$ and assessments of energy input that resulted in emissions at $2.8\mu\text{m}$ and in the spectral band $4\text{-}22\mu\text{m}$, are considered.

Altitude profiles of radiation density in the $4.2\text{-}4.3\mu\text{m}$ band at low elevation angles when the ionosphere is bombarded by charged particles, which are unique to HAES-ICECAP rocket A18.219-1 (1974), are presented and partially evaluated in Section I. Substantial layering (altitude irregularity) of the radiant flux in the disturbed region is observed. Section II reviews potential sources of the largely-unexpected prompt fluorescence-associated component of the atmosphere's radiation in this wavelength band, and suggest further field investigations to determine its origin. The internal consistency of these $4.3\mu\text{m}$ radiance and instrument-pointing data is evaluated critically.

Section III assesses the performance of a photometer designed to measure in the wavelength band over which photographic cameras using panchromatic film are sensitive. This Film Response Photometer provides a link between the infrared radiant intensities resulting from excitation by naturally-occurring energetic charged particles and those from particles and photons output by nuclear explosions. A similar evaluation of a dual channel differential photometer intended to measure column-concentrations of the NO^{\ddagger} precursor species N^2D is in Section IV. The former instrument is found to behave about as expected, and the latter requires modification if it is to perform effectively.

Procedures for determining pointing of the high resolution infrared ($4\text{-}22\mu\text{m}$) spectrometer HIRIS II on rocket IC630.02-1A (01 Apr 76) against the dynamically-excited auroral ionosphere are presented in Section V. Section VI, with Appendixes I and II, lists auroral characterization and aircraft positioning data for the eight ICECAP 1976 missions of NKC-135 A/C 55-3120 in which spatial variations of the upper atmosphere's radiance at wavelengths near $2.8\mu\text{m}$ were measured.

PREFACE

The High Altitude Effects Simulation (HAES) Program sponsored by the Defense Nuclear Agency since the early 1970 time period, comprises several groupings of separate, but interrelated technical activities, e. g., ICECAP (Infrared Chemistry Experiments - Coordinated Auroral Program). Each of the latter have the common objective of providing information ascertained as essential for the development and validation of predictive computer codes designed for use with high priority DoD radar, communications, and optical defensive systems.

Since the inception of the HAES Program, significant achievements and results have been described in reports published by DNA, participating service laboratories, and supportive organizations. In order to provide greater visibility for such information and enhance its timely applications, significant reports published since early calendar 1974 shall be identified with an assigned HAES serial number and the appropriate activity acronym (e. g., ICECAP) as part of the title. A complete and current bibliography of all HAES reports issued prior to and subsequent to HAES Report No. 1 dated 5 February 1974 entitled, "Rocket Launch of an SWIR Spectrometer into an Aurora (ICECAP 72)," AFCRL Environmental Research Paper No. 466, is maintained and available on request at DASLAC, DoD Nuclear Information and Analysis Center, 816 State Street, Santa Barbara, California 93102, Telephone: (805) 965-0551.

This report, which is the final report on Contract DNA001-77-C-0208 and No. 69 in the HAES series, covers PhotoMetrics' activities in accessing and evaluating field data on infrared backgrounds in the period 01 Mar - 15 Oct 1977. It makes frequent reference to procedures developed for accessing data from sounding rockets and flights of instrumented aircraft at high latitudes, preliminary results, and comparison material on ICECAP investigations other than those reported here, contained in our previous HAES reports 4, 27, and 59 (Ref's 1, 2, and 3).

In addition it applies information recently derived from simulations of the effects of nuclear explosions in exciting atmospheric radiations that was presented at the HAES Infrared Data Review held in Falmouth, MA 13 - 15 Jun 77 (Ref 4). Considered in the report are data from the following HAES-ICECAP sources -

Multi-instrumented rocket A18.205-1, 27 Mar 73

Multi-instrumented rocket A18.219-1, 25 Feb 74

Multi-instrumented rocket IC519.07-1B, 22 Mar 75

Interferometric spectrometer-carrying rocket
IC630.02-1A(HIRIS II), 01 Apr 76

USAF NKC-135A 55-3120 (Air Force Geophysics
Laboratory's IR-Optical Flying Laboratory)
aircraft missions between 22 Feb and 28 Mar 76,
performed under program heading ICECAP 76.

This work was under the direction of I. L. Kofsky, to whom questions about it should be addressed. D. A. Gentile contributed to the photoreproduction and artwork, and Mrs. C. A. Rice was responsible for typing the manuscript. Supporting information was provided by many of the staff of the Air Force Geophysics Laboratory's OPR branch, in particular J. Kennealy and P. Doyle, and by T. C. Degges of Visidyne, Inc. The flight logs in Appendix II were prepared by J. Reed of Visidyne. The authors gratefully acknowledge the support and encouragement of A. T. Stair, Jr., and J. C. Ulwick of AFGL and of C. A. Blank of the Defense Nuclear Agency.

TABLE OF CONTENTS

SECTION		PAGE
	SUMMARY	1
	PREFACE	2
I	4.3 μ m RADIATION PROFILES AT LOW ELEVATION ANGLES	11
	INTRODUCTION	11
	INSTRUMENT ELEVATION AND AZIMUTH - GENERAL	13
	CORRECTION OF EL-AZ.....	14
	EFFECT OF THE ELEVATION ANGLE CORRECTION ON INTERPRETATION OF 2.8 μ m RADIANCE DISTRIBUTIONS	24
	RADIATION PROFILES	25
	LAYERING OF THE RADIANCE PROFILES	38
II	CORRELATED 4.3 μ m FEATURE NEAR GEOMAGNETIC WEST	43
	NEAR-PROMPT 4.3 μ m EMISSION	43
	CORRELATION WITH ALL-SKY AND MERIDIAN SCANNING PHOTOMETER DATA....	43
	CORRELATION WITH 5199 \AA PHOTOMETER DATA..	49
	DISCUSSION OF SOURCES OF 4.3 μ m EMISSIONS	49
	CONCLUSION	53
III	FILM RESPONSE PHOTOMETER, IC519.07-1B.....	55
	FUNCTION	55
	INSTRUMENT CHARACTERISTICS	55
	ANTICIPATED RESPONSE OF THE FRP.....	57
	ROCKET TRAJECTORY AND ORIENTATION.....	58
	COMPARISON TO N ₂ ⁺ FIRST NEGATIVE (0,0) BAND FLUORESCENT RADIANCE	60
	EFFECT OF OI GREEN LINE EMISSION	66
	SUMMARY, APPLICATION TO USE OF THE FRP ON AIRCRAFT	69
IV	N ₂ ^D DIFFERENTIAL PHOTOMETER, A18.219-1.....	71
	FUNCTION	71
	SPECTRAL SENSITIVITY OF THE PHOTO- METER AND DISTRIBUTION OF THE SOURCE	72
	PROCEDURE FOR EVALUATION OF FLIGHT DATA	77

TABLE OF CONTENTS (continued)

SECTION	PAGE
	EVALUATION FOR SYNTHETIC-SPECTRUM
	MODELS 82
	CONCLUSIONS 85
V	HIRIS VIEWING GEOMETRY 87
	AURORAL CONDITIONS, POINTING REQUIREMENT 87
	ROCKET POINTING GEOMETRY 88
	AURORAL-EXCITATION INTERCEPTS 92
VI	AURORAL INTENSITIES, ICECAP 76
	AIRCRAFT PROGRAM 98
	INTRODUCTION 98
	DATA, APPLICATION 98
	REDUCTION PROCEDURE 101
	REFERENCES 105
	APPENDIX
I	AURORAL RADIANCES, ICECAP 76
	AIRCRAFT MISSIONS 107
II	POSITION AND HEADING OF ICECAP 76
	AIRCRAFT 129

LIST OF ILLUSTRATIONS

<u>Figure</u>		<u>Page</u>
1	Elevation-azimuth plot for the side-looking photometers and radiometers after stabilization of A18. 219-1	12
2	4. 3 μ m radiometer azimuth-elevation spin cycles near 111 and 102 km on downleg of A18. 219-1, showing the van Rhijn-like, cyclically-varying radiance	16
3	Plots of 4. 3 μ m radiance against cosec of elevation angle of the radiometer's axis as a function of shift in the elevation-azimuth scales, for rocket altitudes between 116 and 103 km, A18. 219-1 downleg	18
4	Summary of plots of 4. 3 μ m radiance against cosec of elevation angle of radiometer's axis applying an 85° shift in elevation-azimuth scales, A18. 219-1 downleg	21
5	Radiance distribution in wide-band channel of 5199 Å differential photometer, averaged over 10 spin cycles of A18. 219-1 near 190 km altitude in the range of (uncorrected) geographic azimuths 305°-286°	22
6	Altitude profiles of 4. 3 μ m radiance measured at 30° azimuth intervals by the sidelooking radiometer on downleg of A18. 219-1, with comparison upleg data for 120° and 210° geomagnetic azimuth.	26
7	Near-zenith altitude profiles of 4. 3 μ m and 3914 Å radiance measured by the axial-pointing instruments on upleg and downleg of A18. 219-1	32
8	Altitude profiles of 4. 3 μ m and 3914 Å radiance at three azimuths-elevations, A18. 219-1 downleg	34
9	4. 3 μ m az-el radiance distribution on downleg spin cycle 733 of A18. 219-1, showing the sharp discontinuity starting at 371.88 sec	36

LIST OF ILLUSTRATIONS (continued)

<u>Figure</u>		<u>Page</u>
10	Transfer characteristics of A18.219-1's sidelooking $4.3\mu\text{m}$ radiometer as determined from the data printout in the time period 365.4 to 368.5 sec, and interpolated from Spin 723	37
11	Azimuth dependence of excess $4.3\mu\text{m}$ signal above an interpolated altitude profile between 106 and 111 km rocket altitude, A18.219-1 downleg	39
12	Altitude profiles of the fractional increase above an interpolated $4.3\mu\text{m}$ intensity profile near 109 km rocket altitude, A18.219-1 downleg	40
13	A comparison between 3914 \AA , 5577 \AA , $2.8\mu\text{m}$, and $4.3\mu\text{m}$ radiances for Spin 721 on downleg of A18.219-1.	44
14	Detail of region near 260° geomagnetic azimuth for Spin 721 on downleg of A18.219-1 showing the correlation between 3914 \AA and the $4.3\mu\text{m}$ "bump." Also shown are the angular response functions of the two instruments	45
15	Comparison between 3914 \AA and $4.3\mu\text{m}$ radiances for region near 260° geomagnetic azimuth at various altitudes on downleg of A18.219-1	46
16	Fort Yukon all-sky camera photograph at 368 seconds after launch of A18.219-1 with the position of the rocket indicated. Also shown is the Poker Flat meridian scanning photometer data at 362 seconds	48
17	Comparison between 5199 \AA channel at 118 km and the $4.3\mu\text{m}$ channel at 94 km on downleg of A18.219-1	50
18	Emission spectra calculated and approximated for the fundamental of NO^+ with equal populations of $v = 0 - 10$ and $\text{NO}^+(1,0)$ only, CO_2 for the $(001,000)$ and $(002,001)$ transitions, and the $\text{N}^{14}\text{N}^{15}(1,0)$ transition. Also shown is the spectral response characteristic of the $4.3\mu\text{m}$ radiometer	52

LIST OF ILLUSTRATIONS (continued)

<u>Figure</u>		<u>Page</u>
19	Relative photon response of the Film Response Photometer compared to that of Eastman Kodak Tri-X Pan film used with a fast wide-angle lens.	56
20	Trajectory of IC519.07-1B with estimated location of the "center" (marked +) and north-south extent of the diffuse auroral arc.	59
21	Representative 3914 Å and FRP elevation-azimuth scans from upleg of IC519.07-1B, showing qualitative correlation of the two radiance distributions.	61
22	Altitude profiles of peak intensities in the east and west limb, geomagnetic azimuth angles of the peaks and elevation angle of the sidelooking photometers at 0° geomagnetic azimuth, IC519.07-1B upleg.	62
23	Scatter plot of 3914 Å and FRP limb peak intensities (background included), with a least squares fit to the 3914 Å readings, IC519.07-1B.	64
24	Scatter plot of 3914 Å and FRP intensities (background included) at 10° azimuth intervals over three 360° spin cycles of IC519.07-1B on upleg, with least squares fits.	65
25	Altitude profiles of FRP/3914 Å limb peak intensities, and FRP/(weighted sum of 5577 Å and N ₂ ⁺ fluorescence) as defined in the text, IC519.07-1B.	67
26	Scatter plot of 5577 Å and 3914 Å limb peak intensities (background included), with a least squares fit to the 3914 Å readings.	68
27	Transmission of the filters in the differential photometer (at normal incidence), and spectra of the N ₂ ⁺ D-S doublet and N ₂ ⁺ First Negative (0, 3) band.	73
28	Synthetic auroral spectrum in the wavelength region 5100-5300 Å.	76

LIST OF ILLUSTRATIONS (continued)

<u>Figure</u>		<u>Page</u>
29	Representative 3914 Å and differential photometer elevation-azimuth scans, A18.219-1 upleg	78
30	Altitude profiles of air fluorescence and signal levels of the two channels of the N ⁺ D differential photometer at 330° magnetic azimuth, A18.219-1 upleg.	79
31	Trajectory of HIRIS II (IC630.02-1A) projected into the meridian plane through PKR, with altitude ranges over which the axially mounted interferometric spectrometer points into the upper and lower hemispheres.....	89
32	Projection of IC630.02-1A's long axis onto a horizontal plane for Rotation 1; 96 to 116 km	90
33	Altitude profiles of elevation and azimuth angles of IC630.02-1A's spectrometer on upleg and downleg.	93
34	Spectrometer pointing into the upper hemisphere at 106.0 sec (100.0 km, Rotation 1) with approximate intensities in the meridian plane from PKR of the bright arc to the S and diffuse aurora to the N	95
35	Ratio of column intensities of the OI 6300 Å line to the N ₂ ⁺ First Negative (0, 1) band, ICECAP 76-5	102
36	Scatter plot of N ₂ ⁺ First Negative fluorescence intensities, with a least-squares fit to the 4278 Å data from the multi-channel photometer.	103

LIST OF TABLES

<u>Table</u>		<u>Page</u>
1	Air Fluorescence Bands Near 5199 Å	75
2	Differential Photometer and Air Fluorescence Data for Table 3	80
3	Calculated N ² D and Background Intensities from Synthetic-Spectra Models	83
4	Times/Altitudes of Zero, Maximum, and Mini- mum Elevation Pointing Angle of IC630.02-1A	91
5	Examples of Spectrometer Pointing Into the Upper and Lower Hemispheres With and Without Aurora Present, IC630.02-1A	96
6	Reports on ICECAP Aircraft Measurements	99

SECTION I

4. $3\mu\text{m}$ RADIATION PROFILES AT LOW ELEVATION ANGLES

INTRODUCTION

This Section presents and provides a preliminary interpretation of altitude profiles of radiance of the auroral particle-excited ionosphere in the $4.21 - 4.305\mu\text{m}$ full-width-to-half-maximum-response (FWHM) wavelength band, measured at elevation angles $\sim 5^\circ - 15^\circ$ by the sidelooking filter radiometer on ICECAP multi-instrumented rocket A18.219-1 (launched from Poker Research Range on 25 Feb 74). The data from this rocket probe constitute the only available coherent set characterizing the disturbed atmosphere's " $4.3\mu\text{m}$ " radiance distribution at these low elevation angles and long radiating path lengths.

Spectral response of the radiometer and the spectrum of the optically-grey-to-thick (001-000) band of CO_2 , which dominates the signal (refer to the discussion in Ref 5), are in Fig 18 of Section II. The radiometer's field of view is about 6° circular (its angular sensitivity is that plotted in the left-hand diagram of Fig 20 of Ref 3). Rocket spin rate is 2.0 revolutions/sec. A major adjustment in the angles at which the instruments point within the radiating volume is derived in the following subsections, and other corrections that were applied to the $4.3\mu\text{m}$ data are described in the text. The effect of this change in elevation angles on interpretation of data from the $2.42 - 4.311\mu\text{m}$ (FWHM) sidelooking radiometer on the same rocket is briefly noted.

A preliminary review of some of these A18.219-1 data, with one comparison of altitude profiles measured on upleg and downleg (where the radiance levels are substantially higher), appears in Ref 3, p104 ff. An evaluation of the increases in the sidelooking $4.3\mu\text{m}$ -band radiometer signals closely associated with auroral excitation, which do not impact significantly the radiance profiles presented in this Section, is the subject of Section II of this report.

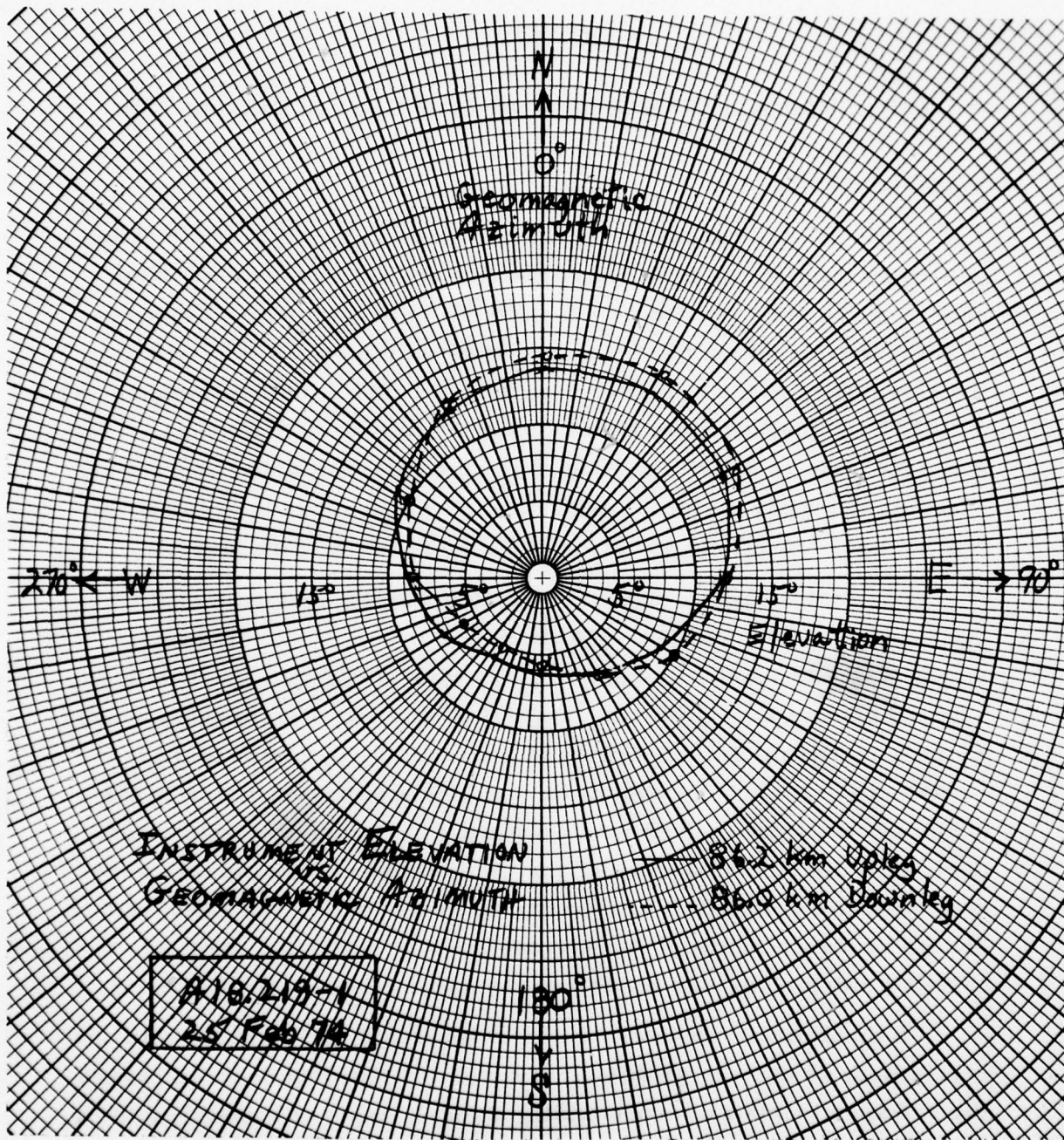


Figure 1. Elevation-azimuth plot for the side-looking photo-meters and radiometers after stabilization of A18.219-1.

INSTRUMENT ELEVATION AND AZIMUTH - GENERAL

We establish first the directions in which the set of sidelooking radiometers and photometers on A18.219-1- was pointing. The original data on rocket orientation, as noted in our previous report (Ref 3), were inconsistent with the expected projection on the instruments' fields of view of the auroral arc's known geometry. A 60° offset in the readings from the rocket's gyro system was tentatively identified by the rocket housekeeping group, which places geomagnetic N at 89° on the geographic-azimuth scales (as for example in Fig 34 of Ref 3). Our preliminary reduction of A18.219-1 data assumed that the elevation angles reported by the rocket group needed no such correction. While errors in the instruments' elevation angle have only secondary effect on our findings about aurora-associated emission near $2.8\mu\text{m}$ (Sections I and II of Ref 3), accurate pointing is needed to understand the spatial distribution of excitation of the incoming charged particles, ranges to and thus altitudes of emitting regions, $2.8\mu\text{m}$ -band backgrounds at the lower rocket altitudes, and particularly, the dependence on elevation angle of the disturbed atmosphere's radiance in the $4.3\mu\text{m}$ -filter band. (Elevation-azimuth is henceforth abbreviated as *el-az*.)

El-az data in the aspect report (Ref 6), however, indicate that any phase shift applied to the azimuth scale must be applied also to the elevation scale. Specifically, the information on zenith angle of the rocket's long axis and its azimuth with respect to true N, whose accuracy is not in question, fixes the azimuths of maximum and minimum elevation of the sidelooking instruments. As an example, near 85 km on upleg the tilt of the rocket axis from vertical is $5\frac{1}{2}^\circ$ at geographic azimuth 231° , and therefore the instruments (which point 80° from the spinning rocket's axis) will have a minimum *el* of $4\frac{1}{2}^\circ$ where their *az* is 231° , and a maximum of *el* of $15\frac{1}{2}^\circ$ near 51° *az*; refer to Fig 1. The telemetered *el-az* data show that both scales must be shifted together to maintain these minimum and maximum elevations at the expected azimuth angles. A corrected version of Ref 3's Fig 33

(Fig 1) shows the instruments' pointing after stabilization is achieved, for the 90° azimuth shift that we determine here. Shifting the el -az scales together results in an almost complete reversal of the high and low elevation angles.

CORRECTION OF EL-AZ

We applied three procedures for determining quantitatively the offset in the elevation-azimuth scales, results from which were in very good agreement.

Our first efforts were directed toward comparing visible-radiance distributions resulting from the geometry of the rocket and arc to those from the 1973 multi rocket probe (A18.205-1). Launch azimuths of the two rockets were nearly the same and zenith angles of their long axes were within $2\frac{1}{2}^\circ$ after stabilization, and an arc lay to the N on upleg of each trajectory. Therefore the sidelooking A18.219-1 instruments on upleg pointed at the arc at elevation angles not substantially different from those of A18.205-1 (compare, for example, Fig 1 with Fig 23 of Ref 2), although since the ranges to the excited air volumes are not the same the intercept altitudes of the fields of view would be expected to differ.

In the 1973 measurements the azimuth angles east and west of the geomagnetic meridian at which the arc limb enhancements maximized differ from one another by only 10° to 15° (even after the rocket had penetrated the arc); typical angles were 73°E and 63°W (see Fig 2 of Ref 3). In the 1974 measurements, on the other hand, this azimuth difference is $\sim 50^\circ$ even after a 60° shift was applied to the azimuth scales (see Fig 34 of Ref 3). That is to say, from A18.219-1 the angular positions of the van Rhijn-like enhancements are offset relative to magnetic N. The argument that the maxima should be symmetric about the meridian does not locate the meridian with good resolution, since the azimuth angles at which the limb brightnesses peak depend on the arc's E-W alignment and excitation uniformity as well as on

the elevation angles at which the instruments view the emitting volume. Considering the apparent E-W uniformity of the arc on rocket upleg, however, it does indicate that the azimuth must be shifted by more than 60° to make the data consistent with the known viewing geometry. (An 85° shift would restore symmetry to the limb peak azimuths.)

A second, potentially more accurate method of assessing the offset is to fit the elevation angle dependence of the $4.3\mu\text{m}$ atmospheric radiance to that expected from a simplified layer-thickness model, such as we adopted in evaluating the 1973 multi's $5.3\mu\text{m}$ radiometer data (Fig 21 of Ref 3). The rocket spin-correlated cyclical radiance variation observed at $5.3\mu\text{m}$ (Fig 23 of Ref 3) is a result of a convolution of the radiometer's (broad) field of view with the altitude profile of earth limb radiance. A plot of this background intensity against the (path length-proportional) cosecant of the radiometer axis' elevation angle (Fig 21 Ref 3) showed that at a fixed rocket altitude, the $5.3\mu\text{m}$ signal increases about linearly with effective path length through the atmosphere.

Although the atmosphere is not optically thin to radiation in the $4.3\mu\text{m}$ band at the lower rocket altitudes and elevation angles, roughly-similar cyclical background variations correlated with the path lengths might be expected. (A simple manifestation of this effect is that the maximum radiance, in the absence of any azimuthal dependences induced by localized dosing that increases "anisotropically" the vibrational temperature of the CO_2 molecules responsible for most of the $4.3\mu\text{m}$ radiation, would be located at the minimum elevation angle.) The $e\ell$ -az scans from 111 and $102\frac{1}{2}$ km (Fig 2) illustrate such van Rijn-like cyclical radiance distributions, with greater fractional modulation at the higher rocket altitude where fewer of the rotational lines from distant CO_2 molecules in the field of view are reabsorbed. (The ratio (peak - trough)/(peak + trough) is a factor 2 higher at the higher altitude.)

To implement this approach, we plotted the radiances from $e\ell$ -az scans at three rocket altitudes on downleg against the cosecant of the

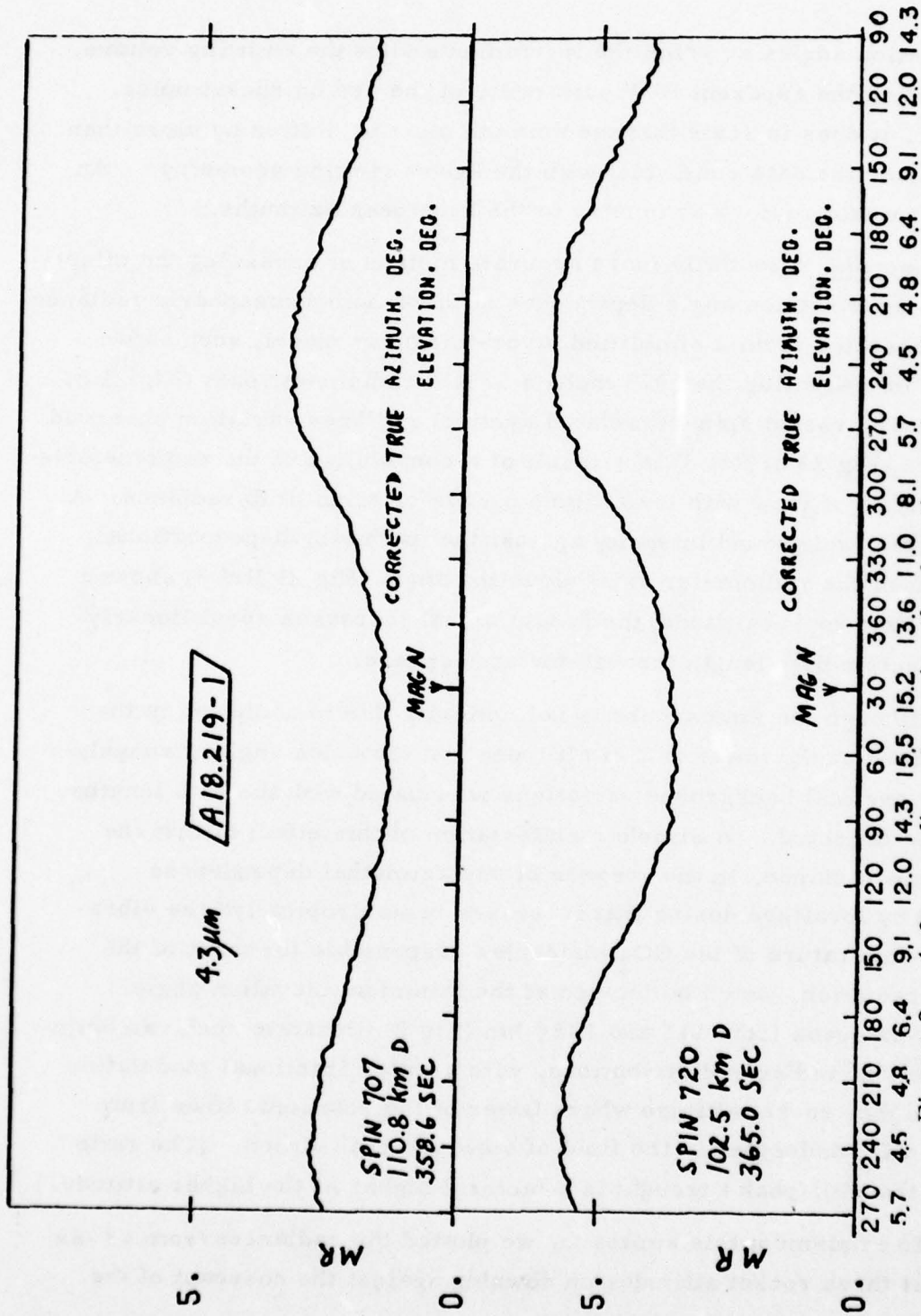


Figure 2. 4.3 μm radiometer azimuth-elevation spin cycles near 110 and 102 km on downleg of A18.219-1, showing the van Rhijn-like, cyclically-varying radiance.

radiometer axis' elevation angle, for shifts between 0° and 120° in the azimuth scale (Fig's 3a-c). The plots fail to close because of the increase in the atmosphere's radiance over the ~ 0.65 km altitude decrease during the 1/2-sec spin cycle; this increase is 6% near 103 km, for example. An azimuth shift of $87^\circ \pm 5^\circ$ best reproduces the expected dependence on elevation angle (recall that we have assumed no azimuthal dependence).

The $4.3\mu\text{m}$ radiance varies about linearly with atmospheric path length at the higher instrument elevation angles and rocket altitudes in Fig 3; conversely, at 103 km the curve "bows over" as more rotational lines become optically thick. This behavior is in qualitative agreement with the known transport of CO_2 radiation near $4.3\mu\text{m}$ in this altitude range (Ref 5). It is further shown in a summary of plots for rocket altitudes between 98 and 116 km (Fig 4), which apply an 85° offset in the azimuth-dependent change in elevation angles. As the altitude of observation decreases the path length dependence becomes less linear, and the onset of the "bow" moves to higher elevation angles.

A third, and most compelling, piece of evidence about the instrument pointing is provided by a narrow ($\sim 5^\circ$ FWHM) feature which appears in el - az scans of both channels of the N^2D differential photometer (Section IV) during most of the upleg and downleg segments of A18.219-1's trajectory. We have determined that the excess signal, which is located near 295° azimuth on the uncorrected plots, is caused by the -1.6 magnitude star Sirius (α Canus Majoris) passing through the 5° field of view of the photometer. The general appearance of its field-convolved angular distribution of radiance is shown in Fig 29 of Section IV. Both the celestial coordinates of and irradiance from Sirius verify this identification, as we show from an assessment of the photometer data from a region of downleg near 190 km rocket altitude, where the auroral signal is low.

Narrative text continues on page 22.

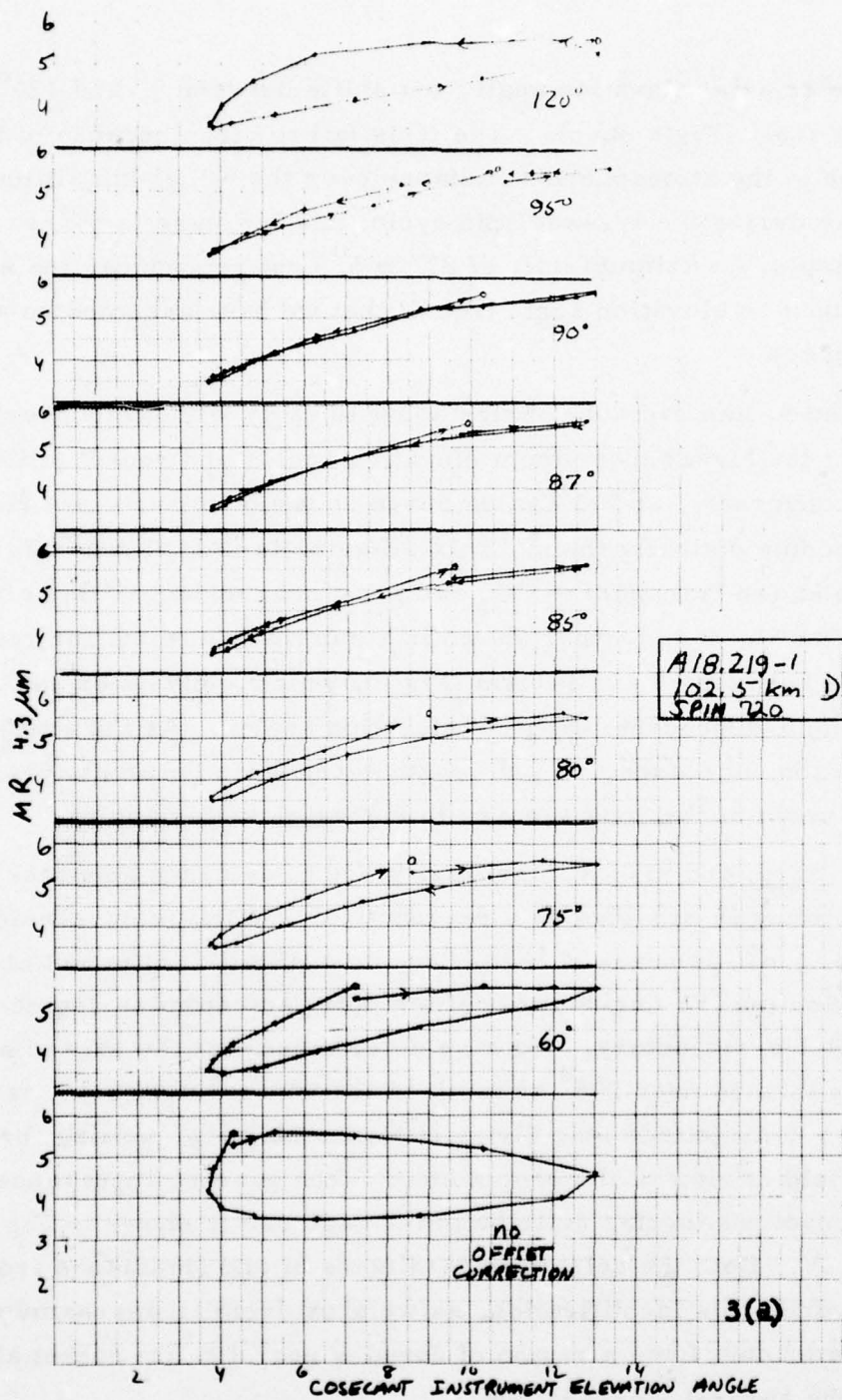
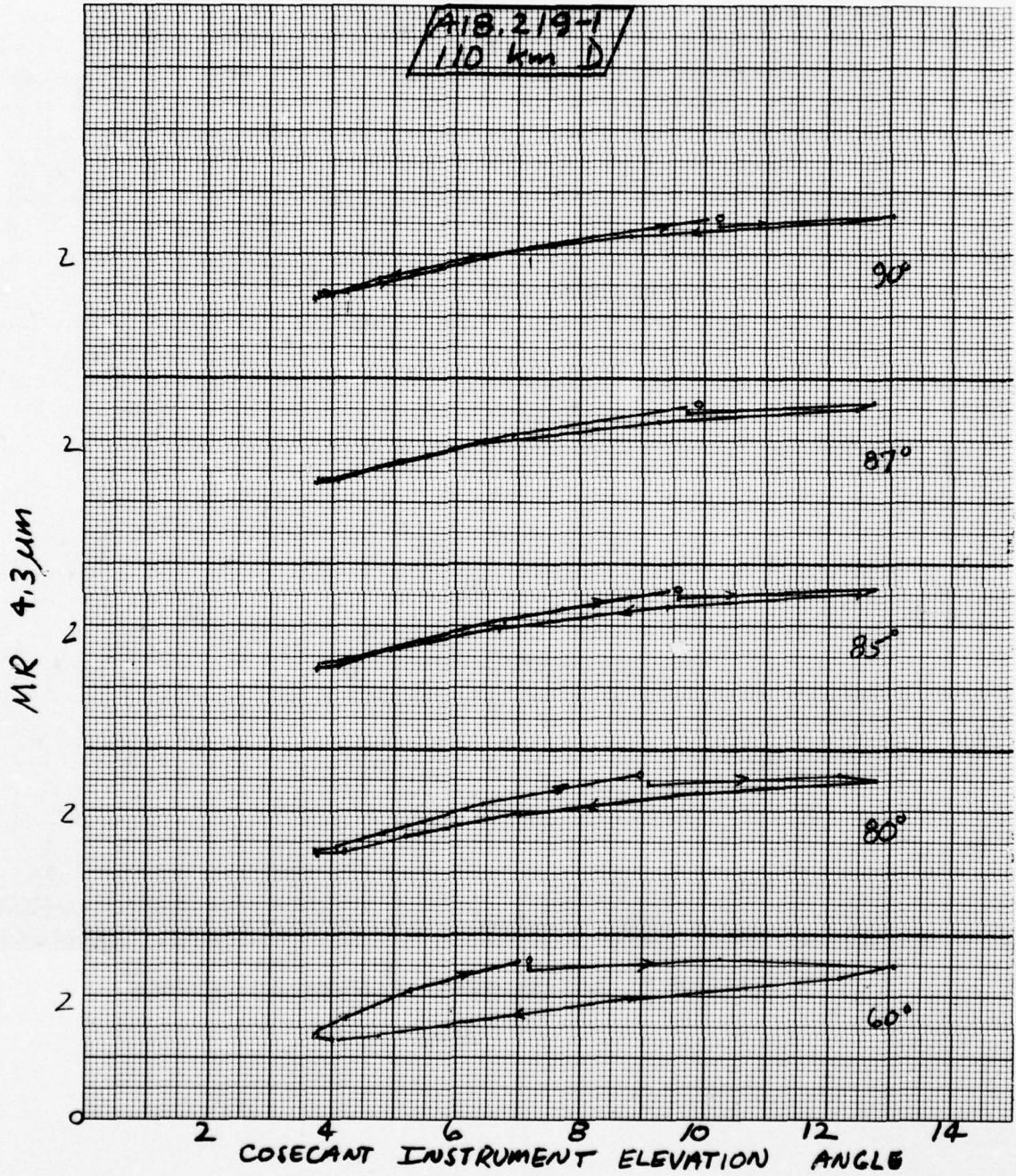
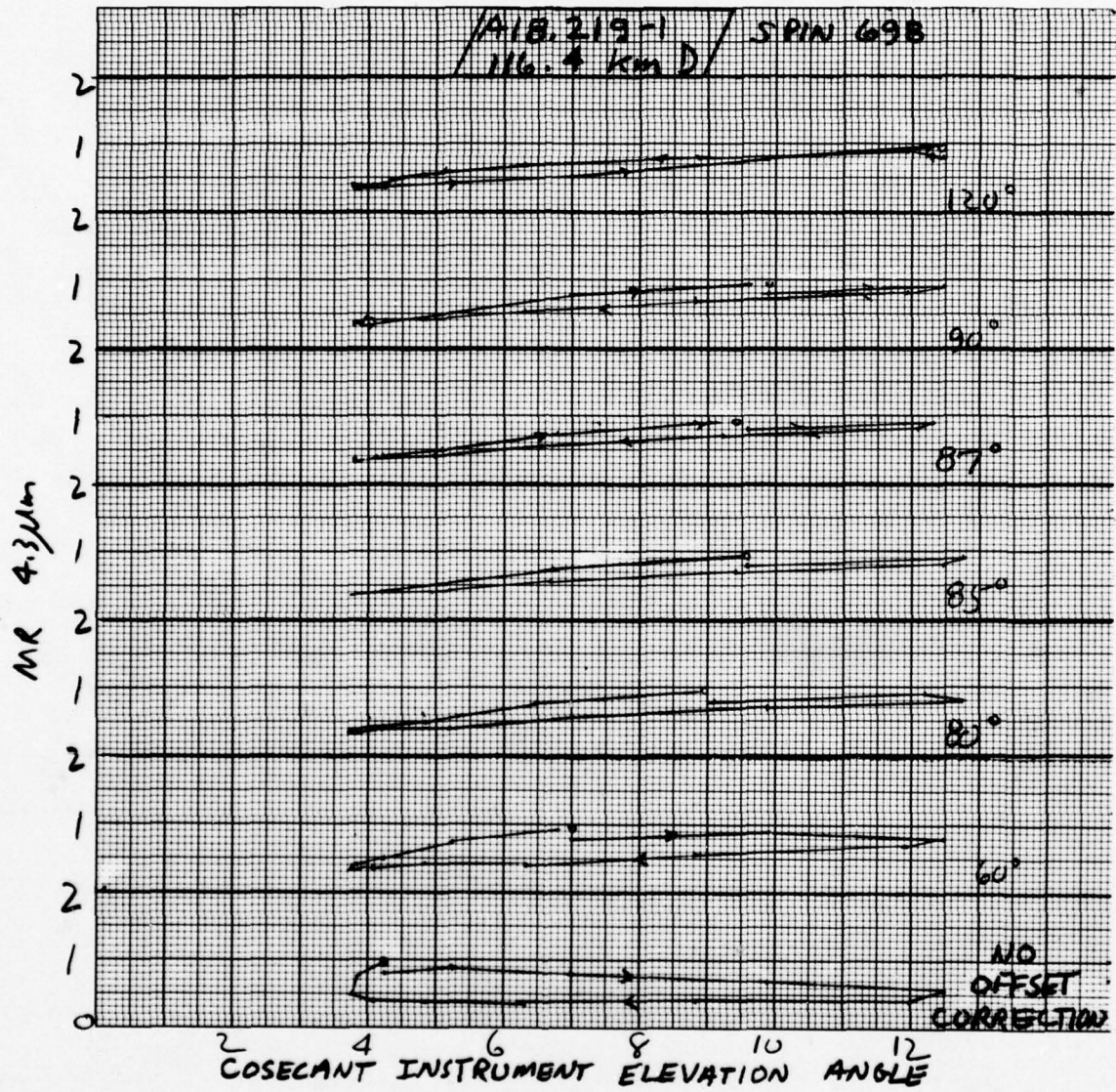


Figure 3a-c. Plots of 4.3 μm radiance against cosec of elevation angle of the radiometer's axis as a function of shift in the elevation-azimuth scales, for rocket altitudes between 116 and 103 km, A18.219-1 downleg.



3(b)



3(c)

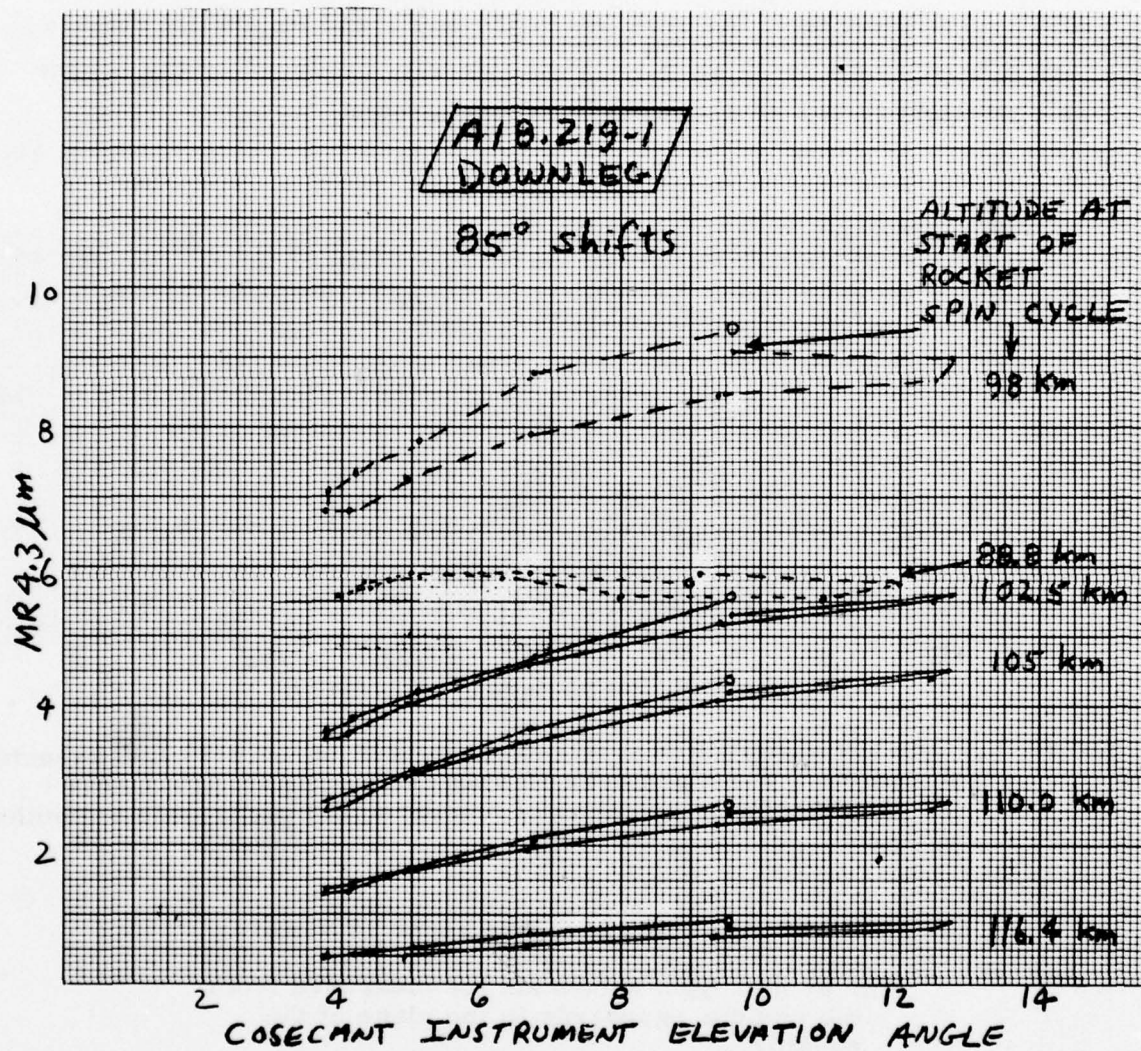


Figure 4. Summary of plots of 4.3 μm radiance against cosec of elevation angle of the radiometer's axis applying an 85° shift in elevation-azimuth scales, A18.219-1 downleg. The data presentation is complementary to that in Fig's 3a-c, as it shows the elevation angle dependence of radiance for rocket altitudes between 116 and 98 km (the spread in the plot for 88.8 km is due to the azimuth-dependent enhancement, Section II).

An average of ten spins from the wider band channel of the photometer is shown in Fig 5 for (uncorrected) geographic azimuths near 295° . The position of the peak is at $295\frac{1}{2} \pm \frac{1}{2}^\circ$, and its FWHM above a 150 R background is $5^\circ \pm \frac{1}{2}^\circ$. Peak intensity produced by the source is equivalent to 0.2 kR above the local background.

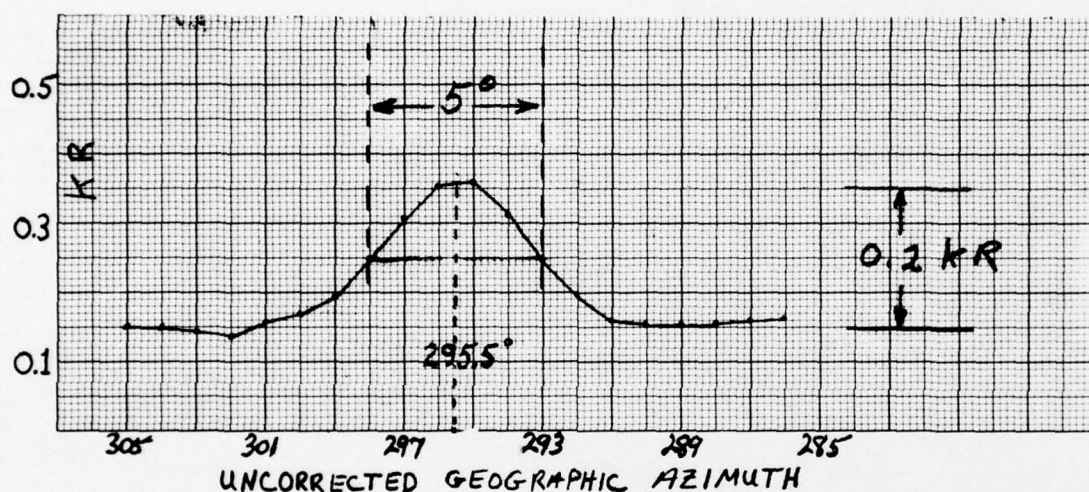


Figure 5. Radiance distribution in wideband channel of the 5199 \AA differential photometer, averaged over 10 spin cycles of A18.219-1 near 190 km altitude in the range of (uncorrected) geographic azimuths 305° - 286° .

The celestial coordinates of Sirius epoch 1974 were:

- 6 hr 44 min right ascension (as measured from the equinox eastwards in the plane of the equator,
- $-16^\circ 40' 46''$ declination (measured perpendicular to the equator, positive to the N).

We calculated the hour angle and declination of Sirius relative to the rocket's position at 190 km downleg (144° longitude, 66° N latitude at 0742:50 UT). These coordinates, converted to geographic azimuth and elevation angle above local horizontal at the rocket's altitude, are:

204.9° geographic azimuth, 5.1° elevation.

Thus the correction in geographic azimuth is $204.9^\circ - 295.5^\circ = -90.6^\circ$ from that indicated in the housekeeping data, that is, all original azimuths are moved eastward by 1/4 revolution. The elevation at the narrow peak, when both azimuth and elevation scales are shifted together (as is required on the basis of the rocket-axis aspect data discussed earlier) is 5.3° at the corrected azimuth of 205° . This is in satisfactory agreement with the elevation of Sirius, particularly when it is considered that the star does not necessarily pass exactly across a diameter of the radiometer's circular field.

The response of the wider channel of the 5199 \AA photometer to a point source producing the spectral irradiance of Sirius results in an equivalent radiance output of 0.19 kR; compare the approximately 0.2 kR in Fig 5. Since the weak air fluorescence-chemiluminescence averaged over the wider band near 5200 \AA produces an irradiance at the photocathode only comparable to that from Sirius, the star is readily detectable in this photometer's signal. It is also detectable, with lower signal/background, in the *el-az* scans of the narrow-band channel of the differential photometer. On the other hand no indication of this feature appears in either the 3914 \AA or 5577 \AA photometer data, since its equivalent radiance at these wavelengths would be only about 0.1 - 0.2 kR; the narrow source would be unresolvable over the typically 10 to 40 kR auroral levels near the same azimuth.

The net result of this investigation is that the first-reported azimuth and elevation scales must be shifted together by $90^\circ \pm 1^\circ$ in azimuth. Thus we have located geomagnetic N at 119° ($90^\circ + 29^\circ$) on the original geographic azimuth scales for assessing the CO_2 radiance data. Since the radiometer/photometer elevations change only slowly with azimuth (Fig 1), small errors in this azimuth shift have only second-order effect on calculations of ranges to or altitudes of emitting regions. For example a 5° error in azimuth at either the maximum or minimum instrument elevation angles of $15\frac{1}{2}^\circ$ and $4\frac{1}{2}^\circ$ results in an error of only 0.1° in elevation; near 135° geographic azimuth, where

the elevation angle is changing most rapidly, an uncertainty of 5° of azimuth produces the maximum elevation error of about 0.5° . Thus the plots in Fig 4 are complementary to the altitude profiles in Fig 6 for the series of azimuths-elevations, in that they represent the dependence of $4.3\mu\text{m}$ radiance on elevation angle at a series of altitudes above the radiance peak.

EFFECT OF THE ELEVATION ANGLE CORRECTION ON INTERPRETATION OF $2.8\mu\text{m}$ RADIANCE DISTRIBUTIONS

The large shift in instrument elevation angles makes the data from the sidelooking $2.8\mu\text{m}$ radiometer self-consistent at downleg rocket altitudes below 86 km. With the corrected elevations, the 2.42 - 3.11 FWHM background radiances fit a van Rhijn-like enhancement, contrary to our previous assessment (p 98 of Ref 3). Although the measured increases are too high to be explained fully by OH $\Delta v = 1$ -band radiation, they could be caused by either leakage of thermal radiation originating from still lower altitudes - a chronic problem with the infrared radiometers - or by the earth-limb features observed from AFGL/DNA's Sept 77 "Spire" spectrometer-carrying rocket IC733.03-1 (which included strong emission near $2.4\mu\text{m}$, Ref 7). Thus enhanced limb radiation overlying the features associated with auroral particle-excited air fluorescence, which becomes self-consistent when the instrument's pointing angles are corrected, provides an attractive alternative interpretation of the apparent decorrelation of sidelooking $2.8\mu\text{m}$ signal from this fluorescence below 86 km (as shown in Fig 49b of Ref 3). (Previous assessments have considered the effect to be caused by a "cloud" of engine exhaust coming into the sidelooking instrument fields as the rocket starts to tip over; this putative cloud has major impact on the interpretation of zenith radiance near $2.8\mu\text{m}$, p 404 of Ref 4.)

RADIATION PROFILES

Altitude profiles of the atmosphere's radiance in the 4.21 - 4.305 μ m wavelength band, plotted at 30° azimuth intervals between 130 and 82 km on downleg of A18.219-1's trajectory, are in Fig's 6a-1. The pointing angles, which refer to the radiometer's optic axis, apply the 90° azimuth shift and accompanying elevation shift derived above. The angular field of the instrument is shown in Fig 20 of Ref 3, and its spectral sensitivity in Fig 18 of this report. 4.3 μ m-band radiances measured by the rocket's near vertical-viewing fixed-filter and wavelength-sweeping (circular variable filter) radiometers (Ref 4, p 427 and Ref 8) are shown for comparison in Fig 7. We interpret the low elevation-angle radiance distributions here only to the extent necessary to verify the accuracy of the data from the side-viewing 4.3 μ m radiometer.

Above 130 km on downleg the signal lies in what appears to be instrument noise. Below 85 km the radiometer's elevation angle at a given azimuth changes rapidly as the rocket's long axis moves through the vertical and then tilts downward, as shown on p 433 and p 500 of Ref 4. On upleg the data exhibit narrow noise spikes of the type in Fig's 30a and 31a of Ref 3 that disappear by 92 km, after which there remains some excess radiance at geomagnetic azimuths between 240° and 30° (that is, in the northwest quadrant from the rocket \pm 30°). Near 110 km this small excess evolves rapidly into an off-scale peak centered at 285° with skirts of 60° azimuthal extent, of the type in Fig 27b of Ref 3, evidence of which persists to ~160 km. As the radiance excess between 92 and 110 km is inconsistent with an increase from van Rhijn effect, it is probably related to the artifact that produces the strong signal over sensibly the same azimuth-angle range at higher altitudes. To provide a partial comparison between upleg and downleg 4.3 μ m-band profiles, we have plotted the upleg radiances from the uncontaminated azimuths 120° and 210° in Fig's 6f and i. (A more informative comparison can be made by applying the other radiance data from between 30° and 240° azimuth, correcting the 240° \rightarrow 30° data set, and filtering the narrow noise spikes present below 92 km altitude.)

Narrative text continues on page 33.

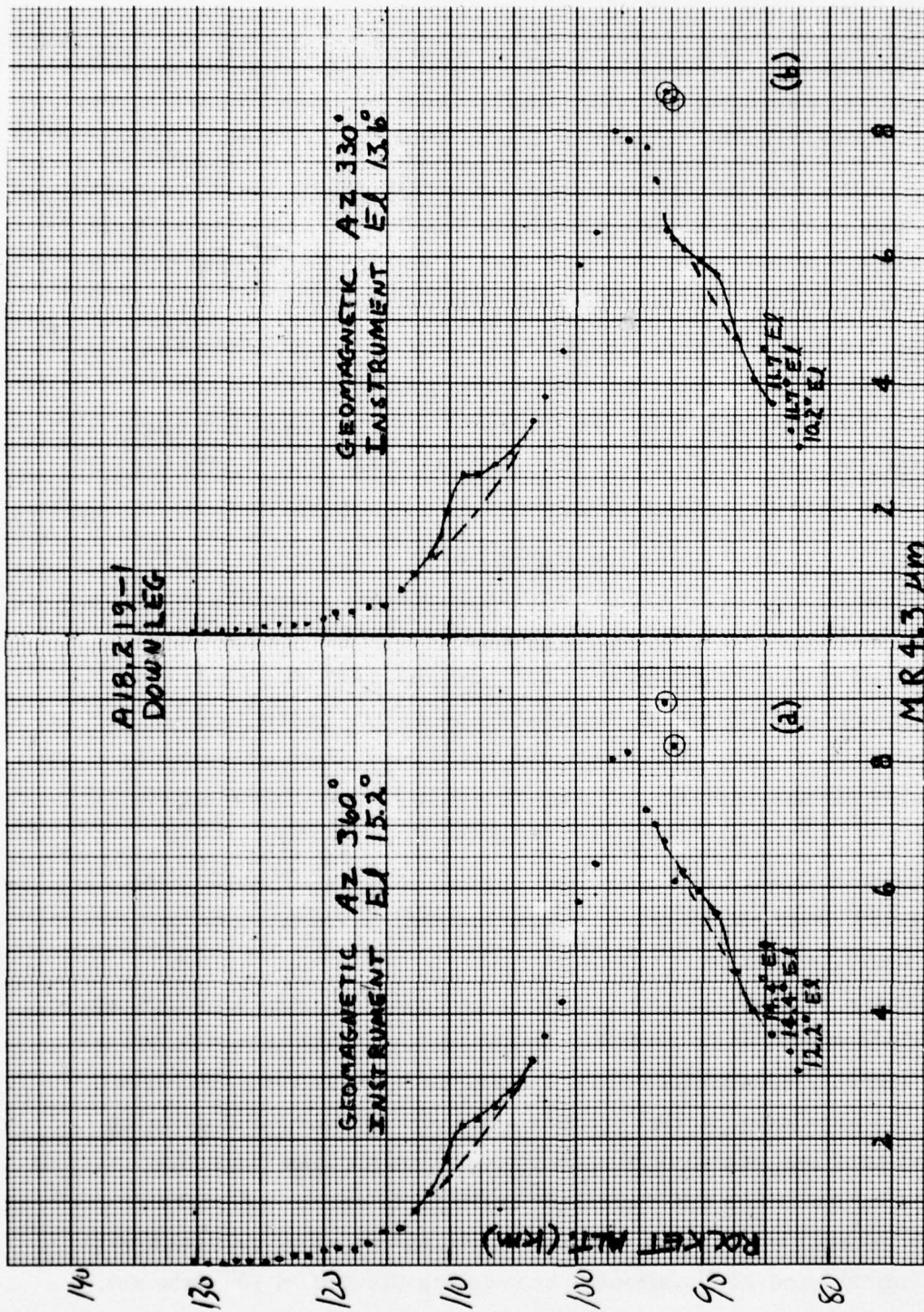
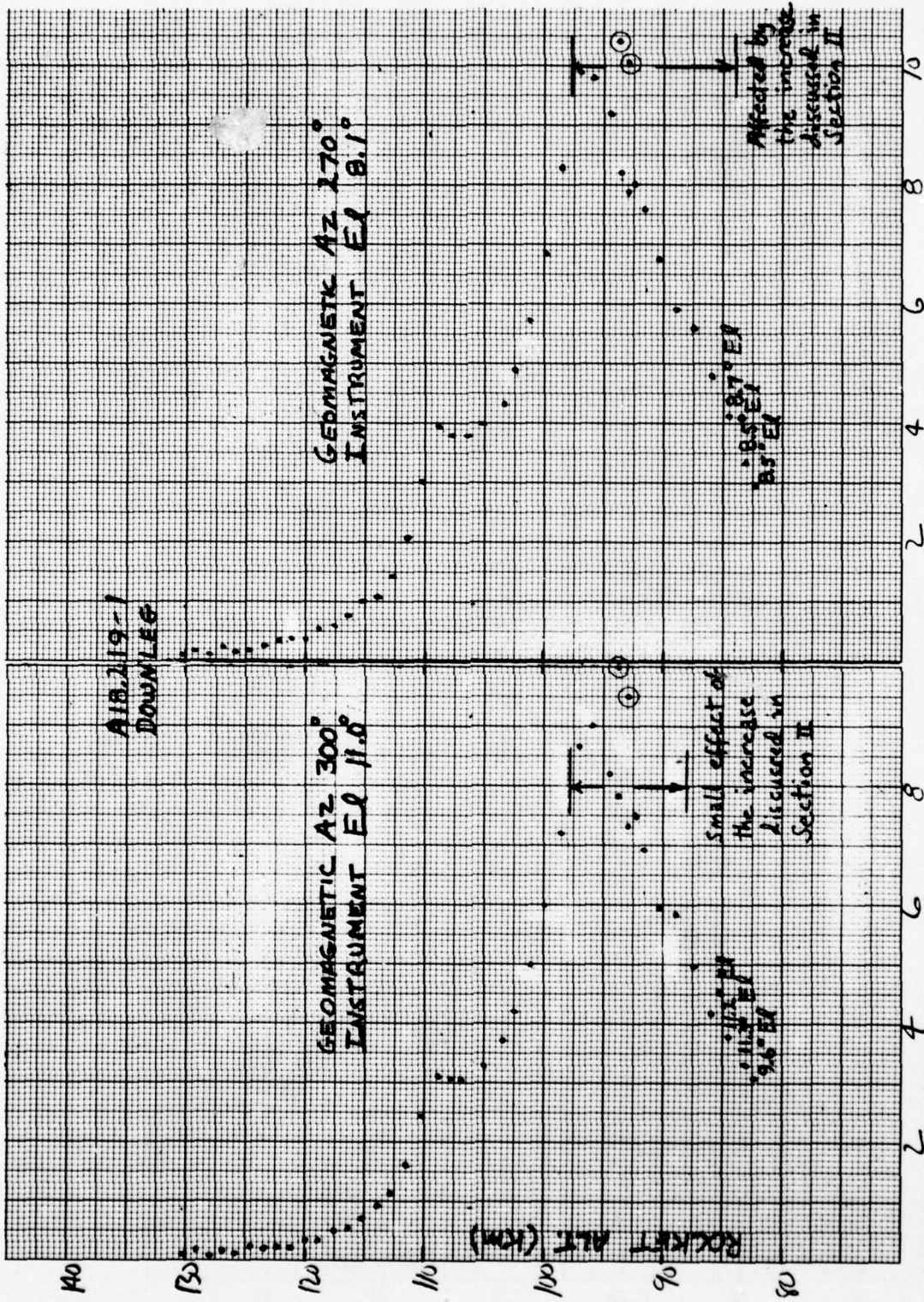


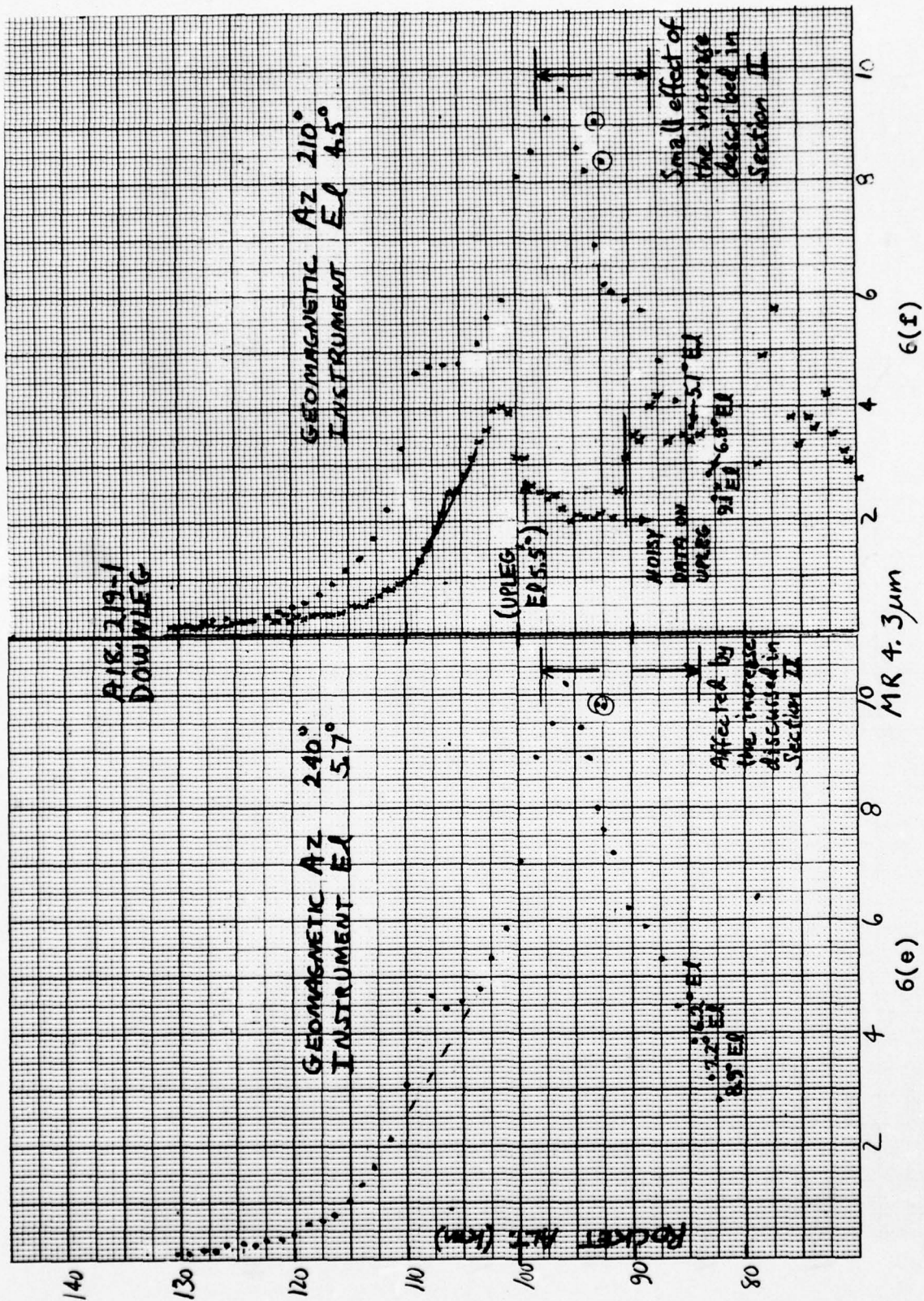
Figure 6a-f. Altitude profiles of $4.3 \mu\text{m}$ radiance measured at 30° azimuth intervals by the side-looking radiometer on downleg of A18.219-1. The numbers next to the points below 85 km are the instrument's elevation angle as the rocket begins to destabilize. Comparison upleg data are included for 120° and 210° geomagnetic, near $5\frac{1}{2}^\circ$ and 9° elevation angle. The circled points have been corrected as described in the text.

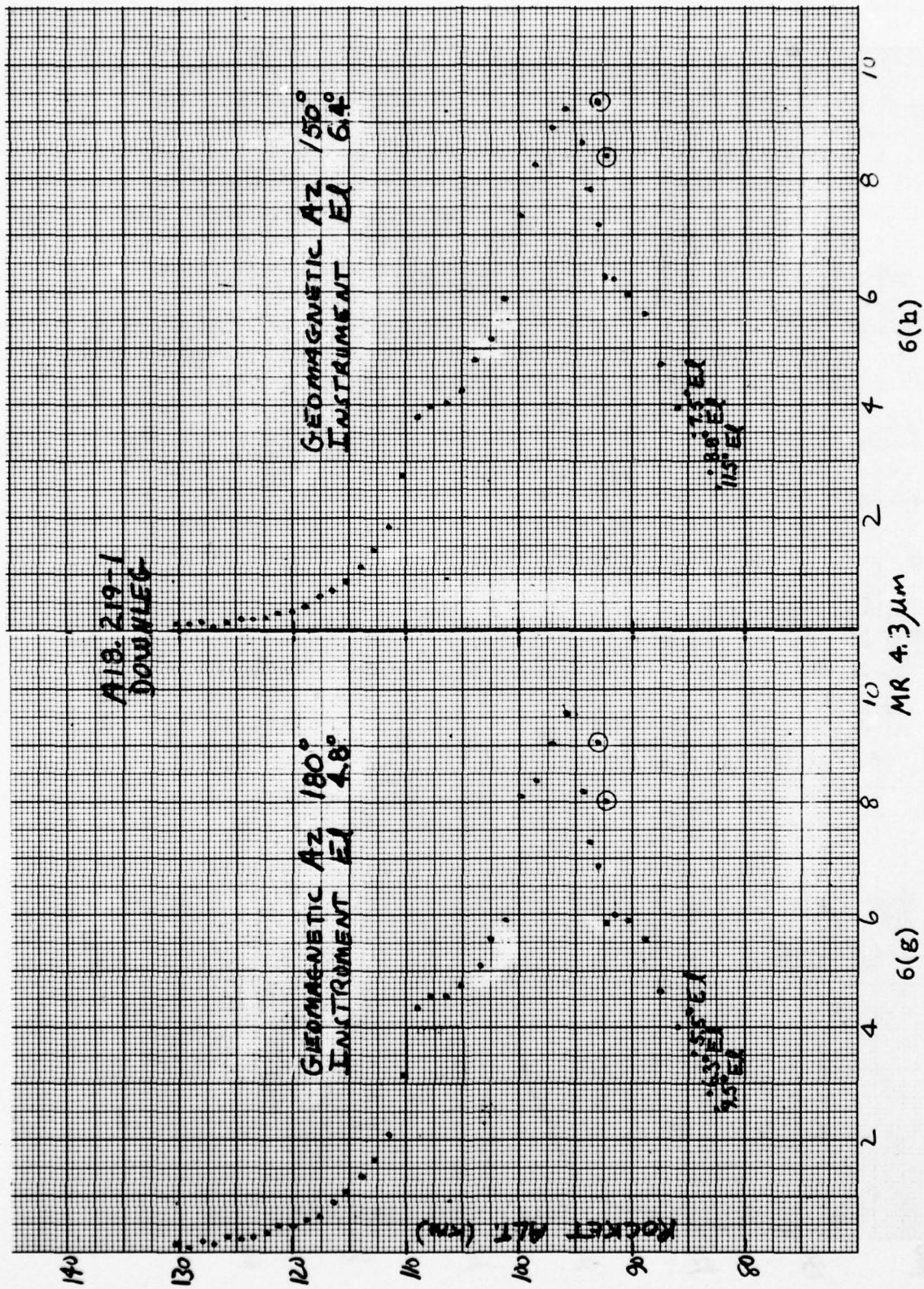


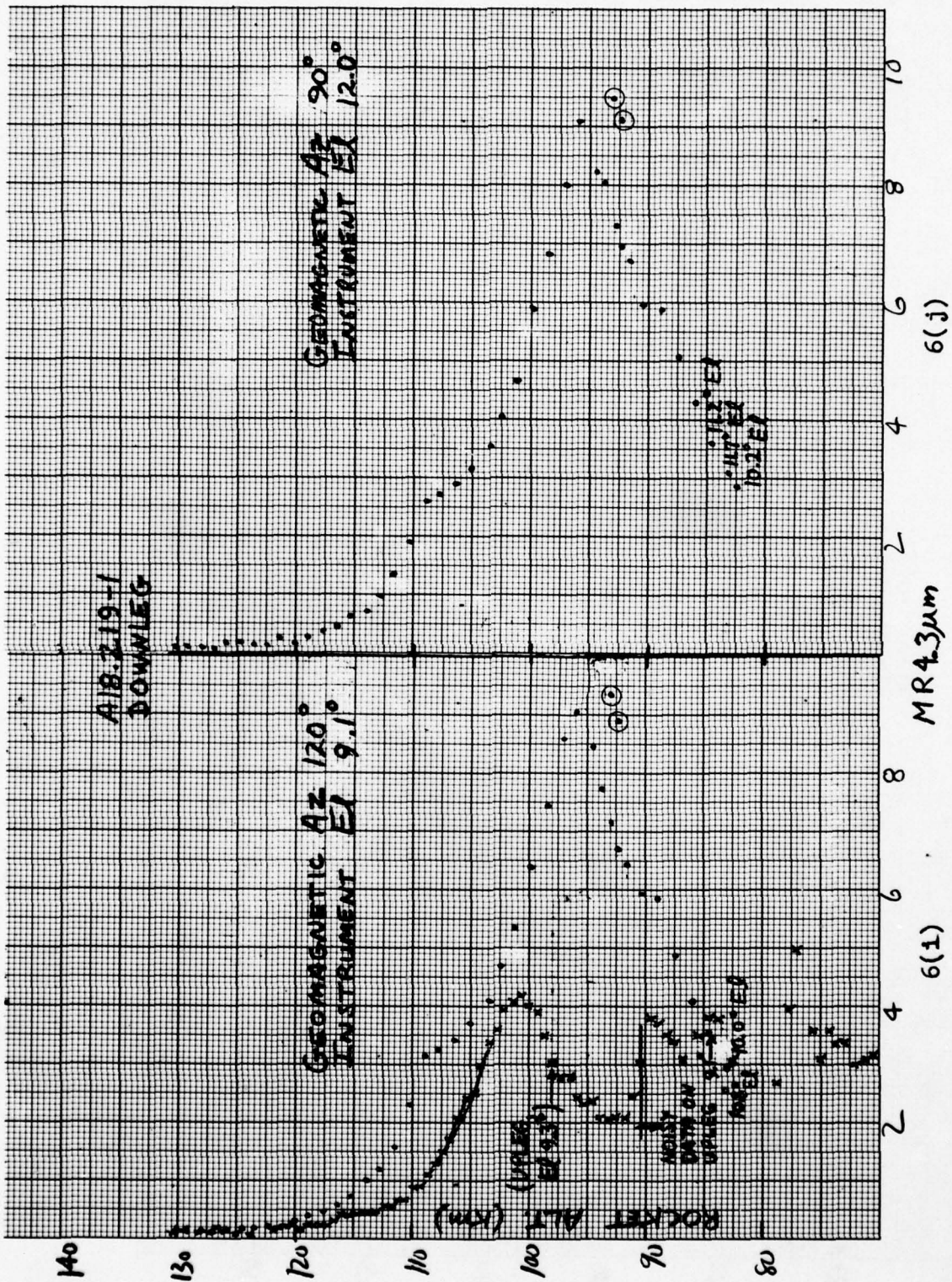
6(d)

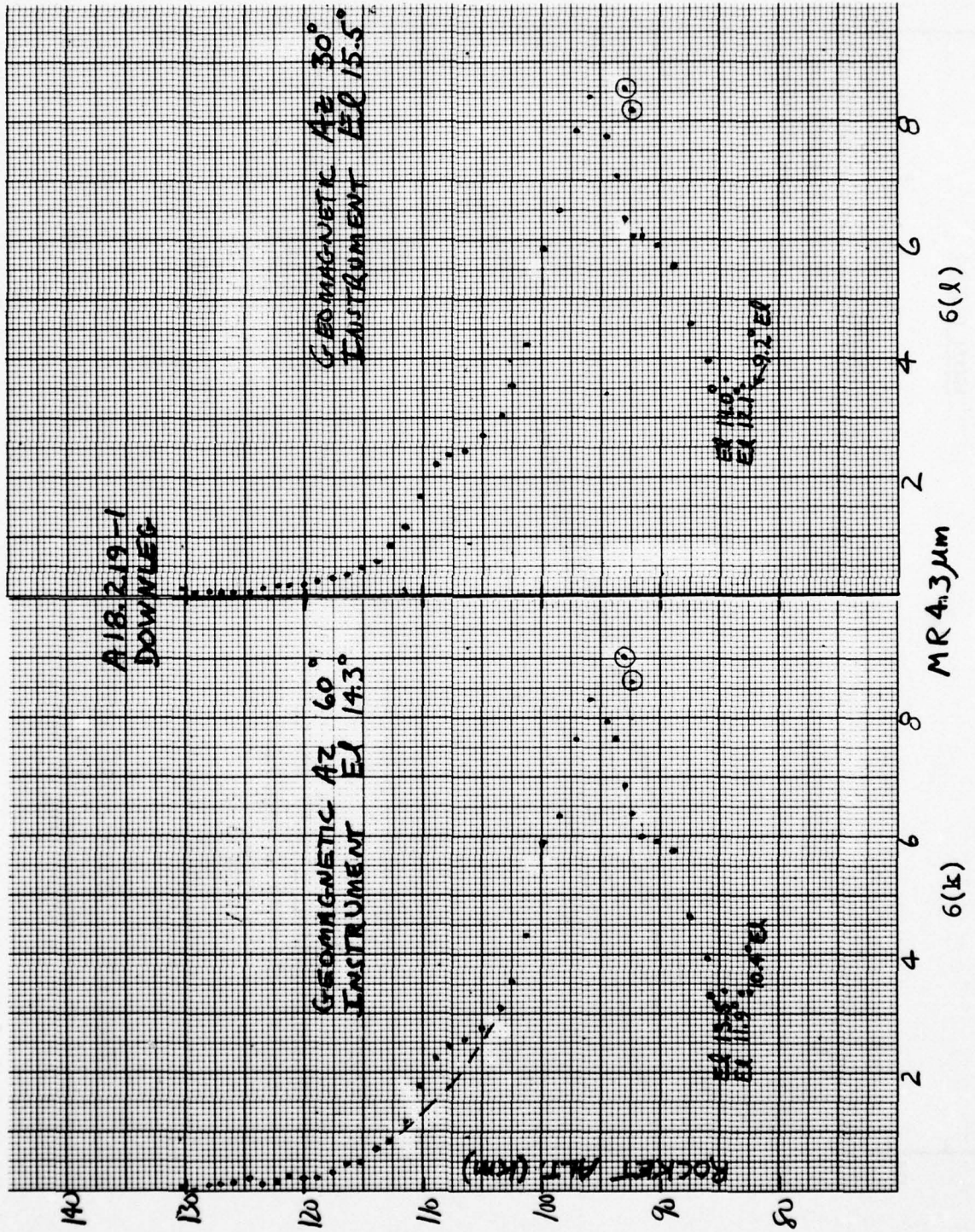
MR 4.3 μm

6(c)









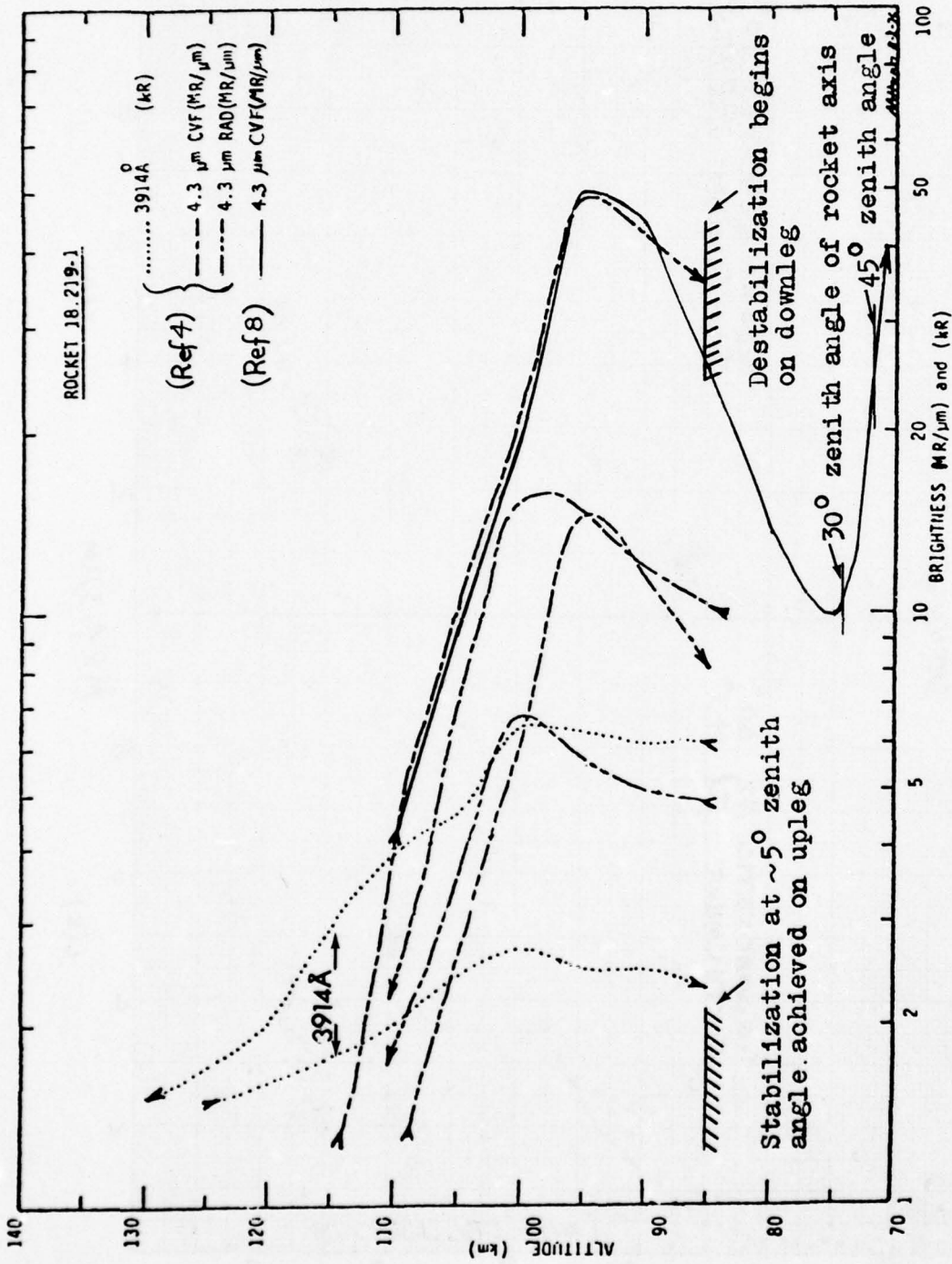


Figure 7. Near-zenith altitude profiles of 4.3 μm and 3914 Å radiance measured by the axial-pointing instruments on upleg and downleg of A18.219-1.

Our earlier characterization of the auroral ionosphere for the 25 Feb 1974 flight (Appendix VII of Ref 2, and Section II of Ref 3; refer in particular to the all-sky views from PKR and FYU, Fig 55 of Ref 3) shows a complex system of arcs, with particle precipitation both south and north of the rocket during the downleg data period of Fig 6 (342 - 380 sec). The northward vector component of the rocket's velocity was about $\frac{1}{4}$ km/sec, and its trajectory lay very close to the 13° -inclined geomagnetic field lines. The most intense arc (in the projection from PKR), whose field lines recrossed the rocket when it was at 180 km on downleg, had a phase velocity of ~ 1 km/sec N; when the rocket was at 100 km (360 sec) the S "edge" of this brightest auroral region lay ~ 75 km N of the radiometer. A second broad arc had intensified further to the N by this time (Fig 42 of Ref 3). The arc to the S of the rocket was weak along the PKR-FYU meridian and bright towards the W, as is described in more detail in Section II where the immediate and earlier dosing of the atmosphere is further reviewed. A semi-quantitative plot from the meridian scanning photometer (p417 of Ref 4) depicts with moderate resolution the predosing of the air in the vicinity of the rocket. As both Fig 6f-i and 7 show, the $4.3\mu\text{m}$ levels near peak radiance are at least a factor 2 higher on downleg than on upleg (a matter discussed in the presentation starting on p 304 of Ref 4).

The restricted range of altitudes and azimuths in which fluorescence-related increases in $4.3\mu\text{m}$ -band radiance (whose implications are discussed in Section II) are observed, is indicated in Fig 6. The data from the sidelooking $4.3\mu\text{m}$ radiometer otherwise show no obvious correlation with the instantaneous energy deposition by charged particles that produce the optical aurora, example profiles of which are in Fig 8. $4.3\mu\text{m}$ -band profiles for the lowest, second highest, and one intermediate elevation angle in Fig 8 indicate that the altitude at which radiance is a maximum decreases by about 1 km between 15° and 5° el in the predosed auroral atmosphere. Over this range of elevation angles the column concentration of CO_2 molecules in the radiometer's

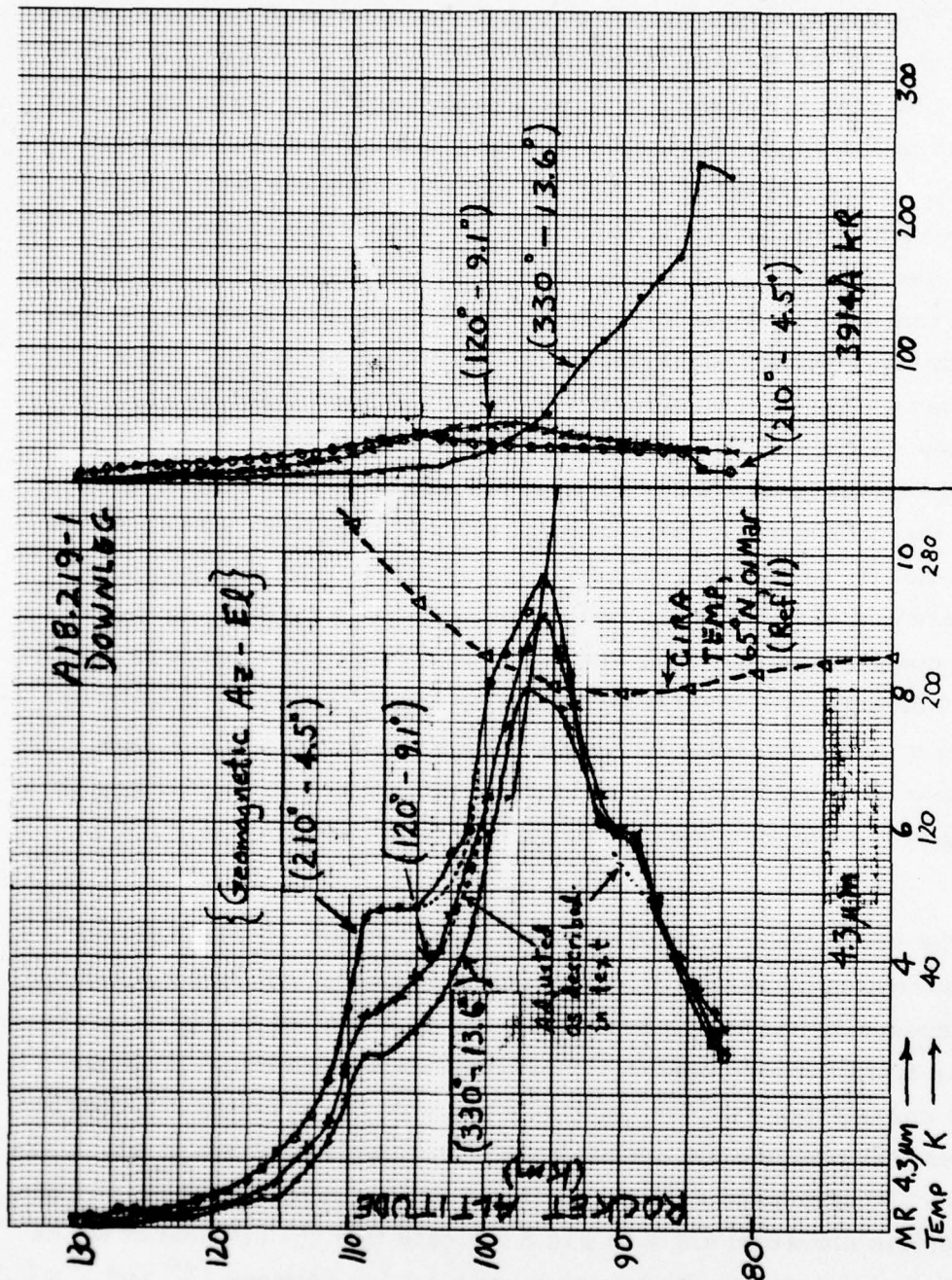


Figure 8. Altitude profiles of 4.3 μm and 3914 Å radiance at three azimuths - elevations, A18.219-1 downleg. The dotted 4.3 μm profiles near 5 1/2 MR apply the adjustment described in the text.

field of view changes by about a factor $2\frac{1}{2}$, applying "density" profile model F in Ref 9. The downleg altitude profiles in Fig 6 and 8 also show two subsidiary layers at all azimuths-elevations, which are discussed in the next subsection.

The two data points near $92\frac{1}{2}$ km (circled on Fig 6) lie $\sim 2\frac{1}{2}$ MR above the interpolated profiles at all azimuths. The radiance increase (Fig 9) starts at 371.88 sec and persists for closely two rocket spin cycles (1.03 sec) before decreasing to near its previous level over the same azimuth range as its increase, $\sim 11^\circ$ (0.015 sec). An increase of substantially greater absolute magnitude appears simultaneously in the data from the $2.8\mu\text{m}$ segment of A18.219-1's dual radiometer. Since similar level shifts are present in the telemetry from both radiometers at fixed intervals throughout the flight, we ascribe them to a calibration signal additively superposed on that produced by the scene radiances. Specifically, these 1 sec-duration step increases occur regularly at 34.3 sec intervals beginning at 97.48 sec, and average 2 MR above the local $4.3\mu\text{m}$ radiance. (Radiometers and photometers on earlier multi-instrumented rockets were documented as fitted with internal light-emitting diodes which were periodically activated to provide an inflight measure of relative system responsivity, p 37 of Ref 10; the excess signals from A18.219-1 are in all probability due to this source.) Taking into account the height of the step increase in Fig 9 and the next az-el scan (Spin 734), we have reduced the $4.3\mu\text{m}$ altitude profile readings by 2.2 MR between 371.88 and 372.91 sec (93 and 92 km in Fig 6).

A18.219-1's $4.3\mu\text{m}$ filter radiometer was a refurbishment of the $5.3\mu\text{m}$ radiometer recovered from the 1973 multi payload (A18.205-1). The response characteristic for the latter instrument had a sharp change in slope near 2.71 telemetry volts (Ref 10). The data printout lists both received TM voltages and the $4.3\mu\text{m}$ radiances they are assigned by computer in the ground-reconstruction process. It shows that the 1974 version's break point was at 2.78 TM volts, 5.9 MR,

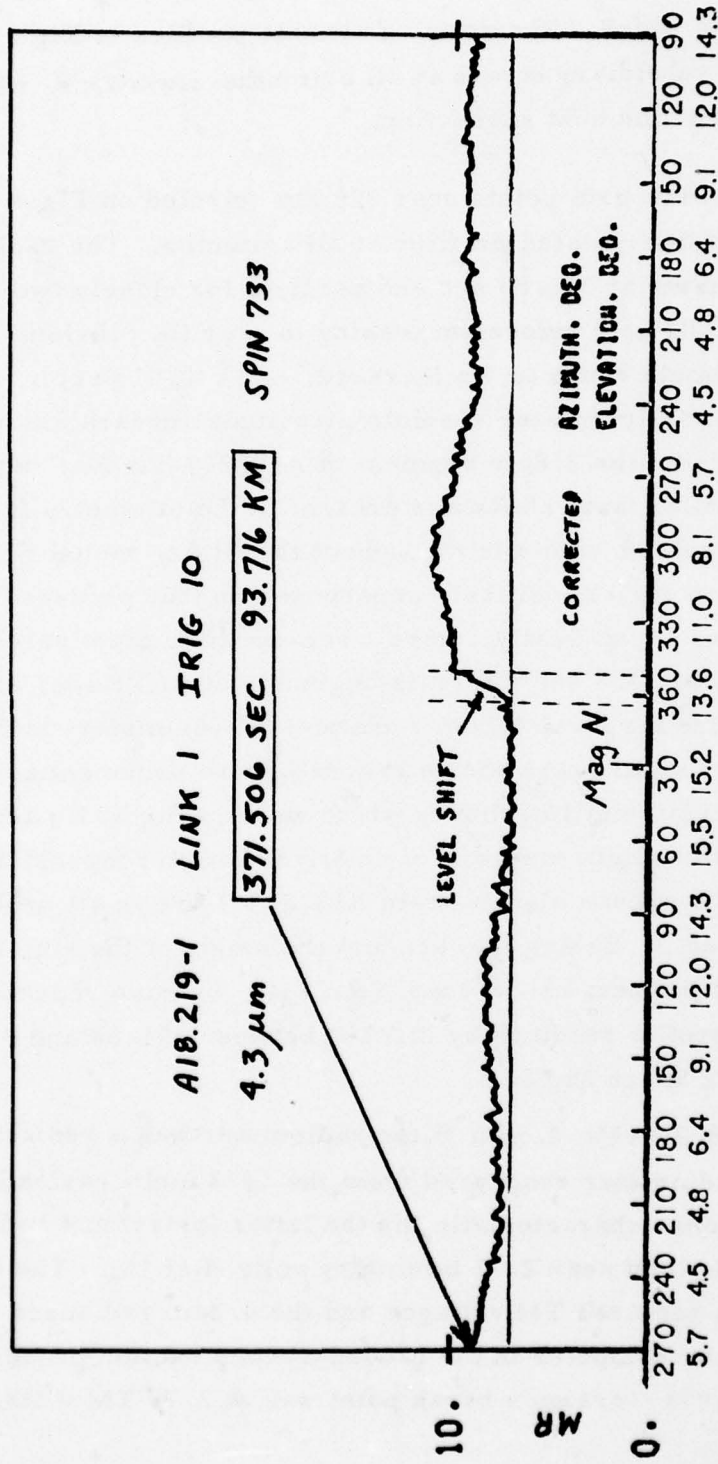


Figure 9. 4.3 μm az-el radiance distribution on downleg spin cycle 733 of A18.219-1, showing the sharp discontinuity starting at 371.88 sec.

above which the slope of the characteristic decreases by a factor 9 (Fig 10). The radiometer's input-output response characteristic - scene radiance (converted to amplified photocurrent) to this same TM voltage - appears to lie above that used in the reconstruction below the break point (at least), as is evidenced by the presence of sections of radiance lying very close to 5.9 MR. The seven circles in Fig 10 were located by interpolating in Spin 723 ($100\frac{1}{2}$ km) between radiances transferred above the minimum of the low-sensitivity segment of the characteristic and those below the maximum of the high-sensitivity segment, which reproduce as "flat" over two $\sim 80^\circ$ -azimuth ranges. (That is, we faired together $4.3\mu\text{m}$ radiances between 4-5 and 6-9 MR regions, whose reproduction is self-consistent; and plotted the interpolated radiances against TM voltage.) The effect of this imperfection in the instrument's data transfer characteristic is to reduce 5-6 MR radiances by $\sim \frac{1}{2}$ MR (see Fig 10). Self-consistency of the reconstructed $4.3\mu\text{m}$ -band data in other radiance ranges, to which this interpolation-correction procedure cannot be applied, does not of course imply that no further systematic error is present.

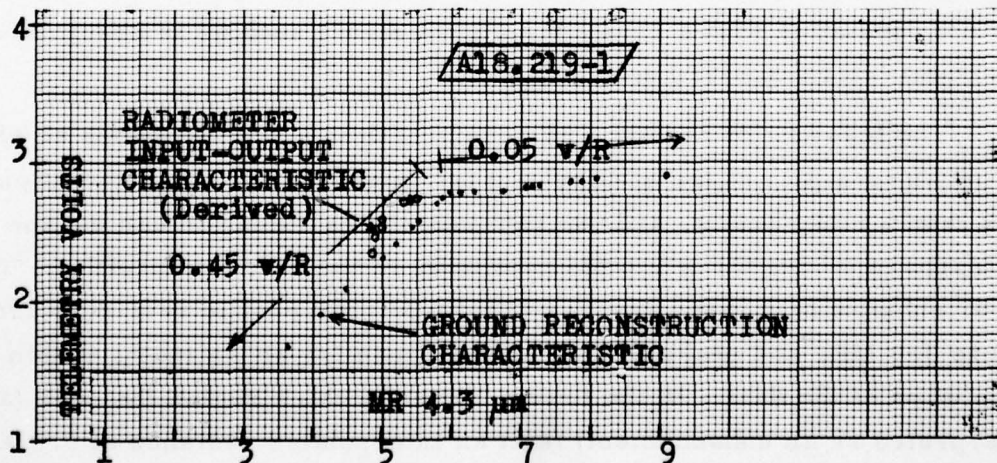


Figure 10. Transfer characteristics of A18.219-1's sidelooking $4.3\mu\text{m}$ radiometer as determined from the data print-out in the time period 365.4 to 368.5 sec, and interpolated from Spin 723 where the radiances lie on both sides of the break point.

LAYERING OF THE RADIANCE PROFILES

The altitude profiles indicate layering of the radiation density both above and below the main peak near 96 km. If these irregularities are interpreted as enhancements, the upper one maximizes at $109 \pm \frac{1}{2}$ km at all azimuths, and the less well-resolved lower subsidiary peak at $88\frac{1}{2} \pm \frac{1}{2}$ km. This radiance structure is not correlated with prompt air fluorescence in the radiometer's field of view, as the representative comparison profiles in Fig 8 show.

Fig 11 is a plot of the upper layer's "excess" $4.3\mu\text{m}$ radiances above a manually interpolated baseline (dashed lines in Fig 6a for example) as a function of pointing azimuth. The enhancement is discernible above the small fluctuations in radiance in the altitude range at least 111 to 106 km at all azimuth angles. It is highest toward the SW (near 210°) where the elevation angle reaches its minimum and the interpolated sky radiance is a maximum. In Fig 12 are plotted profiles of the fractional increase above this interpolated intensity. The variability of these fractional changes indicates that they are probably not due to a slow change in sensitivity of the radiometer system; for example, at the peak the fraction varies between 0.35 and 0.65. In addition the increases are not consistent with a constant additive signal such as is observed at 92-93 km (starting 371.9 sec, Fig 7).

The layering of radiant flux occurs both in altitude regions at which the mean free path of the atmosphere for (most) $4.3\mu\text{m}$ CO_2 radiation is less than a scale height, and where much of this radiation can escape the atmosphere (above the principal maximum in the radiance profile). The upper enhancement layer appears at interpolated-profile radiances from 1.5 to 3.0 MR, and peaks at the same altitude for all azimuths within the resolution of the data. In the lower, optically thick region the peak (again interpreted as an enhancement) is at an interpolated radiance of $5.2 \pm \sim 0.2$ MR, near $88\frac{1}{2}$ km rocket altitude at all azimuths-elevations (as best as can be determined).

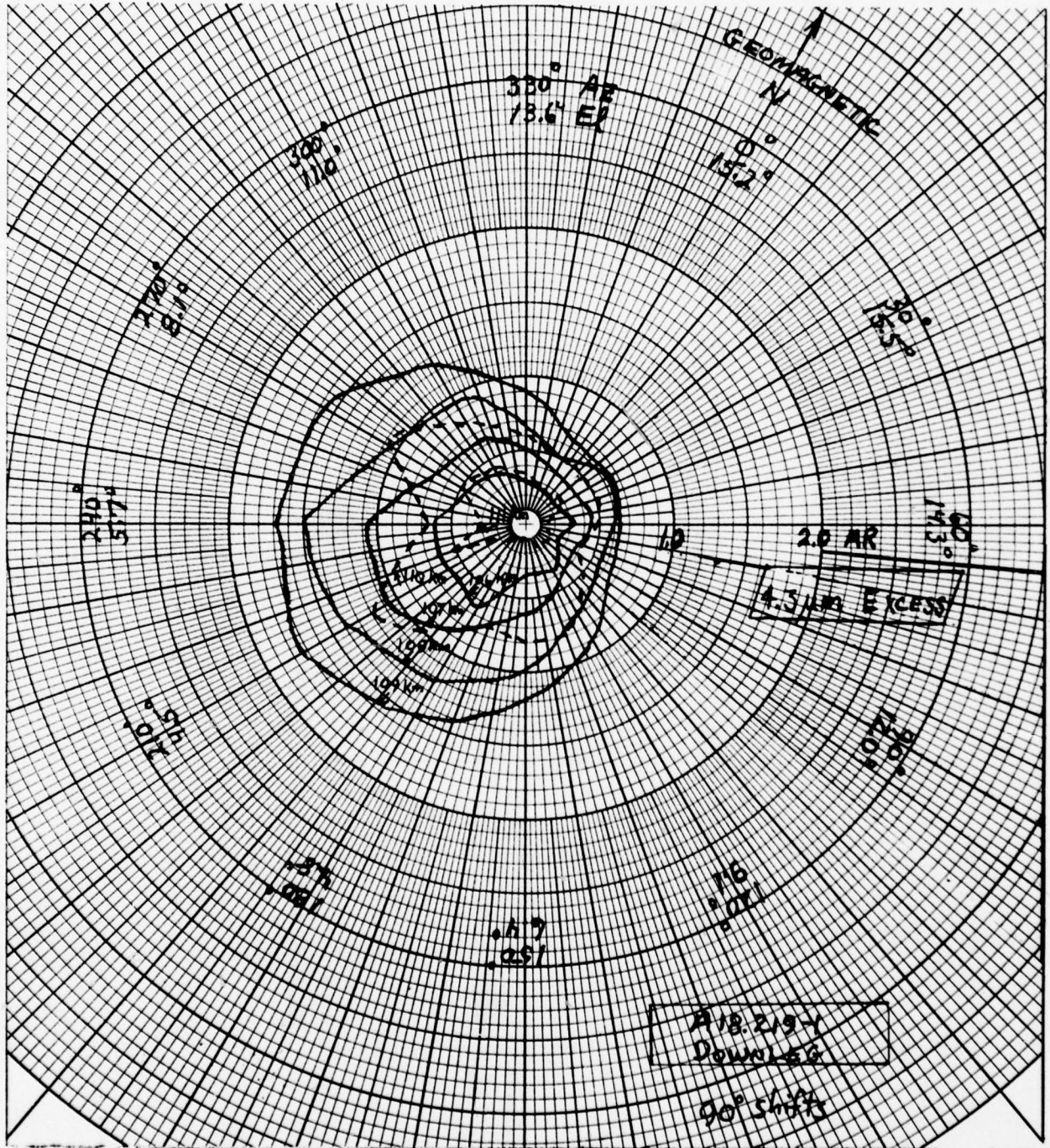
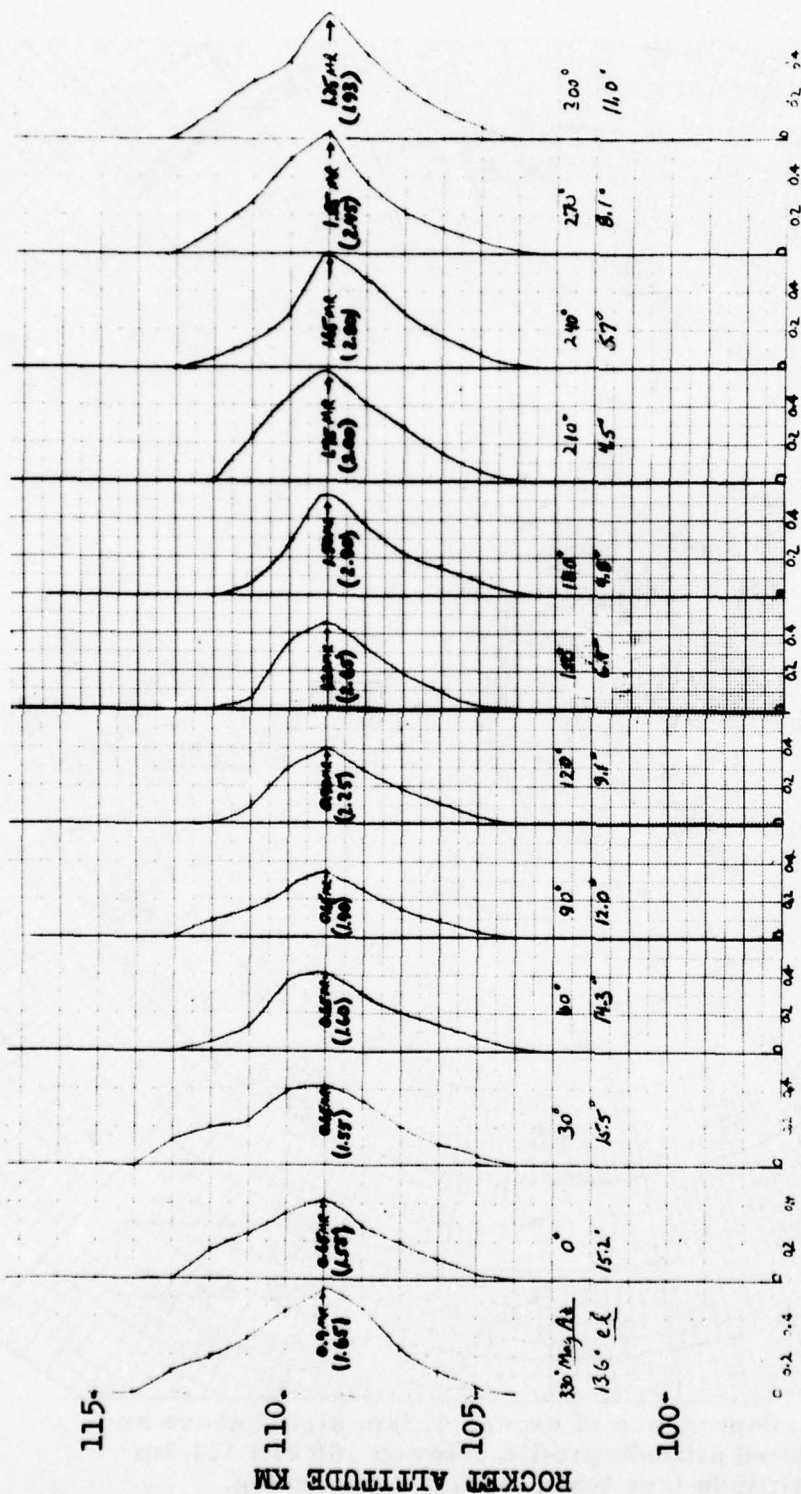


Figure 11. Azimuth dependence of excess $4.3\mu\text{m}$ signal above an interpolated altitude profile between 106 and 111 km rocket altitude (see text), A18.219-1 downleg.



EXCESS 4.3 μm SIGNAL/INTERPOLATED 4.3 μm INTENSITY PROFILE

Figure 12. Altitude profiles of the fractional increase above an interpolated 4.3 μm intensity profile near 109 km rocket altitude, A18.219-1 downleg. The numbers in parentheses are the baseline intensities at the peaks.

The upleg altitude profiles (Fig's 6f,i) give some hint of a high altitude (~ 106 km) layering similar to that observed in the downleg profiles. Estimated peak excess above an interpolated radiance profile is 0.3 MR above $2\frac{1}{4}$ MR, a ratio substantially less than those in the more heavily predosed air volumes shown in Fig 12. We are at present investigating the upleg $4.3\mu\text{m}$ -radiance data at other azimuths for further evidence of irregularities.

The extent to which this layering of radiation density could be an effect of error in transfer-telemetry of data from the rocket radiometer can be in part determined from the characteristics in Fig 10. The warp in the altitude profiles above the principal peak near 96 km lies at levels too far below the break point to be ascribed to this source. The lower layer might be interpreted as a local maximum lying below the break point, or a minimum above it; see in particular Fig 8. Thus the departure from smoothness of the profile below 96 km could be caused either by the aforementioned $\sim \frac{1}{2}$ MR offset in the instrument's transfer characteristic below 5.9 MR, or by a defect in reproduction of radiances between ~ 6 and 9 MR.

Profiles to which are applied the interpolation-derived "correction" between ~ 5 -6 MR from Fig 10 are included as dotted lines in Fig 8. Such an adjustment in effect removes the lower layering while deepening the profile irregularity above the main $4.3\mu\text{m}$ radiance maximum. The argument that the lower layer is an artifact is strengthened by the observation that the inflection in the profile always occurs in the same radiance range near the break point. However this radiance is in any case virtually constant with elevation angle near 89 km because the atmosphere has become optically thick to radiation in the $4.3\mu\text{m}$ filter band. (Refer to the plot in Fig 4; the "spread" at 88.8 km starting altitude is caused by the fluorescence-related signal discussed in Section II.)

Viewing in the zenith from above the main peak, the irregularity in radiation flux would have a lower signal/background ratio or "contrast." This could explain why it has not been detected in previous rocket experiments (and why it does not show clearly, if at all, in the data from the near zenith-viewing filter radiometer and circular variable filter spectrometer on A18.219-1, Fig 7). We have included for reference the kinetic temperature profile for the late winter sub-polar atmosphere (from Table 18a of Ref 11); the vibrational temperature of the CO_2 molecules is known to be out of equilibrium with this local temperature at altitudes where aurora-producing particles deposit their energy. The upper layering may be an effect of adding two sources of pumping of the upper state(s) of $4.2 - 4.3 \mu\text{m}$ CO_2 emission, auroral-collisional (through N_2^+ and reabsorption of photons, Ref 5) and by absorption of principally-thermal atmospheric radiation. The lower amplitude of any irregularity in the more weakly-predosed upleg region is supportive of this hypothesis.

SECTION II

CORRELATED 4.3 μ m FEATURE NEAR GEOMAGNETIC WEST

NEAR-PROMPT 4.3 μ m EMISSION

Elevation-azimuth scans in the 4.3 μ m band on downleg of A18.219-1 show a weak feature at $\sim 290^\circ$ geographic azimuth that correlates with a narrow peak seen by the visible aurora-monitoring 3914 Å and 5577 Å photometers. This largely-unexpected excess emission, which was given preliminary notice in Ref 3 (p102ff), is further evaluated and interpreted in this Section.

The feature initially appears on the 4.3 μ m signal as a small enhancement detectable in scans below approximately 102 km rocket altitude. Figure 13 shows the data from the spin starting at 102 km from the 4.3 μ m radiometer, along with the radiances measured at 2.8 μ m, 5577 Å, and 3914 Å. Figure 14 is a detail of the region near 290° (260° geomagnetic) at 4.3 μ m and 3914 Å, along with plots of the angular responses of the two instruments. This feature at 4.3 μ m is not associated with the change in the radiometer's transfer characteristic at radiant intensities near 5.9 MR (explained in Section I).

Figure 15 compares the 4.3 μ m radiance distributions at several downleg altitudes down to 92.3 km with the 3914 Å distributions. The peak at 4.3 μ m aligns very closely with that at 3914 Å. However, the 4.3 μ m peak at the lower altitudes - not discussed in our preliminary review - has broadened considerably.

CORRELATION WITH ALL-SKY AND MERIDIAN SCANNING PHOTOMETER DATA

The excess emission appears near 260° geomagnetic azimuth, or 10° south of geomagnetic west. The strong, narrow enhancement in the 3914 Å data can be explained qualitatively from the all-sky camera photographs taken from Fort Yukon and Ester Dome (Fig 16 and Ref 3, p110) in combination with the meridian-plane radiance distribution measured by the scanning photometer at Poker Flat.

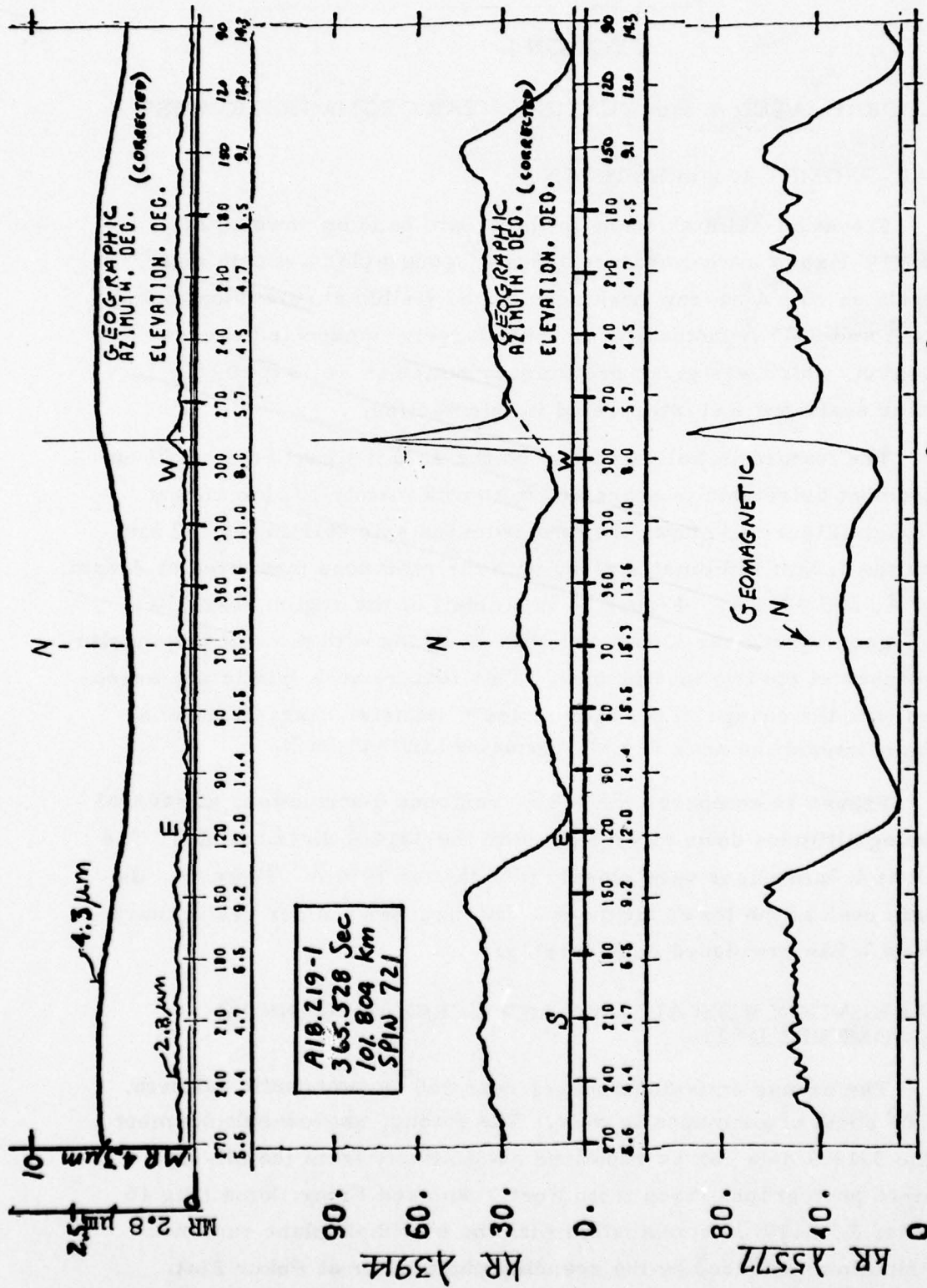


Figure 13. A comparison between 3914 Å, 5577 Å, 2.8 μm, and 4.3 μm for Spin 721 on downleg of A18.219-1. The scales have been corrected in elevation and azimuth for a 90° shift (Section I).

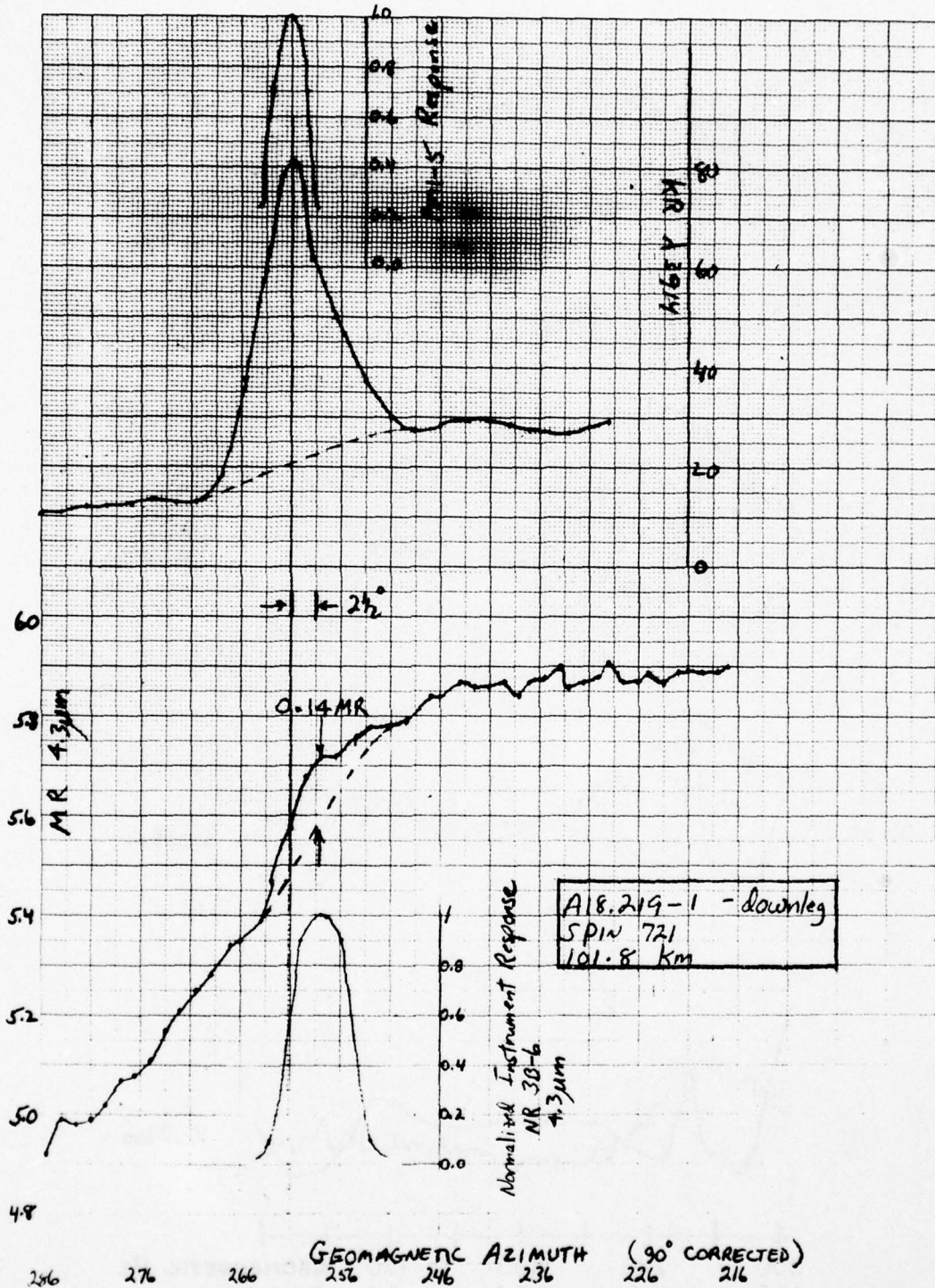


Figure 14. Detail of region near 260° geomagnetic azimuth for Spin 721 on downleg of A18.219-1 showing the correlation between 3914 Å and the 4.3µm "bump." Also shown are the angular response functions of the two instruments.

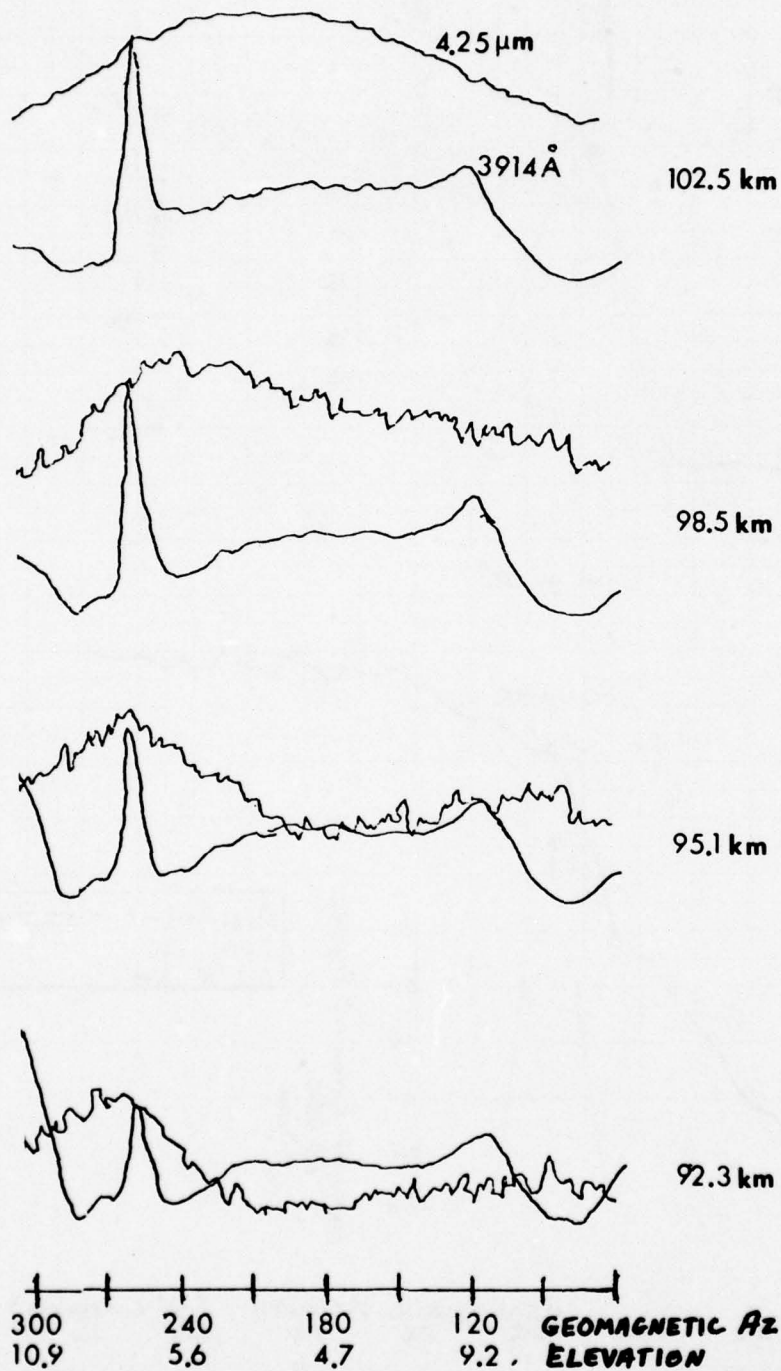


Figure 15. Comparison between 3914 Å and 4.3 μm radiances for the region near 260° geomagnetic azimuth at various altitudes on downleg of A18.219-1.

When the rocket was at 100 km altitude (360 sec after launch) on downleg, it is 40° north of the zenith as viewed from Poker Flat and about 45° south of the zenith as viewed from Fort Yukon. The Poker Flat meridian scanning photometer (Fig 16) shows an intense region with three peaks running from about 45° north of its zenith to 85° north, with the peaks centered at 60° , 70° , and 80° north. There is also a weak arc (as viewed by the MSP) which is centered at 30° north of the zenith. These features are consistent with the all-sky views. The position of the rocket is also shown in the all-sky photograph at about 75 km south of the center of the first of three northern arcs and about 30 km north of the center of the arc to the south of it. Looking again at Fig 13, when the geomagnetic azimuth of the rocket photometers is to the north, the photometer elevation is approximately 15° , while when it is to the south the elevation is 5° . Projecting the look angles into the near-vertical planes containing the two arcs under discussion yields intercepts at 118 km altitude for the first arc to the north and 102 km altitude in the arc to the south when the rocket is at 100 km altitude downleg). The projection into the two additional arcs to the north is at much higher altitudes. This explains why the visible radiances toward the south appear much more intense than those to the north in Fig 13, since the intercept of the photometer field on the near-vertical plane to the north is well above the altitude of peak emission rates. Similar azimuthal scans taken at lower altitudes show the intensity to the north rising rapidly as the photometer intersection moves closer to the altitude of peak emission, while the intensity to the south decreases slowly as it moves below the altitude of peak emission.

The sharp feature at the western edge of the southern scan (260° geomagnetic) in the 3914 Å and 5577 Å channels of Fig 13 is explained primarily by the usual east-west enhancement seen as fields line up with the direction of the arc to the south. This enhancement is higher to the west due to the bright region which is observable in the all-sky photograph (Fig 16) to the southwest, and also because the elevation

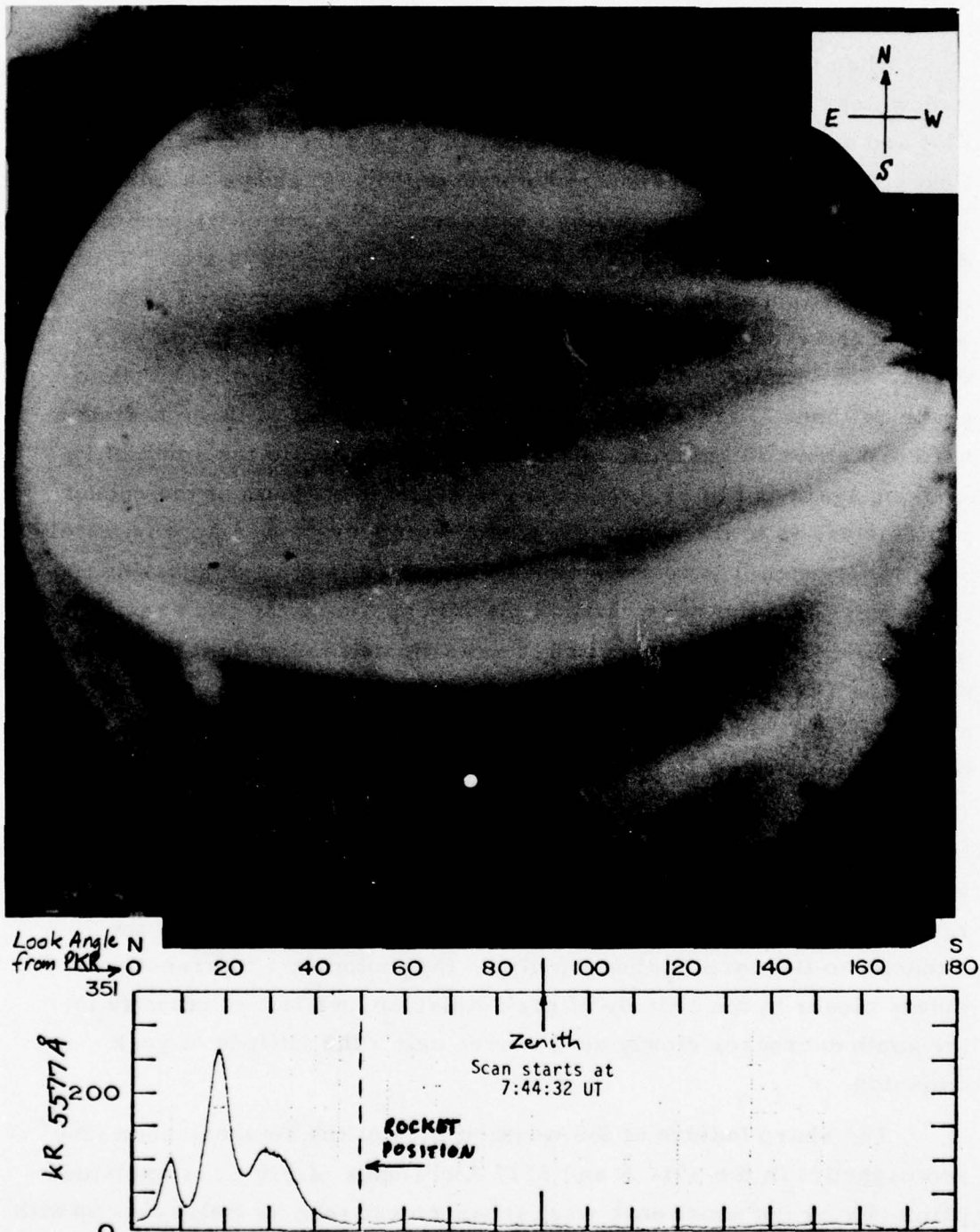


Figure 16. Fort Yukon all-sky camera photograph at 368 seconds after launch of A18. 219-1 with the position of the rocket (●) indicated. Also shown is the Poker Flat meridian scanning photometer data at 362 seconds, with the rocket position noted (scan from Ref 3's Reference 11).

angle is lower to the west. The general east-west characteristic enhancement agrees with enhancements seen in earlier flights (Ref 3, Fig 15) of sidelooking narrow-angle photometers.

CORRELATION WITH 5199 Å PHOTOMETER DATA

Fig 17 shows a scan from the wider 5199 Å channel taken at 118 km downleg compared with a scan from the 4.3 μm channel taken at 94 km. It can be seen that the broadened emission feature in the 4.3 μm channel centered around geomagnetic west correlates in angle extremely well with a broad feature on the 5199 Å channel at the higher altitude. The 3914 Å and 5577 Å radiances do not demonstrate this broad feature. The intensity observed in the narrow (10 Å) 5199 Å channel near 118 km is approximately 0.17 kR above background. Since the 3914 Å channel shows little change over much of the feature at this altitude, we can assume that the excess above background is primarily due to N²D emission, as discussed in Section IV. This is consistent with the apparent higher altitude production of N²D, since 3914 Å would be seen to peak at much lower altitude. Indeed, 3914 Å does show a slight indication of a broad feature in this angular region at the lower altitude, upon which the sharp feature is superimposed.

DISCUSSION OF SOURCES OF 4.3 μm EMISSIONS

The bulk of the signal observed in the 4.3 μm channel is almost certainly due to radiation by CO₂ excited by resonance transfer from vibrationally excited nitrogen, as discussed in Section I. However, the enhancement at 260° azimuth above the smoothly varying background at the higher altitudes (102 km) is quite sharply defined in azimuth, having an angular spread comparable to the angular response of the photometer. This would indicate, at least for the region viewed at a rocket altitude of 102 km, that the reaction causing the observed radiation must be relatively "prompt" in order to maintain its strong correlation with the 3914 Å fluorescence emission.

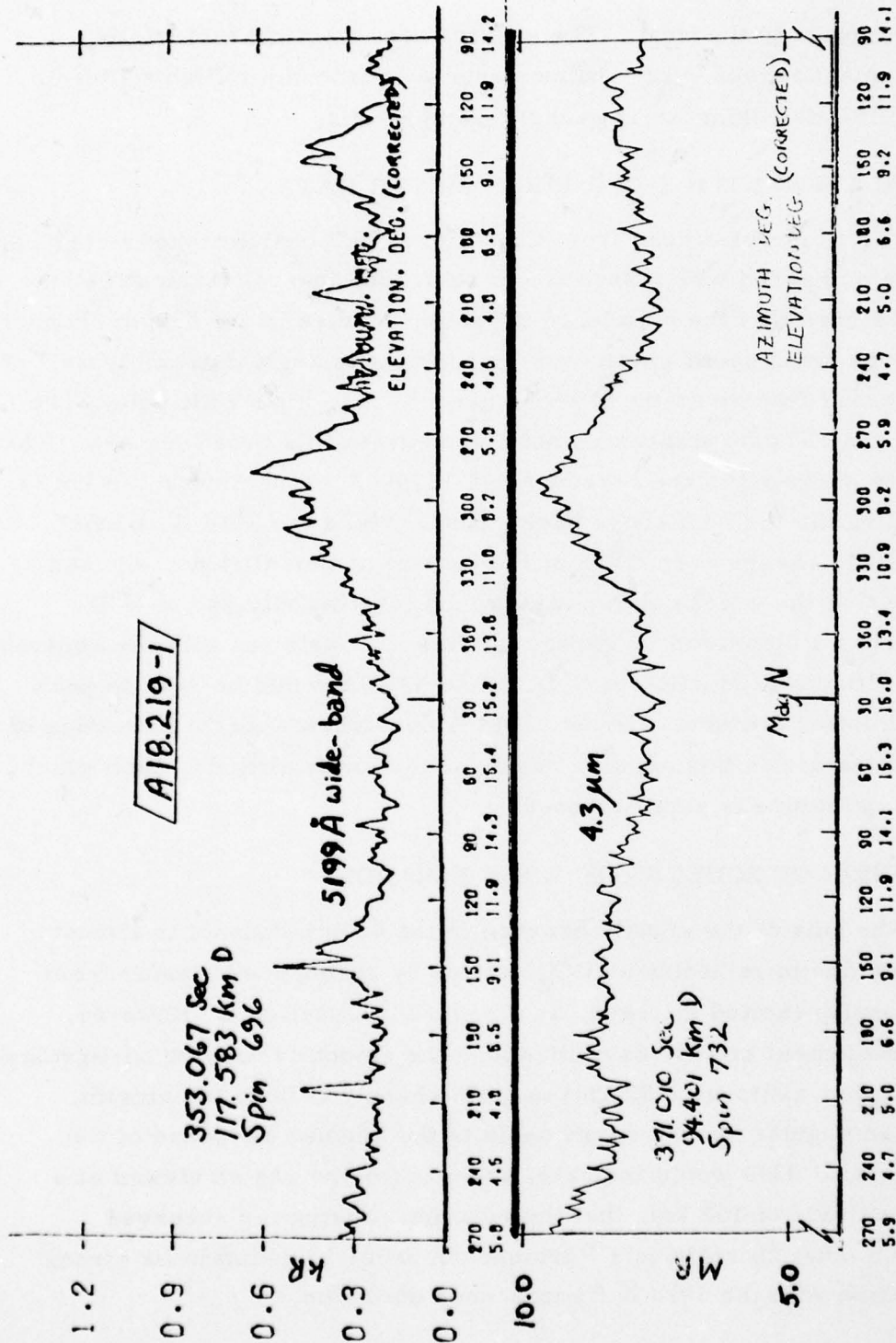


Figure 17. Comparison between the 5199 Å channel at 118 km and the 4.3 μm channel at 94 km on downleg of A18.219-1.

The broadened feature at the lower altitudes in the $4.3\mu\text{m}$ channel may perhaps be explained as due to rather lengthy predosing by exciting particles that have the apparent angular extent exhibited by the higher altitude N^2D as seen in the 5200 \AA channel. This predosing, perhaps with some diffusive broadening, would start the reaction chain that leads to the $4.3\mu\text{m}$ emission feature which peaks near 94 km rocket altitude.

There are at least three potential candidate reactions to explain the prompt sharp $4.3\mu\text{m}$ feature at the higher altitude. These are (Ref 3) radiation from excited NO^+ , radiation from the excited isotopic molecule $\text{N}^{14}\text{N}^{15}$, and direct production of excited CO_2 by electrons. Fig 18 illustrates the emission spectra related to these various possible contributors. The figure also shows the passband of the radiometer. It can be seen that there is some sensitivity to all three emissions, with the lowest sensitivity to the equally populated model of NO^+ and to the $\text{N}^{14}\text{N}^{15}(1,0)$ band radiation.

From Fig 14, the signal seen in the $4.3\mu\text{m}$ channel at 260° geographic west has an excess of approximately 140 kR over the expected level assuming an effect due to elevation angle only. It is possible to make some estimates for the efficiency for producing $4.3\mu\text{m}$ radiation through each of the three production channels indicated by making certain simplifying assumptions.

If we assume the prompt feature is due to radiation from NO^+ , by referring to Fig 18 we can calculate the detection efficiency by examining the overlap of the instrument spectral response with the NO^+ spectral characteristics. The instrument function overlaps about 40% of the spectral energy of the NO^+ emission if the (1,0) model is used and only about 15% of the emission if the ($v = 0 - 10$) equal population model is used. Applying these factors yields corrected values of 0.35 MR and 0.95 MR respectively for the two models. The intensity in the 3914 \AA peak at this time is approximately 70 kR. This yields approximately 5 photons at $4.3\mu\text{m}$ per 3914 \AA photon, assuming the (1,0) model and approximately 14 photons per 3914 \AA photon assuming

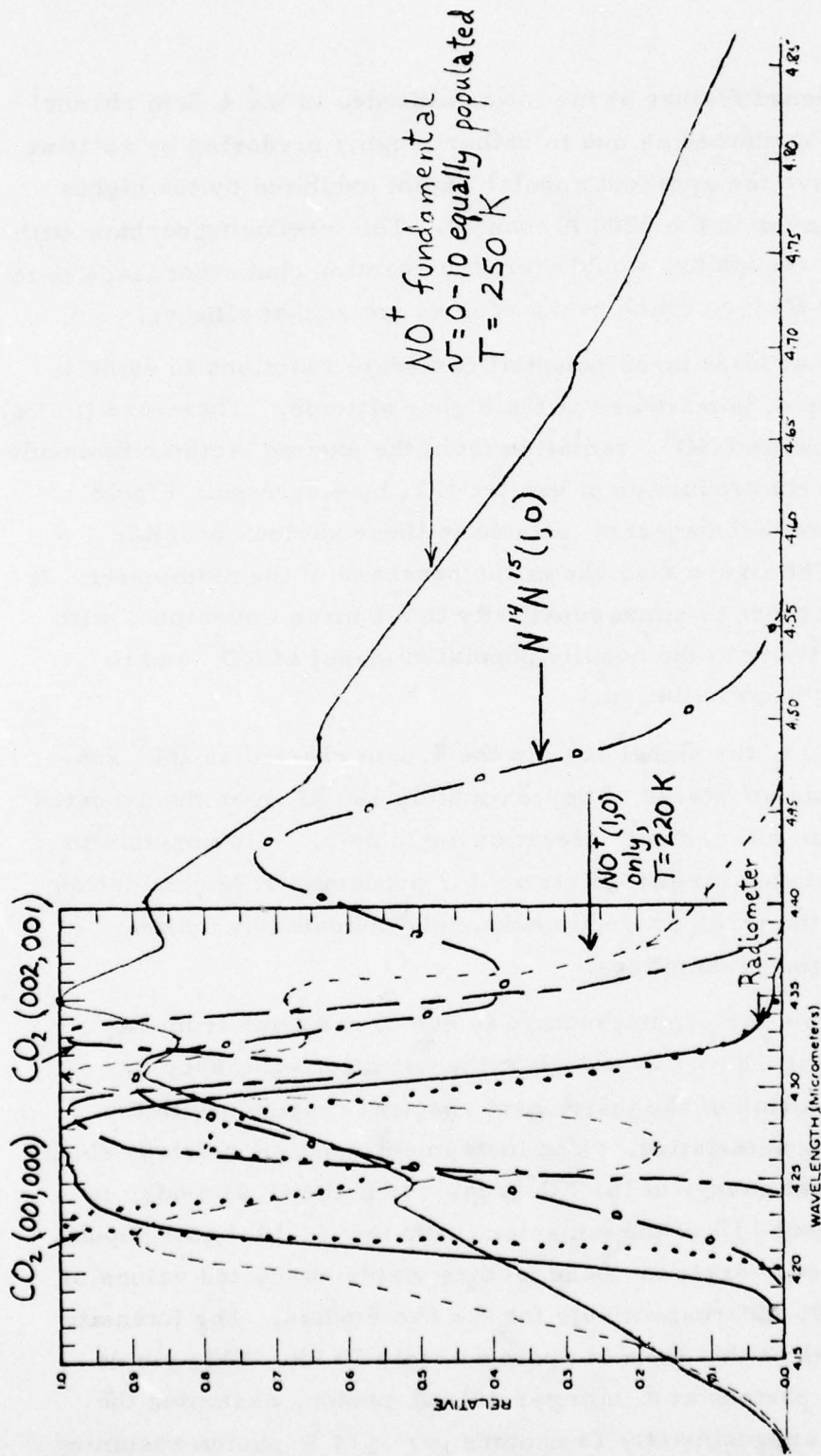


Figure 18. Emission spectra calculated and approximated for the fundamental of NO^+ with equal populations of $v = 0-10$ and $\text{NO}^+(1,0)$ only, CO_2 for $\text{N}^{14}\text{N}^{15}(1,0)$ and $(002,001)$ transitions, and the $\text{N}^{14}\text{N}^{15}(1,0)$ transition. Also shown is the spectral response characteristic of A18.219-1's Sidelooking "4.3 μm " radiometer.

the ($v = 10$) equal population model. This yields effective fluorescent-chemiluminescent efficiencies of about 0.2% and 0.5% respectively (quenching is believed to be a factor at auroral particle-deposition altitudes), using a $\sim 0.4\%$ 3914 Å fluorescent efficiency (Section V of Ref 3).

If we assume that the observed prompt component is due to radiation in the (1,0) band of $N^{14}N^{15}$, the convolution of the instrument response with the vibration-rotation spectrum yields a detection efficiency of approximately 30%. This, in turn, gives an $N^{14}N^{15}$ fluorescence(-vibrational luminescence or -chemiluminescence) efficiency of approximately 0.25% for the volume viewed from 102 km rocket altitude under the auroral dosing conditions of A18.219-1 downleg. (Refer to pp 105-106 of Ref 3 for further discussion of the $N^{14}N^{15}$ molecule's radiative properties.) We will forego a discussion of a prompt CO_2 component because of its uncertain mode of production.

CONCLUSION

The salient points of this discussion of the particle excitation-correlated 4.3 μm features are the indication of a prompt component in several scans below 102 km and the very distinct correlation of a broadened feature at lower (94 km) rocket altitude, whose shape and relationship to 3914 Å-fluorescence are shown in Fig 15, with a similar broad feature in the 5199 Å photometer channels at higher (118 km) rocket altitude. This would appear to couple the N^2D production with whatever mechanism(s) produce the lower altitude 4.3 μm feature. A more exhaustive assessment of the predosing west of the radiometer, with improved estimates of the range to the field lines and thus the altitude above the descending rocket, would better define the source of this 4.3 μm radiation. The procedure for determining the spatial distribution of predosing is that described for the HIRIS spectrometer, in Section V (in addition, altitudes near the meridian can be determined from spectroscopic ratios, as noted in Section VI).

Future rocket investigations should include instruments - narrow-wavelength radiometers and/or spectrometers - to obtain high resolution spectral information between $4\mu\text{m}$ and $5\mu\text{m}$ in low-elevation angle scans (refer to Fig 18). Such instruments would in principle reach useful fluorescence-associated signal/ CO_2 background ratios over broader azimuth ranges in the auroral particle-excited ionosphere. It would be cost-effective to point radiometers at several elevation angles from the same sounding rocket, better to assess the altitude distribution, and thus the quenching, of this component of the "4.3 μm " emission. Because of the apparent connection to $[\text{N}^2\text{D}]$, a 5199 Å differential photometer should be among those aligned with the infrared spectro-radiometers' field. In addition directly-quantitative all-sky photography would improve measurement of the off-meridian predosing.

SECTION III

FILM RESPONSE PHOTOMETER, IC519.07-1B

FUNCTION

A photoelectric photometer designed (by AFGL/OPR staff) to have wavelength response matching that of calibrated photographic cameras that recorded the spatial radiance distributions of the persistent sky-glow excited by the Fishbowl (1962) high-altitude nuclear explosions, was coaligned with the sidelooking radiometers and photometers on ICECAP "multi" rocket IC519.07-1B. The purpose of this film response photometer (henceforth referred to as FRP) is to link the infrared emissions from auroral particle-stimulated air measured from the rocket to this existing body of optical photometry data, so as to allow the infrared sky backgrounds excited by nuclear particles to be scaled to the known visible backgrounds. An FRP, viewing in the zenith, will also be used in the forthcoming HAES-program measurements from an aircraft of the spatial and spectral distribution of radiation near $2.8\mu\text{m}$ from the auroral ionosphere. The purpose of this preliminary review of the sidelooking FRP data from the rocket flight is to evaluate and verify the performance of this "transferring" instrument in terms of the radiances measured by visible aurora-sensitive photometers that viewed the same volumes of particle-excited air.

INSTRUMENT CHARACTERISTICS

Fig 19 shows the relative spectral sensitivity of the FRP as realized and the design-goal characteristic for a combination of film and lens typical of that used in Fishbowl Project 8A.1 and 8A.2's cameras. The film is Eastman Kodak Tri-X Pan, and the lens is representative of the fast, short focus types effective for late-time photography of afterglows that cover wide angles of sky (for example the Nikkor 55mm f/1.2 as used with full-frame 35mm format). Since no correction was attempted for the wavelength dependence of Rayleigh

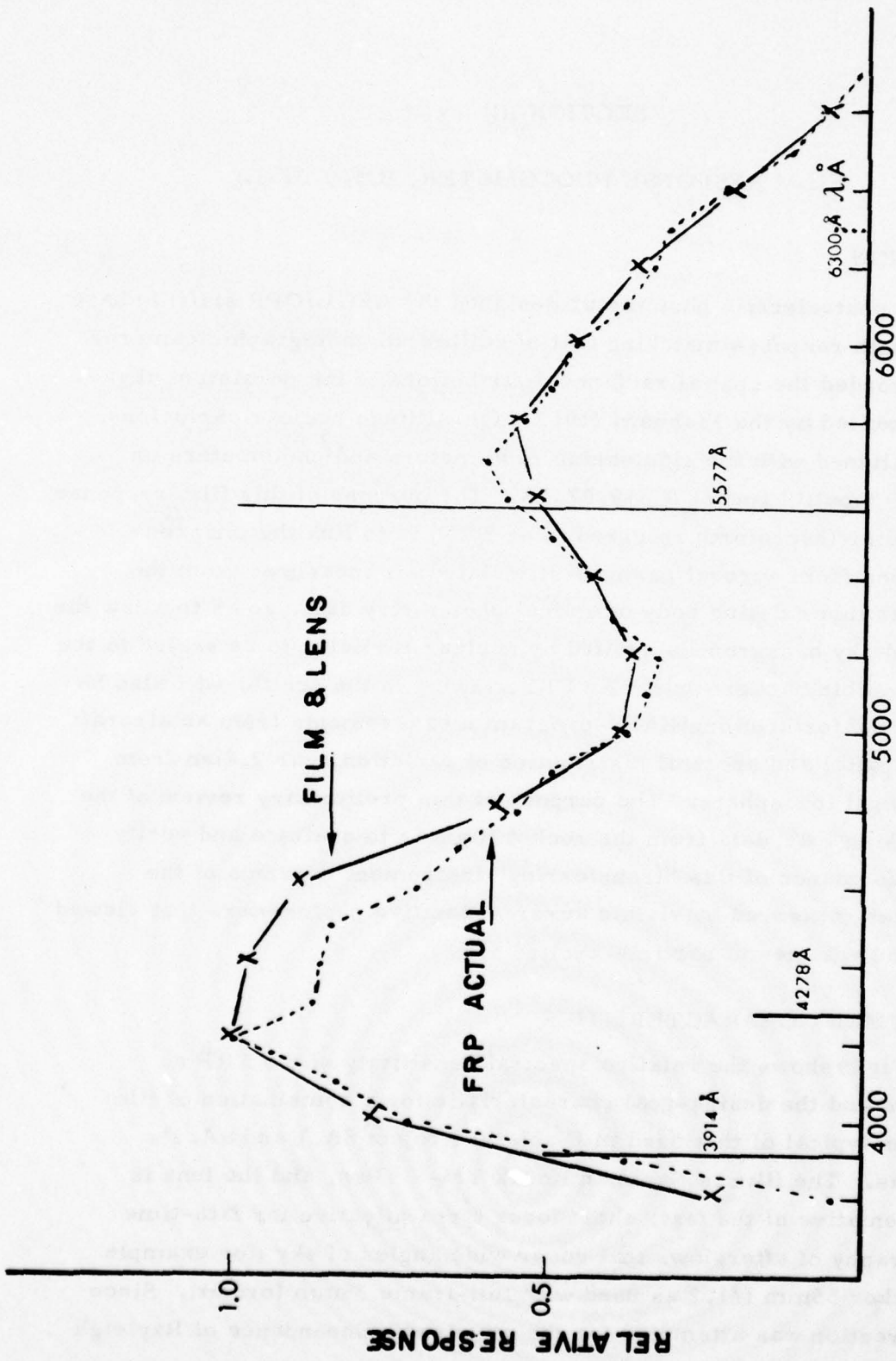


Figure 19. Relative photon response of the Film Response Photometer compared to that of Eastman Kodak Tri-X Pan film used with a fast wide-angle lens (see text). The vertical bars represent typical relative column intensities (as viewed from below) of the major auroral features in the FRP's wavelength range.

and Mie scattering of bomblight by the intervening lower atmosphere, which is in any case variable with elevation angle and meteorological conditions, The FRP's results apply best to the photography from KC-135 aircraft flying at ~35 kft. From this altitude the effects of outscattering are important only for narrow-angle radiating sources lying at low elevation angles.

The ordinate in Fig 19 is the relative output current from the photometer per unit monochromatic scene radiance (in photon units, for example Rayleighs per Å) at the wavelengths indicated on the abscissa. This characterization differs somewhat from that applied to photographic film, whose spectral sensitivity is expressed as the inverse of the monochromatic fluence that produces a given optical density after standard development, (erg/cm^2 for $D = 0.1$ above fog, or for some fixed total density)⁻¹. There are, in addition, further differences between the response of the logarithmically-integrating photographic film and that of its simulating photoelectric detector.

ANTICIPATED RESPONSE OF THE FRP

Fig 19 also shows the approximate relative intensities of the brightest auroral features in the FRP's spectral range, viewing the excited volume from below. The OI green line is emitted from somewhat higher altitudes, and the strongly-quenched OI red doublet originates at considerably higher altitude than the N_2 and N_2^+ fluorescence bands; this effect is the basis for assessing the energy distribution of the incoming charged particles (Ref 12). Very roughly speaking, the column emission in the photographic-visible excited by auroral electrons having the typical characteristic energy 2-10 keV is about half in OI 5577 Å chemiluminescence-fluorescence photons and one quarter in impact-excited N_2^+ 3914 Å First Negative band photons, with all the other spectral features contributing the remaining one-quarter of the quanta over this wavelength range. The 5577 Å radiation lags the instantaneous energy deposition by ~ 1/2 sec, the actual time

dependence of emission varying in a complex way with altitude and time integral of ionization rate. In addition there is a weak persistent chemiluminescent continuum from the $\text{NO} + \text{O}$ reaction, which results from predosing rather than the immediate local particle bombardment (Section IV).

This partial auroral spectrum leads to the expectation that the FRP's signal when the rocket is below most of the excited region would by and large follow that from the 5577 Å and 3914 Å photometers, in particular under intense auroral bombardment and at low zenith angles (for which the path length through the continuum-emitting layer is not excessively long). The correlation with 5577 Å emission would be better at higher rocket altitudes, and the 6300 - 6364 Å doublet provides an increasingly important contribution at very high rocket altitudes and large fluxes of soft electrons. We apply this rough model of the FRP's response to average aurora in our review of its performance.

ROCKET TRAJECTORY AND ORIENTATION

The location of the relatively diffuse auroral emission viewed by the rocket instruments is shown on the plot of the trajectory of IC519.07-1B (launched 0748:10, 12 Mar 75), Fig 20. A stable arc system formed near the PKR zenith before launch, and its central field line (indicated by + in Fig 20) remained south of the rocket during the measurement period; see the All-sky camera views in Fig 57 of Ref 3. The rocket was attitude-stabilized to only a few degrees, as the plot of the sidelooking instruments' altitude dependence of elevation angle shows (right side of Fig 22), so that in the magnetic meridian (for example) elevation varied between -0.5° and $+3.9^\circ$ over the flight. Therefore the altitude at which the fields-of-view of the FRP and its coaligned photometers and radiometers intercept the excited volume at a given look azimuth varies cyclically with the rocket's altitude. The rocket's spin rate was 1.4 rev's/sec, and the plane of its trajectory lay very close to the geometric meridian.

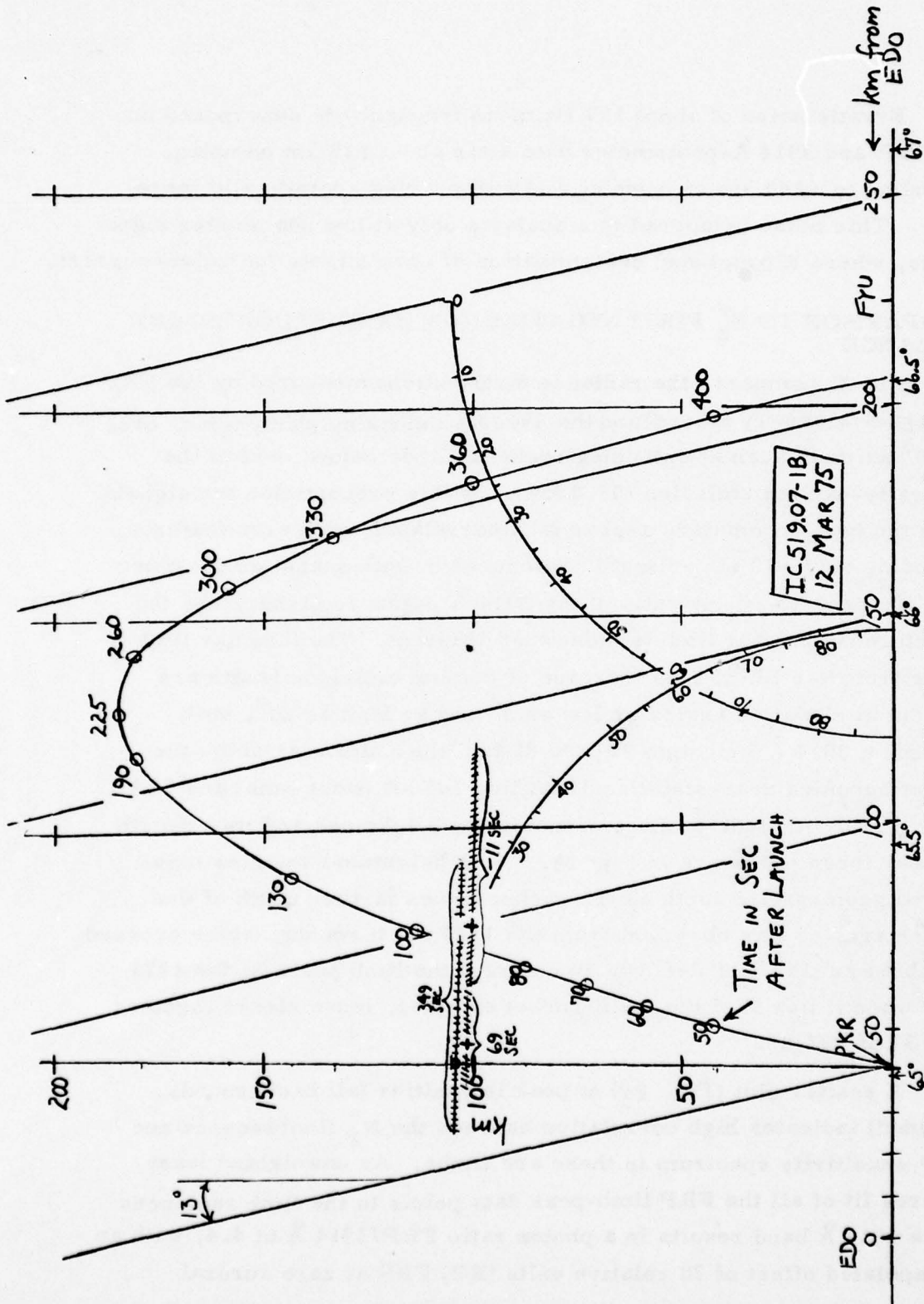


Figure 20. Trajectory of IC519.07-1B with estimated location of the "center" (marked +) and north-south extent of the diffuse auroral arc. See also All-sky views in Fig 57 of Ref 3.

Erratic noise of about 100 Hz mean frequency is superposed on the FRP and 3914 Å-photometer data after about 115 km on upleg, extending to ~140 km on downleg and reappearing sporadically thereafter. This noise hampered this analysis only at low photometer signal levels, where it precluded determination of zero offsets due to dark current.

COMPARISON TO N_2^+ FIRST NEGATIVE (0,0) BAND FLUORESCENT RADIANCE

Fig 21 compares the radiance distributions measured by the FRP (high gain telemetry record) and the 3914 Å sidelooking photometer, over a 540° azimuth scan at one upleg rocket altitude below most of the aurorally-excited emission (93.4 km). In this presentation the signals from the two photometers appear well correlated, with even features extending only ~10° in azimuth reproduced in both scans; on the other hand the peak-to-valley ratio of the 3914 Å signal is higher, and the structure in the east limb is somewhat different. The familiar limb peaks from van Rhijn-type increase of column emission length are present at elevation angles as low as 3° and as high as 20°, with maximum 3914 Å brightness above 80 km (the altitude at which the rocket becomes near-stabilized) reaching 141 kR (west limb) and 76 kR (east limb). Altitude profiles of maximum brightness and its azimuth angle at these peaks are in Fig 22. Both brightness maxima move toward geomagnetic south as the rocket moves farther north of the diffuse arc, as was observed from the 1973 multi rocket, which crossed a stable arc (Fig 3 of Ref 3); in contrast the limb peaks of the 1974 arc, when it lies N of the multi rocket on upleg, move closer together (Fig 37 of Ref 3).

A scatter plot (Fig 23) of peak intensities (all backgrounds included) indicates high correlation between the N_2^+ fluorescence and FRP-sensitivity spectrum in these arc limbs. An unweighted least squares fit of all the FRP limb-peak data points to the limb radiances in the 3914 Å band results in a photon ratio FRP/3914 Å of 4.4, with an extrapolated offset of 78 relative units (RU) FRP at zero auroral

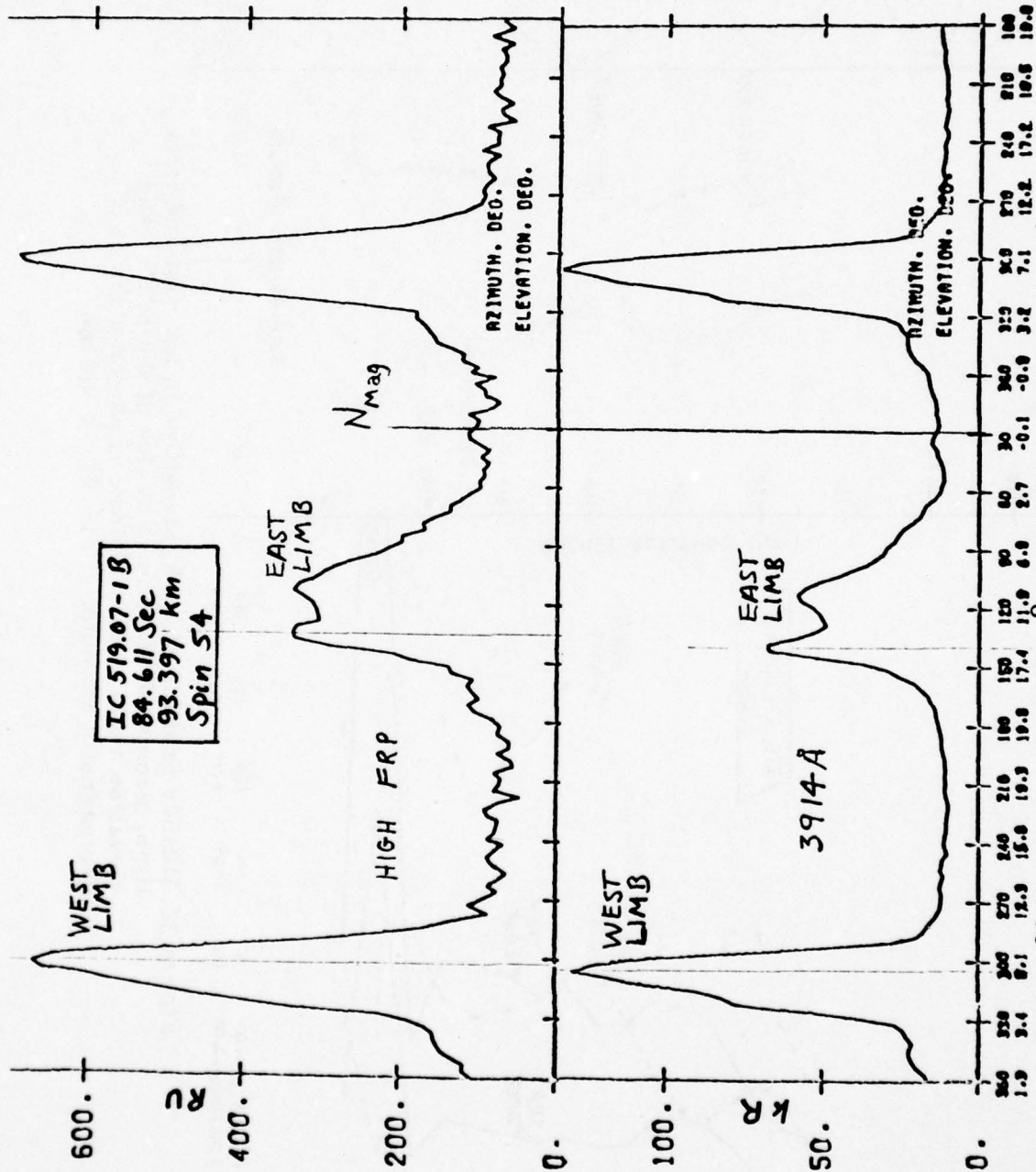


Figure 21. Representative 3914 Å and FRP elevation-a-zimuth scans from upleg of IC519.07-1B, showing qualitative correlation of the two radiance distributions.

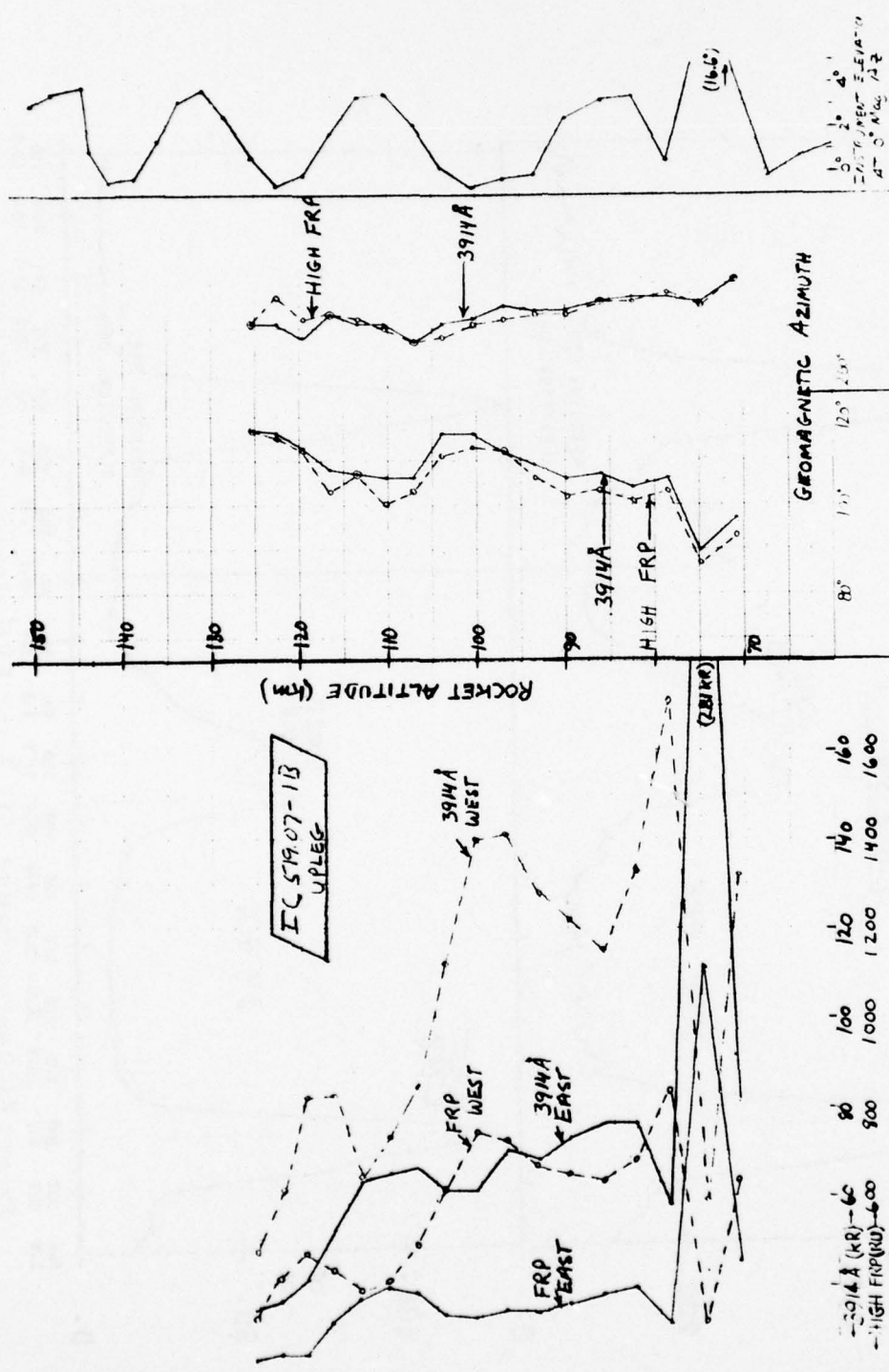


Figure 22. Altitude profiles of peak intensities in the east and west limb, geomagnetic azimuth angles of the peaks and elevation angle of the sidelooping photometers at 0° geomagnetic azimuth, IC519.07-1B upleg.

bombardment, or $-18 \text{ kR } 3914 \text{ \AA}$ at 0 RU FRP. (This offset is a quantitative expression of the peak-to-valley ratio difference noted in the previous paragraph.) Taking the FRP's bandwidth as 1500 \AA (see Fig 19); the mean continuum nightglow intensity as 1 Rayleigh/\AA over its sensitivity range (which is conservative for high latitudes, where [NO] can be enhanced); and a mean van Rhijn gain factor of 6 for the elevation angles at which the data are taken, we find that the continuum makes a contribution of 9 kR-equivalent to this latter offset. While this figure does not quantitatively explain the zero-offset, it does suggest that the airglow continuum is at least partially responsible for it.

Since the data taken when the rocket was below 100 km altitude (which correspond to higher intercept altitude on the arc) constitute the majority of the readings and lie at generally higher radiances, they dominate placement of the least-squares fit line. We therefore also treat separately the higher-altitude data (not underlined in Fig 23), since 1) the relative contribution to the FRP signal from 5577 \AA photons decreases more steeply below 100 km (Ref 12) and 2) the contribution from the nightglow continuum should decrease very rapidly above 100 km. For these data points the slope is $5.0 \text{ (RU/kR } 3914 \text{ \AA)}$ and the $\text{FRP} = 0$ intercept -11 kR . This higher slope is expected on the basis of the decreasing relative excitation of N_2^+ fluorescence previously noted. The smaller intercept value is at least in part due to the great reduction in $\text{NO} + \text{O}$ continuum radiance when the sensor is above 100 km.

Fig 24 is a scatter plot of $\text{FRP}-3914 \text{ \AA}$ intensities over three complete 360° spin cycles, at the representative rocket altitudes 97, 110, and 139 km. Samples were taken at 10° azimuth intervals, and where the data were noisy they were averaged over about 5° in azimuth. The unweighted least squares fit of FRP to 3914 \AA radiance more closely approaches the origin than the fits in Fig's 23 and 26, the offset being -5 kR taking all data points. The slope using all data points is 5.2, significantly higher than that derived from all the isolated auroral limb radiances (see the comparison line on Fig 24). As expected this slope is

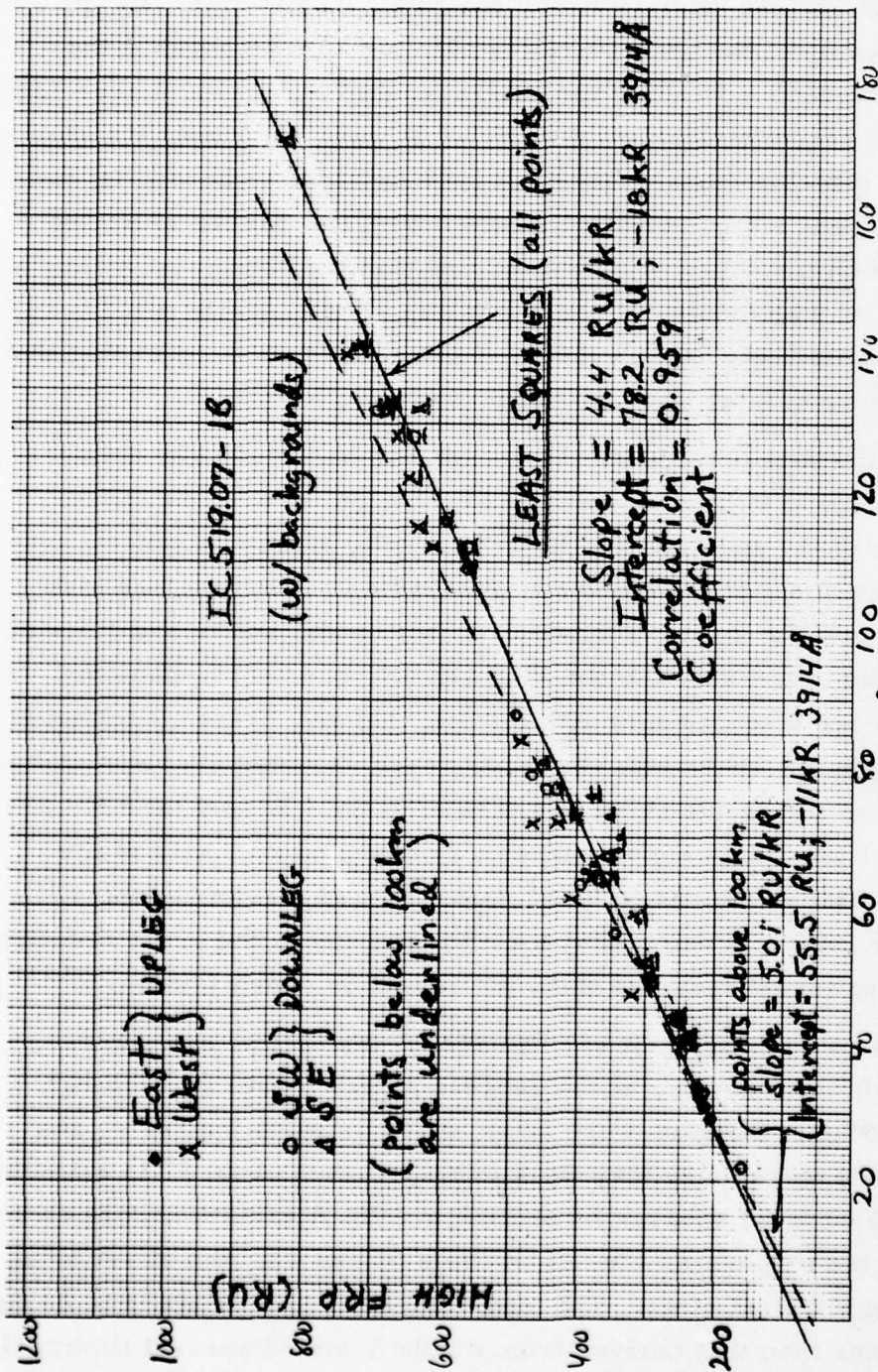


Figure 23. Scatter plot of 3914 Å and FRP limb peak intensities (background included), with a least squares fit to the 3914 Å readings, IC519.07-1B.

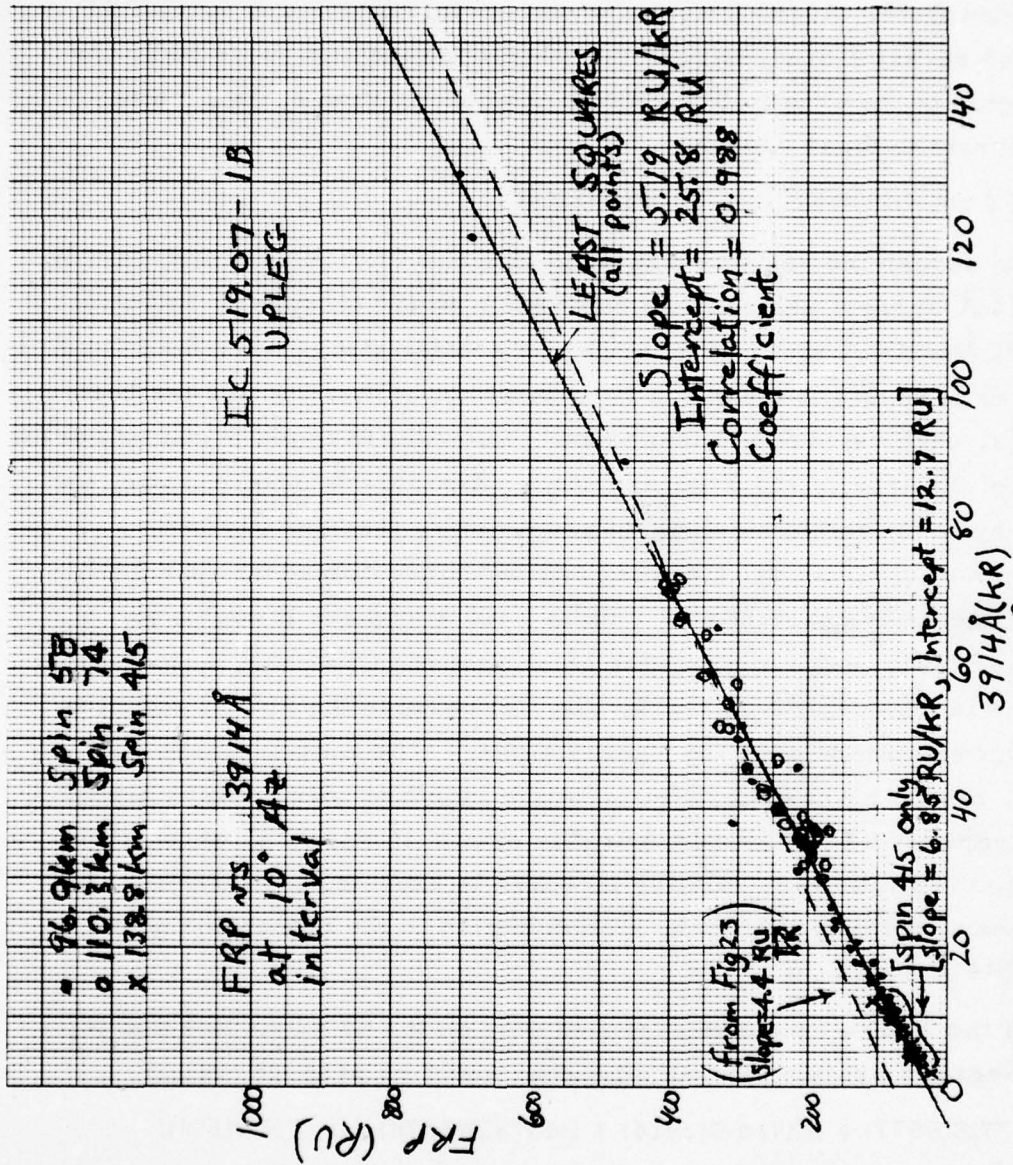


Figure 24. Scatter plot of 3914 Å and FRP intensities (background included) at 10° azimuth intervals over three 360° spin cycles of IC519.07-1B on upleg, with least squares fits.

markedly higher when the rocket is at 139 km. Furthermore the intercept drops to < -2 kR 3914 \AA , which is large in comparison to what would be expected from any OI red-line (metastable) emission remaining in the instrument field. At the lowest fluorescent intensities measurable (at very high rocket altitudes) above the aforementioned noise, ~ 2 kR, the FRP signal is too erratic to establish the contribution of its phototube's dark current to these offsets.

EFFECT OF OI GREEN LINE EMISSION

To assess the relative contribution to the FRP signal from 5577 \AA and 3914 \AA auroral photons, we compiled altitude profiles of FRP/ 3914 \AA and $5577 \text{ \AA}/3914 \text{ \AA}$ ratios (Fig 25) and a scatter plot of $5577 \text{ \AA} - 3914 \text{ \AA}$ radiances (Fig 26), for the arc limb maxima. (The data are the peak readings, unadjusted for "background" below the isolated maximum or for offsets of the type in Fig's 23 and 24). The $5577 \text{ \AA}/3914 \text{ \AA}$ ratio, as viewed by the rocket's sidelooking photometers (see our earlier comments on their actual elevation angles and arc-intercept altitudes), remains sensibly constant at 1.3 up to ~ 105 km where it begins to increase slowly. The slope of the least-squares fit of 5577 \AA to 3914 \AA radiance is somewhat less (1.22, Fig 26) because the 5577 \AA signal is zero-shifted upward about $8\frac{1}{2}$ kilorayleighs. The radiance ratio FRP/ 3914 \AA , however, shows a greater relative increase with rocket altitude (compare the $3 \times 5577 \text{ \AA}/3914 \text{ \AA}$ profile drawn in Fig 25), which starts at 95 km. This larger relative increase is expected because the N_2^+ fluorescent intensity maintains a contribution to the numerator of the FRP/ 3914 \AA ratio.

If the FRP's response depended only on the OI green line and N_2^+ First Negative system, its output signal would be proportional to

$$I(5577)S(5577) + I(3914)S(3914) + I(4278)S(4278) + I'(FN)\bar{S}(FN),$$

where the I's represent the relative photon intensities of the features and the S's the sensitivity of the FRP at the indicated wavelengths. The last term in the expression above makes a small additive correction for the bands of the First Negative system other than (0,0) with head at

IC 519.07-1B (backgrounds included)

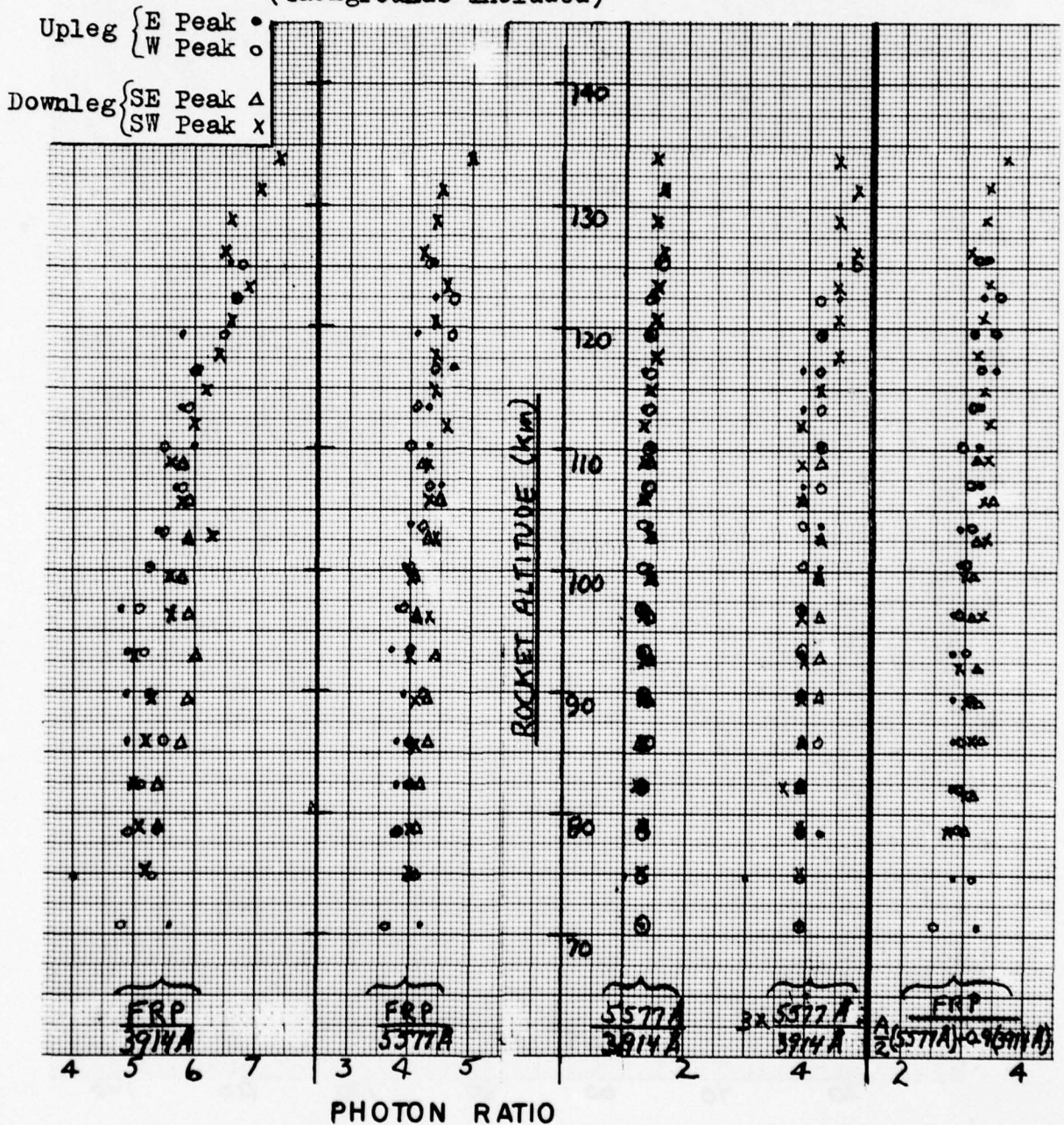


Figure 25. Altitude profiles of FRP/3914 Å, FRP/5577 Å, and 5577 Å/3914 Å limb peak intensities, and FRP/ (weighted sum of 5577 Å and N₂ fluorescence) as defined in the text, IC519.07-1B.

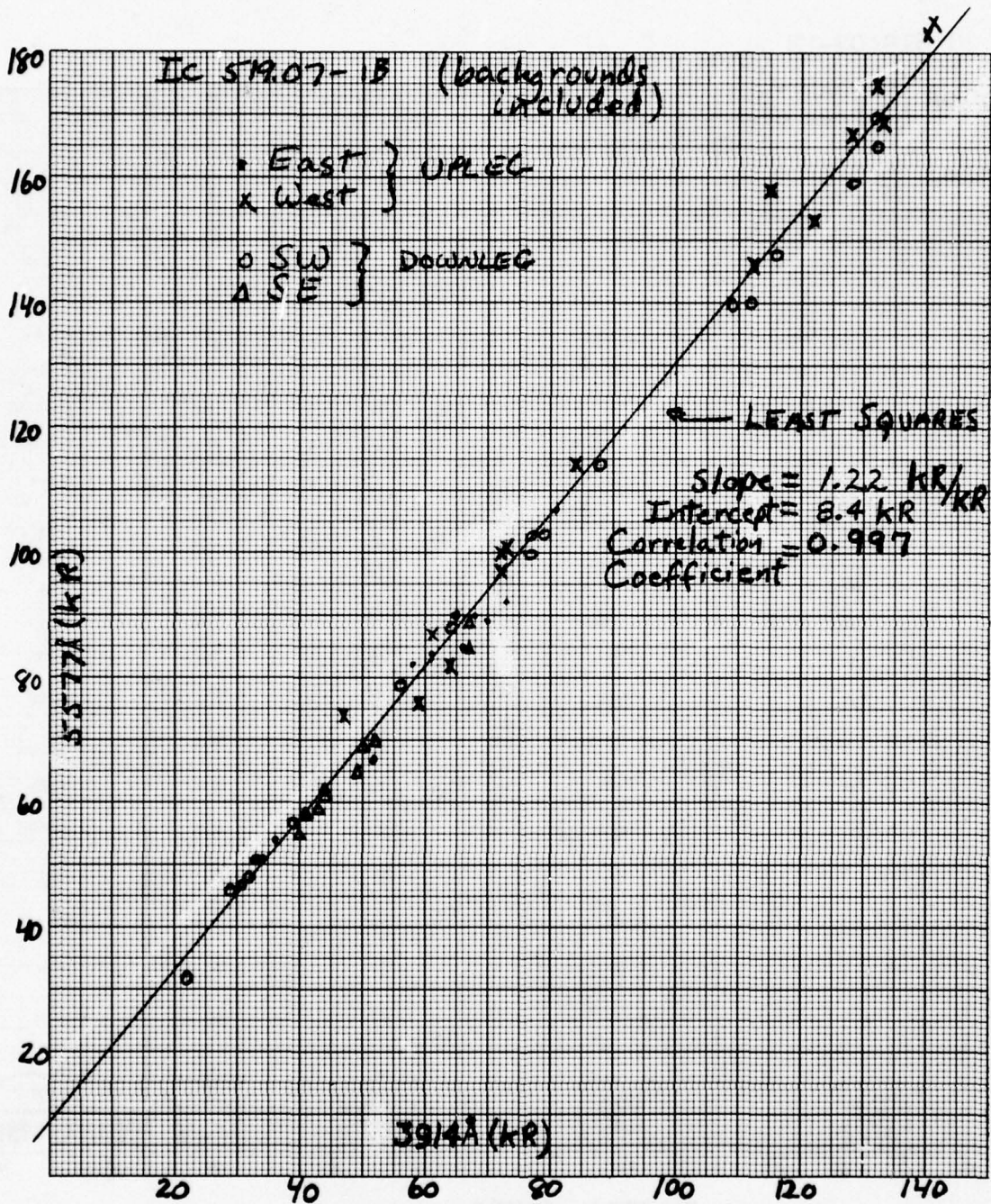


Figure 26. Scatter plot of 5577 Å and 3914 Å limb peak intensities (background included), with a least squares fit to the 3914 Å readings.

3914 Å and the 0.34-as-intense (0,1) at 4278 Å, in which are emitted ~1/6 as many photons as at 3914 Å. Applying the spectral response in Fig 19, this expression becomes

$$\frac{A}{2.0} I(5577) + 0.9 I(3914) \equiv \Sigma ,$$

where A is the measured altitude-dependent ratio $I(5577)/I(3914)$ (or as we have been labeling it $5577 \text{ \AA}/3914 \text{ \AA}$) plotted in the center of Fig 25. The ratio FRP/Σ , at the right of Fig 25, shows a slow increase with altitude. This observation indicates that aurora-associated emitters whose intensities are not proportional to the FRP sensitivity-weighted sum of OI 5577 Å and N_2^+ First Negative band, are contributing relatively more photons to the film response photometer as the altitude of energy deposition increases (or alternatively, less with decreasing deposition altitude). Presumably these sources include metastable radiating species, less quenched at the higher altitudes.

SUMMARY, APPLICATION TO USE OF THE FRP ON AIRCRAFT

The ratio FRP/Σ in Fig 25 gives an indication of the departure of the FRP's response to actual auroral emission from its calculated response to high altitude air's two major visible features, for the viewing geometry of arc limbs. Fig's 23 and 24 show experimentally significant differences between the quantity that panchromatic film with fast wide angle lenses measures at different excitation altitudes, when this quantity is referenced to the electron impact-excited N_2^+ First Negative Band radiance that is conventionally taken as proportional to the column rate of production of ions by energetic charged particles. (Refer to Section V of Ref 3 for a review of the altitude dependence of this proportionality.) The offset of the FRP signals at low and high altitudes can at least in part be attributed to types of "predosing." No substantive evidence of nonlinearity of the FRP's response with auroral "intensity" at a given altitude - due to changes in volume rate of energy deposition, length of column viewed, or both - is resolvable in the sidelooking photometry data that we analyzed.

Since these results were derived from an isolated (albeit diffuse) auroral arc viewed at low elevation angles ($< 20^\circ$) from near coaltitude, they refer, in effect, to altitude profiles of the FRP's intensity response relative to the radiance of "standard" auroral features. To assess the FRP's performance when it views aurora in the zenith from below the excited volume, as from the aircraft, the rocket data presented here should be weighted by the altitude profile of energy deposition by the incoming charged particles. The usual concentration of this excitation in a height range of ≈ 25 km in the intense aurora most useful for measuring infrared emissions would have the effect of damping the altitude dependences that we observe from the multi rocket. (In addition the contribution of the continuum is small for zenith views.) That is to say, the aircraft FRP's signal from the aurora-excited vertical column would be expected to follow the 5577 Å and 3914 Å photometer signals even more closely than is indicated in the data in this Section. The FRP's response for the aircraft's viewing geometry could of course be more accurately determined by measurements on aurora from a ground station.

SECTION IV

N^2D DIFFERENTIAL PHOTOMETER, A18. 219-1

FUNCTION

ICECAP 1974's multi-instrumented rocket (Sections I and II; Ref 3, Section II) carried a differential photometer whose performance in isolating the N^2D - 4S forbidden doublet 5198.7-5200.5 Å from nearby and overlying fluorescent and chemiluminescent radiations is evaluated in this Section. The radiance in this weak auroral-airglow feature measures the column concentration of atoms in the long-lived metastable upper (2D) state, which, since they react relatively rapidly with ambient O_2 , are considered to be the major precursor of 2.8 μm overtone emission from vibrationally-excited NO molecules. A sidelooking filter radiometer boresighted with the differential photometer measured this infrared emission, as reported in Section II of Ref 3.

Earlier measurements from multi rockets made by single narrow wavelength-band photometers (Ref 1, Section I; Ref 3, Section I) indicated concentrations of N^2D in arcs below ~ 115 km at least an order of magnitude higher than those determined from the ground and aircraft with tilting filter photometers (Ref 1, Section V; Ref's 13, 14). The latter results are consistent with the N^2D state's known short lifetime against collisional deactivation at these altitudes. We interpreted the high readings from the rocket photometers as due principally to leakage to the photocathode of radiation at wavelengths just below the principal passband of the interference filter incident at angles greater than the $2\frac{1}{2}^\circ$ half-angular field (Ref 1, Appendix XV). The conclusion that auroral fluorescence overlapping 5199 Å is not the major source of the large excess signals is supported by ICECAP meridian scans (Ref 1, Section V) from the ground with a well-baffled tilting filter photometer having a passband only ~25% narrower than that of the fixed-filter rocket instrument. The auroral background when the groundbased photometer's sensitivity maximum was located at 5204 Å,

where the N_2^+ First Negative (0, 3) band contributes some signal, was only slightly higher than at 5185 Å, where auroral fluorescence is very weak (more on this point presently).

The differential photometer design is intended to subtract out the in-band contamination by determining its relative intensity over a narrow and a wider wavelength interval. The instrument would compensate adequately for the contribution of photons to the signals arriving from off-axis angles if the out-of-band responses of each of its channels were proportional to their respective bandwidths for all spatial distributions of auroral radiance. (Each channel has the same optical system as the photometer illustrated in Appendix XV of Ref 1; the off-axis transmission is not calculable a priori, and in any case the spurious photocurrents would be expected to depend on the specific spatial distribution.) To evaluate the performance of the differential photometer when viewing aurora at low elevation angles, we have made this preliminary review of the N_2^+ intensity data from the instrument coaligned with the other sidelooking photometers and radiometers on sounding rocket A18. 219-1.

SPECTRAL SENSITIVITY OF THE PHOTOMETER AND DISTRIBUTION OF THE SOURCE

Fig 27 shows the transmission of the differential photometer's narrow-band (10 Å FWHM) and wider-band ($26\frac{1}{2}$ Å FWHM) interference filters, measured at normal incidence; the relative intensity in the N_2^+ - $4S$ forbidden doublet (corrected from Fig 17 of Ref 1); and the relative spectral intensity in the N_2^+ (0, 3) band at 300 K rotational temperature convolved with a 1 Å triangular scanning slit (also from Ref 1). This temperature implies a mean emission altitude at $116\frac{1}{2}$ km (CIRA 72 model atmosphere), which is representative of IBC-II auroral conditions; in any case, the intensity distribution in the lines of the R branch overlapping the filter passbands does not change rapidly enough with ambient temperature to impact detectably this present evaluation. (For peak energy deposition at $116\frac{1}{2}$ km, the

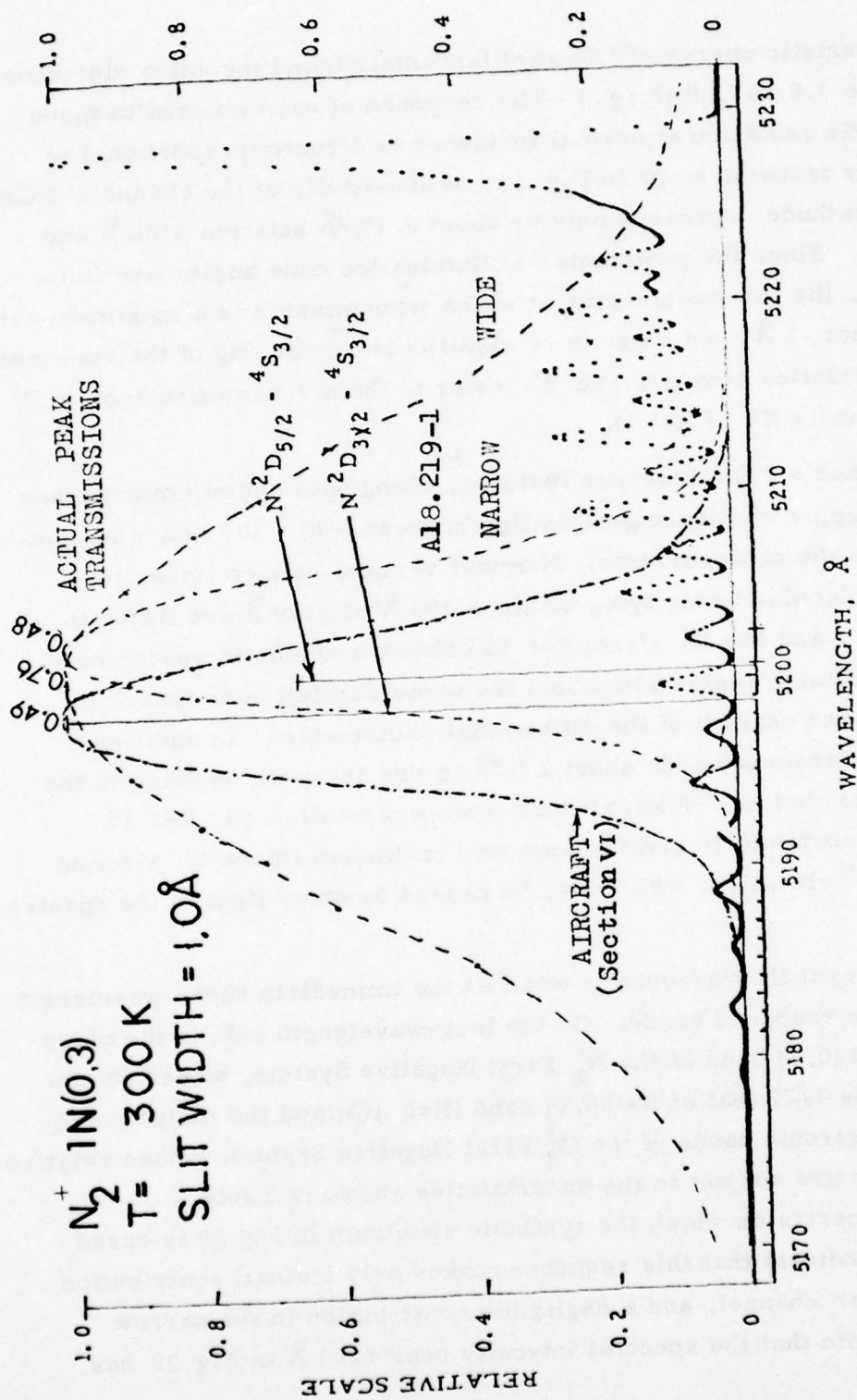


Figure 27. Transmission of the filters in the differential photometer (at normal incidence), and spectra of the $N_2^+ D-S$ doublet and N_2^+ First Negative (0, 3) band.

characteristic energy of "Maxwellian"-distributed incoming electrons would be 3.0 keV, Ref 12.) The response of each channel to monochromatic radiation at normal incidence is directly proportional to the filter transmissions in Fig 27, as sensitivity of the channels' RCA 4516's cathode decreases only by about $0.1\%/Å$ between 5180 Å and 5230 Å. Since the photometer's illumination cone angles are finite (5° full), the two wavelengths at which transmission is a maximum each shift about $-1 Å$, but there is no significant broadening of the response characteristics shown in Fig 27 (refer to the discussion in Section IV and Appendix XV of Ref 1).

Other air fluorescence features, along with chemiluminescence in the airglow continuum originating between $\sim 90 - 100$ km, also contribute to the photocurrents. Nominal vertical column intensities of the molecular bands lying within $\pm 100 Å$ of 5199 Å are listed in Table 1, and Fig 28 (from Ref 15) shows a synthetic spectrum of this wavelength region with about the same resolution as that of the narrow-band channel of the differential photometer. In addition chemiluminescence adds about $2 R/Å$ in this interval, viewing in the zenith from below ~ 90 km altitude (compare Section III; Ref 15 reports substantially greater apparent continuum intensity viewing at $16^\circ - 47^\circ$ elevation, which may be caused by stray light in the spectrometer).

Auroral fluorescence is weak on the immediate short-wavelength side of the response bands. On the long-wavelength side is the aforementioned (0, 3) band of the N_2^+ First Negative System, whose photon intensity is $1/72$ that of the (0, 0) band (Ref 16); and the multiheaded $\Delta v = 2$ electronic bands of the O_2^+ First Negative System, whose relative intensities are subject to the uncertainties shown in Table 1. Auroral spectra on which the synthetic spectrum in Fig 28 is based (Ref 17) indicate that this sequence makes only a small contribution in the wider channel, and a negligible contribution in the narrow channel (note that the spectral intensity near 5200 Å in Fig 28 has

Table 1. Air Fluorescence Bands Near 5199 Å *

<u>Spectral Feature</u>	<u>Band Head Å</u>	<u>Shaded to</u>	<u>Nominal IBCIII R^{**}</u>
N ₂ V-K (4, 17)	5090	Red	230 ^{***}
N ₂ ⁺ 1N (1, 4)	5150	Blue	280
N ₂ ⁺ (M) (7, 1)	5174	Red	80
N ₂ 2P (2, 9)	5179	Blue	30
N ₂ ⁺ 1N (0, 3)	5228.3	Blue	780
N ₂ V-K (5, 18)	5226	Red	170 ^{***}
O ₂ ⁺ 1N (7, 5)	5234	Blue ⁺	< 100, 400 ⁺⁺
O ₂ ⁺ 1N (6, 4)	5241	Blue ⁺	< 100, 200 ⁺⁺
O ₂ ⁺ 1N (5, 3)	5251	Blue ⁺	< 100, 600 ⁺⁺
O ₂ ⁺ 1N (4, 2)	5259	Blue ⁺	200, < 200 ⁺⁺
O ₂ ⁺ 1N (3, 1)	5275	Blue ⁺	1400, 700 ⁺⁺
O ₂ ⁺ 1N (2, 0)	5296	Blue ⁺	1800, 700 ⁺⁺
N ₂ 2P (1, 8)	5309	Blue	30

 * From Ref's 15 and 17 except as indicated. V-K=Vegard-Kaplan band; 1N = First Negative; M=Meinel; 1P, 2P= First, Second Positive. Refer to text for estimate of continuum-chemiluminescence intensity.

** Column intensity viewing in the zenith when N₂⁺ 1N (0, 0)=50 kR; only approximately represents sidelooking column radiance.

*** Quenched at altitudes below ~120 km, therefore contributes relatively less to photometer signal.

⁺ Complex (and diffuse), heads extend ~40 Å to blue from first head listed.

⁺⁺ Laboratory value from Ref 18, see text. The high values for the (3, 1) and (2, 0) transitions in Ref 15 may include the (4, 2), (5, 3), (6, 4), and (7, 5) transitions incompletely resolved in the auroral spectra.

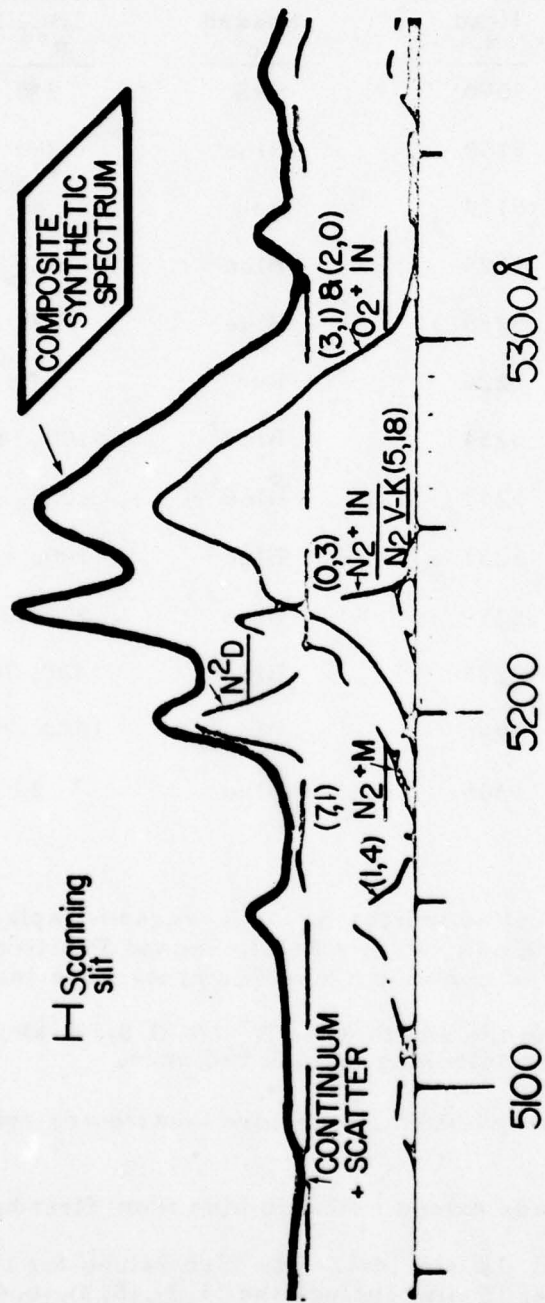


Figure 28. Synthetic auroral spectrum 5100-5300 Å, from Ref 15. In the O_2 First Negative system only the (3, 1) and (2, 0) bands are considered, the (2, 9) band of N_2 Second Positive is neglected, and a strong continuum present in the Ref 15 spectrum data is included. The effective transmission of the scanning slit is actually a triangle of 7 Å FWHM convolved with an 8 Å rectangular function.

been increased by convolution with the scanning slit). The laboratory data on O_2 bombarded by kilovolt electrons (Ref 18), on the other hand, show more $O_2^+ \Delta v = 2$ band emission toward shorter wavelengths, which would result in a greater contribution of this sequence to the photocurrents.

PROCEDURE FOR EVALUATION OF FLIGHT DATA

The relationship of the readings from the two channels to instantaneous auroral column intensity measured by a boresighted 3914 \AA - photometer is indicated qualitatively in the upleg azimuth-elevation scans in Fig's 29a and b. An isolated, narrow arc with peak 5577 \AA radiance $\sim 175 \text{ kR}$ as viewed from PKR is $\sim 50 \text{ km N}$ of the rocket during this data period; refer to Ref 3's All-Sky images (Fig 55) and plot of trajectory and latitudinal extent of the arc (Fig 32). The ordinate scale in the near-meridian altitude profiles (Fig 30) is the rocket's altitude, which is about 11 km below the intercept of its photometers' fields of view on the isolated arc form. The elevation-azimuth scan when the rocket is at 85 km (Fig 29a) includes the airglow chemiluminescence (with a van Rhijn factor that varies between 4 and 10), little of which is expected to be present in the scan from 100 km altitude. Fig's 29 and 30 show that the wider-band channel's signals correlate more closely with the fluorescence directly excited by the aurora-producing particles, as would be expected from their lower content of N^2D-^4S radiation.

We selected for this assessment four representative viewing geometries, pointing toward and away from the arc - geomagnetic N and S - from rocket altitudes above and below the main airglow-chemiluminescence layer - 85 km and 100 km . The radiance data points, which are averages over $\sim 10^\circ$ in azimuth averaged from two successive spin cycles, are listed in Table 2. No correction for the "background" levels has been attempted, as these should in principle drop out of the subtracted data, and in any case the baseline radiances

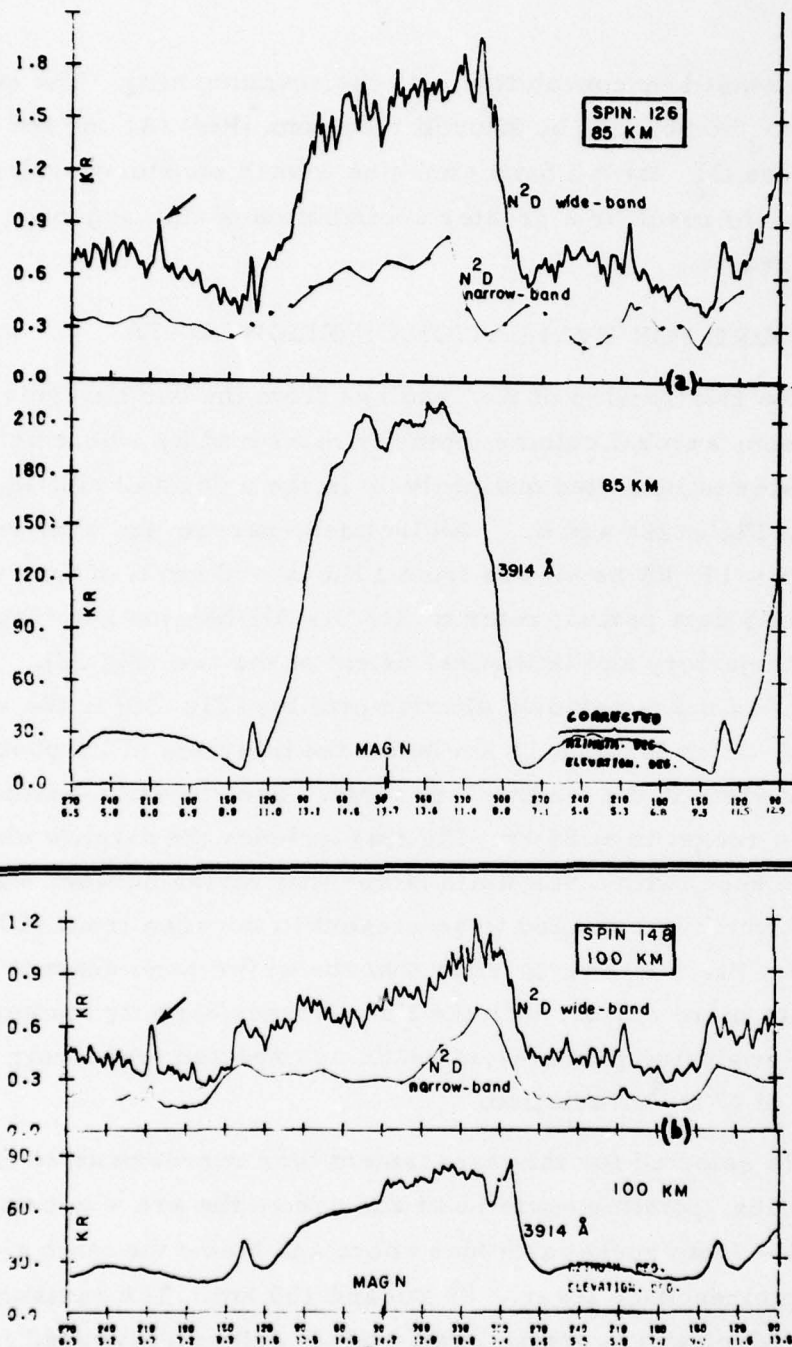


Figure 29. Representative 3914 Å and differential photometer elevation-azimuth scans, A18.219-1 upleg. The data from the narrow-band channel have been manually smoothed in transferring them to these plots. The arrow points to the feature identified in Section I as due to the star Sirius in the instrument's field of view.

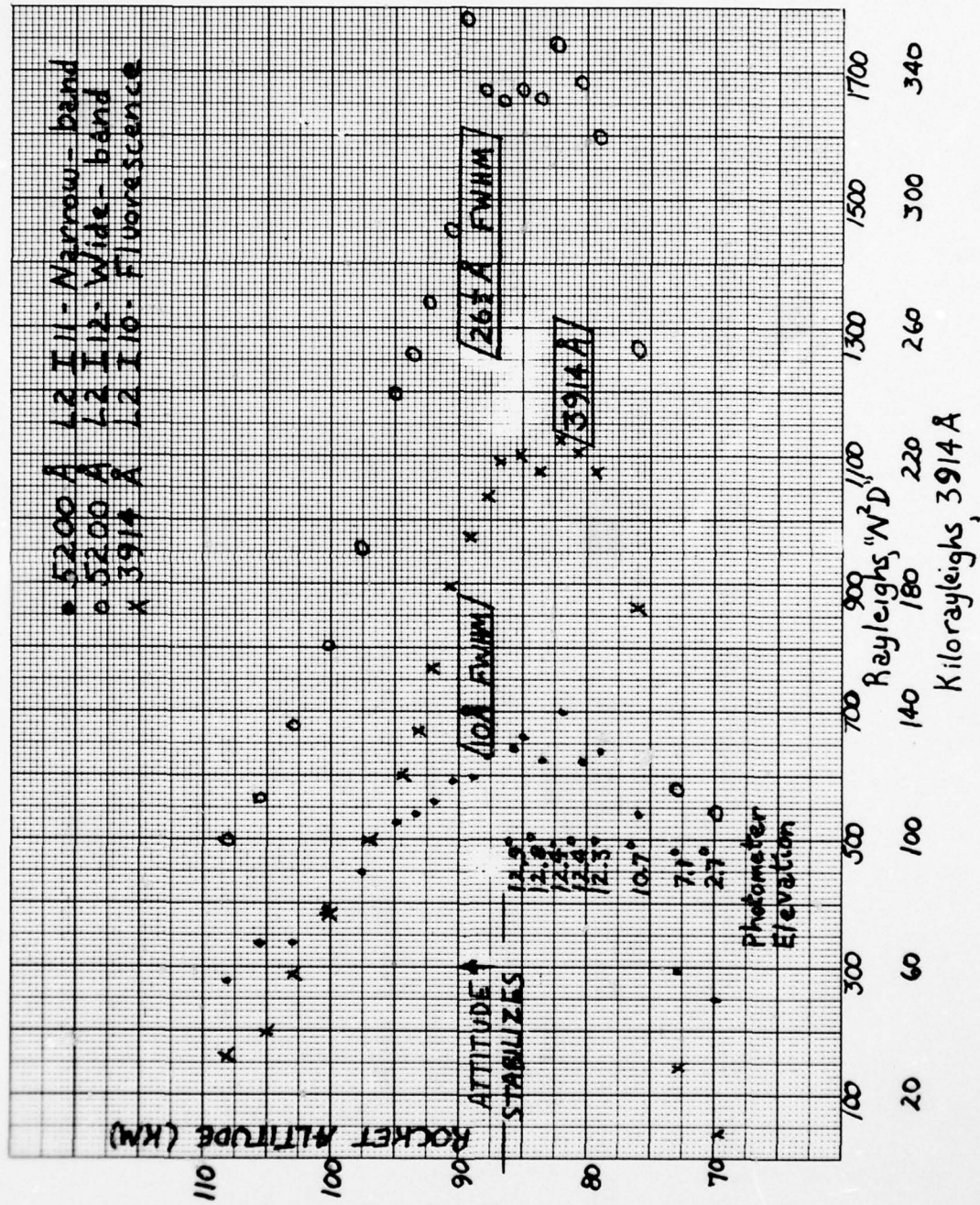


Figure 30. Altitude profiles of air fluorescence and signal levels of the two channels of the N²D differential photometer at 330° magnetic azimuth, A18.219-1 upleg.

Table 2. Differential Photometer and Air Fluorescence Data for Table 3.

Item	Rocket Altitude, Photometer Pointing	N^2D Wide(w), N^2D Narrow(n), 3914 \AA , kR	
		R	R
1	85 km, 360° Az, 11° El	1490	590
2	(Spins 125-7) 180° Az, 9° El	685	270
3	100 km, 360° Az, $11\frac{1}{2}^\circ$ El	685	325
4	(Spins 148-9) 180° Az, 9° El	330	200

are expected to be a real physical effect of buildup of $[N^2D]$ in the auroral ionosphere (Ref 13). We make the assumption that each channel's calibration in terms of N^2D-^4S radiant intensity, in which units the data have been presented by the photometer group, refers to its response to a doublet (only) whose lines have the 1.53:1 ratio and location on the sensitivity band shown in Fig 27. (The aforementioned shift in effective filter transmission, while introducing quantitatively substantial changes in the narrow channel's signal levels, was found in auxiliary calculations not to change qualitatively the conclusions of this evaluation.)

The radiation flux reaching each photocathode may thus be related to its datum point by the equation

$$\begin{aligned} & (\text{Transmission to } N^2D-^4S) \times (\text{Actual } N^2D-^4S \text{ radiant intensity}) + \\ & \Sigma (\text{Transmission to background feature}) \times (\text{Radiant intensity of} \\ & \qquad \qquad \qquad \text{background feature}) \\ & = (\text{Transmission to } N^2D-^4S) \times (\text{Radiant intensity datum}). \end{aligned}$$

The background flux is the sum of products of spectral intensity of fluorescence bands (and continuum) and filter transmission. Applying the filter curves in Fig 27, we find that the weighted transmissions to the doublet are 0.39 and 0.75, and the area integrals (transmission summed over wavelength) are 4.8 Å and 20.3 Å, respectively for the narrow-band and wider-band channels of the differential photometer.

The two auroral " N^2D " data points in a row of Table 2 in two linear equations of the above form allow for solution for the N^2D-^4S radiant intensity and the intensity of one background contaminant feature. Intensities of other auroral features can be ratioed to this latter number (we shall provide examples presently). Successful application of this concept requires, of course, that the folding of background spectral intensity into the response characteristics has been performed correctly, and that off-band-off-axis leakage is either negligible or relatable to the area integrals for all scene brightness distributions.

EVALUATION FOR SYNTHETIC-SPECTRUM MODELS

The first-approximation fit to the data (Calculation A) assumes that the wavelength-averaged background intensity is the same in the sensitivity bands of both channels. This is the reduction procedure usually applied to data from co-located wide- and narrow-band filter photometer pairs, particularly when little a priori information is available about the spectrum of the background radiation. The spectral radiance need not be uniform, or even have constant slope across the passbands; it need only have a shape that contributes photocurrents proportional to the area integrals of the filters.

A spectrum dominated by N_2^+ First Negative (0, 3) band radiation and airglow continuum (refer to Fig's 27 and 28) might appear to meet this condition reasonably well. The two simultaneous equations then become

$$\begin{aligned}0.39 N^2D + 4.8r &= 0.39n \\0.75 N^2D + 20.3r &= 0.75w,\end{aligned}$$

where n and w refer to the input data in Table 2, r is the mean background spectral intensity extending across both sensitivity bands (units are Rayleighs/Å), and N^2D the corrected radiant intensity of the doublet. Solutions of these equations, listed in the second and third columns of Table 3, are clearly inconsistent, as they result in physically-unrealizable negative N^2D - $4S$ intensities (and excessively high mean backgrounds 5185-5215 Å). Thus this zeroth-order calculation fails to subtract out the fluorescent-chemiluminescent auroral background contaminating the signal from metastable N^2D atom radiation.

The next logical step is to improve the background model by putting in the response of each channel to the expected spectrum of radiation from charged particle-excited air. As a second approximation, we add in the contribution of the (0, 3) band of the N_2^+ First Negative system and calculate the further quasi-continuum background radiance that (we assume) contributes photocurrents proportional to the area

Table 3. Calculated N_2^+D and Background Intensities from Four Synthetic-Spectra Models

Table Data	Background A, $\frac{R}{A}$	N_2^+D A, $\frac{R}{R}$	Background B, $\frac{R}{A^{**}}$	N_2^+D B, $\frac{R}{R}$	$N_2^+(0,3)C$, $\frac{R}{kR^+}$	$\frac{N_2^+(0,3)}{N_2^+(0,0)}$	N_2^+D C, $\frac{R}{R}$	$N_2^+(0,3)D$, $\frac{R}{kR^{++}}$	$\frac{N_2^+(0,3)}{N_2^+(0,0)}$	N_2^+D D, $\frac{R}{R}$	N_2^+D E, $\frac{R}{R}$
1	$81\frac{1}{2}$	-410	20	+40	3.3	1/59	+89	1.9	1/101	+247	+154
2	$37\frac{1}{2}$	-190	22	-47	1.00	1/29	-3	0.58	1/49	+44	+97
3	$32\frac{1}{2}$	-74	12	-129	2.14	1/32	+83	1.25	1/54	+184	+220
4	12	+52	3.8	-28	0.58	1/41	+134	0.34	1/71	-162	+162

^{*} Mean auroral background r over filter bands, as defined in text for Calculation A.

^{**} Mean auroral background r over filter bands, as defined in text for Calculation B

[†] Intensity of N_2^+ First Negative (0, 3) band, from Calculation C.

^{**†} Intensity of N_2^+ First Negative (0, 3) band, from Calculation D.

integrals. We took the intensity of the (0, 3) band as 1/72 that of the (0, 2) band, and folded its rotational spectrum from Ref 1 line-by-line into the transmission characteristic of each filter. The two equations for this Calculation B are then

$$0.39 N^2_D + 0.044 N_2^+/72 + 4.8r = 0.39n$$

$$0.75 N^2_D + 0.253 N_2^+/72 + 20.3r = 0.75w,$$

where N_2^+ is the measured (0, 0) band intensity, listed in Table 2. (Shifting the filter bandpasses 1 Å to shorter wavelengths gives effective (0, 3)-band transmissions of 0.038 and 0.23 respectively, as compared to 0.044 and 0.253 without such a shift.) This approach to a model spectrum also failed to produce realistic doublet intensities, as the solutions listed in Table 3 show.

Results of three further attempts to fit the differential photometer data are also shown in Table 3. The background spectrum for Calculation C was taken as a continuum having zenith intensity $2R/\text{Å}$ at 85 km and $0 R/\text{Å}$ at 100 km, plus the N_2^+ First Negative (0, 3) band whose intensity is one of the unknowns. The ratio of the inferred (0, 3) band intensity to the measured (0, 0) is the principal test of performance of this fitting procedure. Calculation D is a refinement of C, with the contribution of the $\Delta v = 2$ sequence of the O_2^+ First Negative system added as a fixed fraction of that from the N_2^+ (0, 3) band. Following Ref 15, we took the intensity of the sequence as 4x that of the latter band, and estimated that the wider filter and narrow filter transmit respectively 3% and 0% of its spectrum; refer to the synthetic spectrum in Fig 28. The simultaneous equations for Calculation D are

$$0.39 N^2_D + 0.044 N_2^{+'} + 2v \ 4.8 = 0.39n$$

$$0.75 N^2_D + 0.373 N_2^{+'} + 2v \ 20.3 = 0.75w$$

where $N_2^{+'}$ is the (0, 3) band's intensity (one of the unknowns) and v an effective van Rhijn factor viewing through the airglow layer ($v =$

$5\frac{1}{4}$ - $6\frac{1}{2}$ for the 85 km data, and is taken as zero at 100 km rocket altitude). For Calculation C, the equations are the same except that 0.373 (=0.253 + 4 x 0.03) is replaced by the wider-band channel's relative sensitivity to the (0, 3) band only, 0.253.

Calculation C results in too much N_2^+ (0, 3) band radiation and N^2D radiance levels comparable, with one exception, to those typically measured in aurora (see the arc measurements in Section V of Ref 1, and Ref 13). Calculation D results in better fits to the expected (0, 3):(0, 0) band ratio 1:72, but with excessive levels of doublet intensity.

Calculation E uses only the data from the narrow-band channel, correcting them for the contribution from the N_2^+ (0, 3) band whose intensity is ratioed from the measured (0, 0) band plus $2 R/\lambda$ of continuum (at 85 km rocket altitude only):

$$0.39 N^2D + 0.044 N_2^+ / 72 + 2v 4.8 = 0.39n.$$

The results (last column of Table 3), though also indicating somewhat too high doublet intensities, do show the expected higher N^2D concentrations in the arc. Intensities decrease with photometer intercept altitude in the arc and increase with altitude in the south. Note that even when the continuum is omitted - for the data at 100 km - the N^2D radiances for the conditions of Calculation E remain high.

CONCLUSIONS

These reductions of the data from the sidelooking differential photometer on A18.219-1, which apply various plausible model spectral distributions for the auroral background, have failed to provide credible values for the intensities of radiation in the N^2D - 4S doublet toward and away from an auroral arc.

The very poor results with Calculation A are most likely due to its inappropriately simple background spectrum. The inconsistencies from Calculations B-E - too much N_2^+ -band and/or N^2D - 4S intensity - appear to stem from the excessively high signals in the narrow-wave-

length band channel. These photocurrents may result from inadequate baffling of the photometer's optical system against radiation from off-axis angles, as discussed earlier.

Since the spectral intensity of particle-excited air at auroral altitudes is both uncertain and decreasing sharply with decreasing wavelength near 5200 \AA , the background is better referenced with narrow sensitivity-band channels than with a single broad channel. A second $\sim 7\frac{1}{2} \text{ \AA}$ photometer centered at 5205 \AA would most likely provide adequately quantitative $\text{N}^2\text{D}-^4\text{S}$ radiance data, for example (refer to the discussion on p 128 of Ref 1). In contrast to the zenith view from aircraft (Section VI), the near-sidelooking view from sounding rockets results in a high contribution from the airglow continuum; - a layer with zenith spectral radiance $2 \text{ R}/\text{\AA}$ viewed with the typical van Rhijn path-length enhancement of 5 would produce $2 \times 5 \times 8 \text{ \AA} \approx 80 \text{ R}$ of spurious signal, which is comparable to the expected radiance levels in the doublet. Therefore even if the air fluorescence in molecular bands can be compensated by an improved synthetic spectrum and monitoring of the N_2^+ First Negative system's intensity, a reference photometer is needed in coordinated experiments from multi-instrumented rockets to measure accurately the column-concentrations of N^2D precursor atoms.

SECTION V

HIRIS VIEWING GEOMETRY

AURORAL CONDITIONS, POINTING REQUIREMENT

A Sergeant rocket carrying the helium cooled high resolution (2 cm^{-1}) interferometric spectrometer payload HIRIS II (IC630.02-1A) was launched at 0805:20 UT 01Apr76 from Poker Research Range, AK to measure 4-22 μm infrared emissions resulting from excitation of the upper atmosphere by energetic charged particles (Ref 19). Ground based observations (Ref's 19, 20) showed that there had been substantial predosing, a Class III+ breakup just before launch, and a weakening and southward movement of the visible aurora starting about one minute after launch. Large spatial/temporal variations in bombardment intensity were observed near the trajectory, with the rocket penetrating Class II diffuse regions on both upleg and downleg.

All-sky views of the spatial distribution of excitation as viewed from Poker Flat and Fort Yukon, along with projections ($e\ell$ and az from these stations) of both the rocket and intercept of the magnetic field line through it with a plane at 100 km altitude, are in Fig 58 of Ref 3. Ref 20 contains further all-sky images, meridian photometer scans (records from both stations in four emission features are available), and other geophysical data characterizing the auroral ionosphere and lower atmosphere before and during flight. Ref 21 gives in addition electron density contours, energy spectra of the precipitating particles, and other ionosphere parameters derivable from incoherent-backscatter data taken by the DNA 617 (Chatanika) radar.

Vertical attitude stabilization was not achieved due to a malfunction of the rocket's control system that caused its long axis to pitch at $10\frac{1}{2}$ degrees/sec. Thus the spectrometer scanned periodically across the earth's limb and surface as well as through auroral particle-

excited air. This section outlines the procedure for establishing pointing of the tumbling instrument's field of view (taken from the aspect and trajectory data, Ref 22) against the dynamically-changing, three-dimensional aurora (whose surface radiance distribution is determined from meridian scanning photometer and all sky camera data records).

ROCKET POINTING GEOMETRY

A projection into the meridian plane of the rocket's trajectory, whose plane lay 8° E of geomagnetic N, is in Fig 31. During the time that the instrument door was open (88 km on upleg to 62 km on downleg) the rocket rotated six times about a horizontal axis, with a period of closely $34\frac{1}{2}$ sec. The period about a vertical axis was about $\frac{1}{2}$ sec longer, which results in a slow N \rightarrow E directed (clockwise as viewed from above the rocket) precession of the azimuth angle at which the spectrometer's optic axis reaches each elevation angle. Specifically, the rate of precession around the vertical direction averages $\sim +0.0139$ sec, or 360° in $7\frac{1}{2}$ hr, so that this azimuth angle increases by $\sim 0.46^\circ$ per rotation of the rocket about a horizontal axis ($\pm 0.25^\circ$ in the six rotations, as indicated by the entries in the last column of Table 4).

The inset in Fig 31 illustrates the spectrometer's elevation and azimuth pointing angles in 1 km altitude intervals for the first such (complete) rotation in the data period (altitudes 96 to 116 km). Fig 32 is a parallel, vertical projection of the rocket's long axis onto a horizontal plane for this rotation, without considering its 14 km northward movement or 20 km rise. The lengths of the lines in Fig 32 are proportional to the apparent length of the rocket to an overhead observer traveling parallel to the rocket's ballistic trajectory at a distance large compared to the rocket's full length. In the rocket's translational frame of reference, its nose - that is, the spectrometer - is describing a cone of full angle $\sim 165^\circ$ whose axis points at an average elevation of $+ \sim 9^\circ$ and azimuth $\sim 130^\circ$ during the six rotation

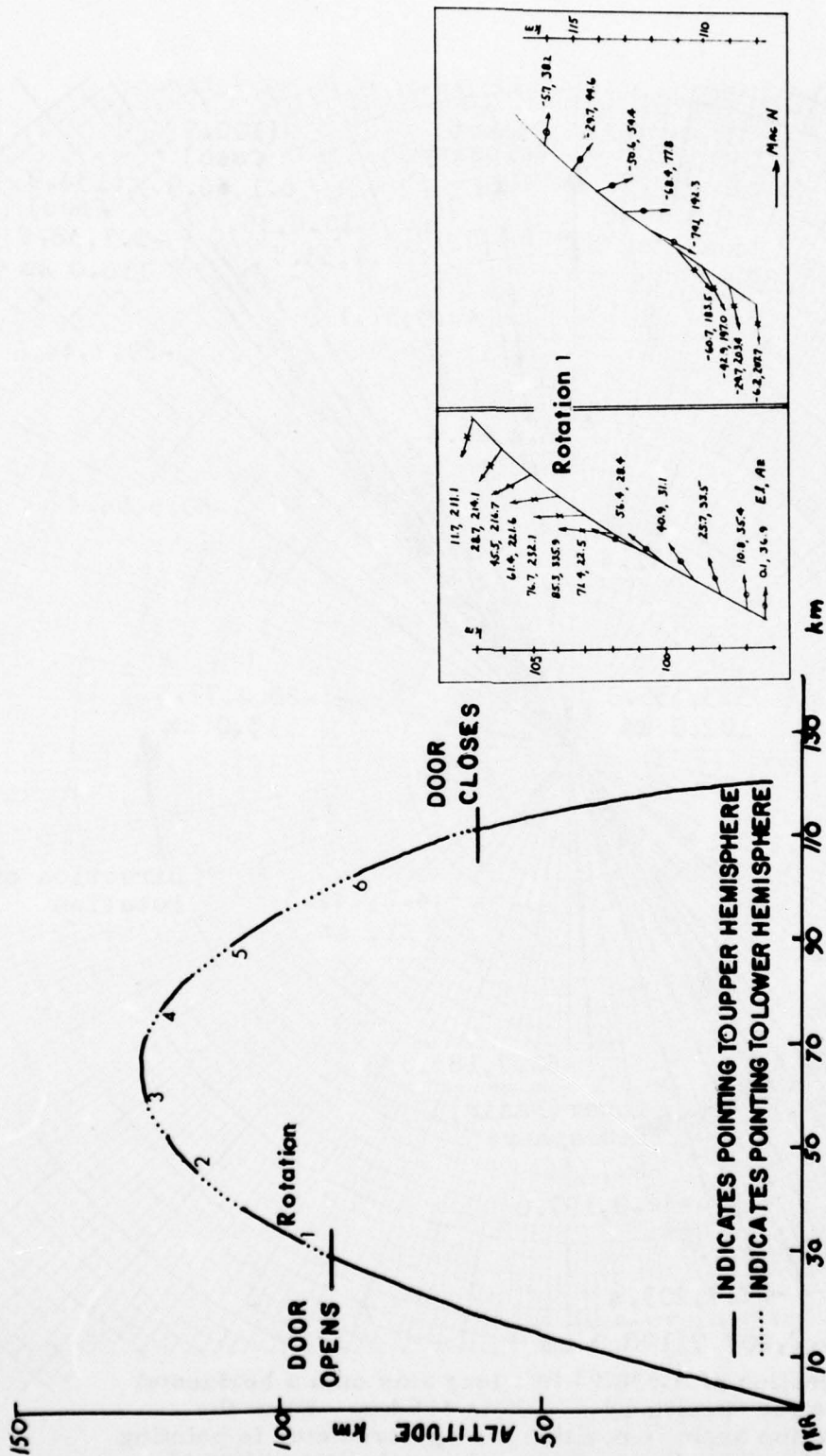


Figure 31. Trajectory of HIRIS II (IC630.02-1A) projected into the meridian plane through PKR, with the altitude ranges over which the axially mounted interferometric spectrometer points into the upper and lower hemispheres. The insets show the elevation and geomagnetic azimuth angles of the rocket's long axis in 1.0-km altitude intervals during the first complete rotation of the rocket about a horizontal axis after the instrument begins to take data. o's and x's indicate E and W pointing components, out of and into the plane of the page respectively.

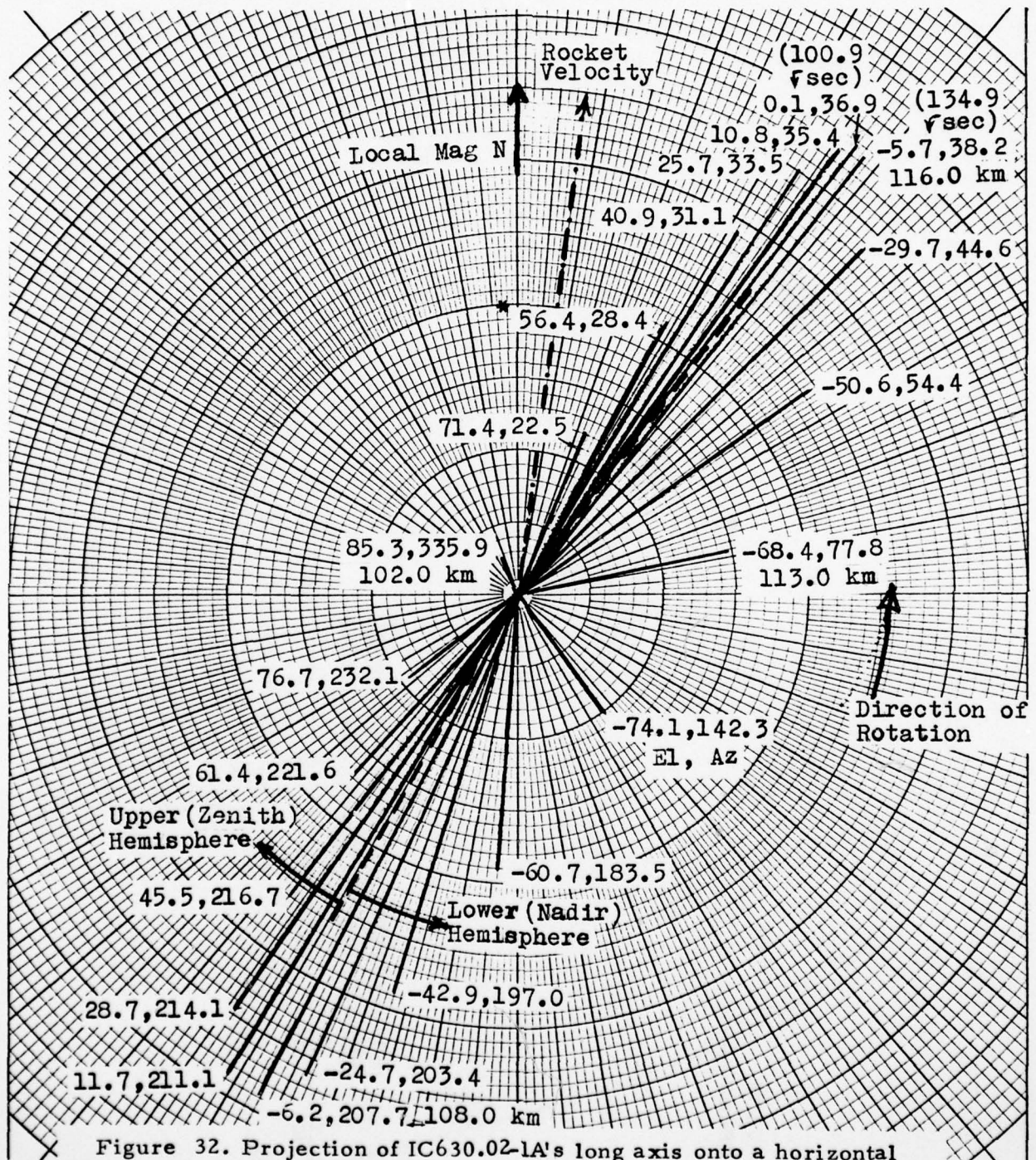


Figure 32. Projection of IC630.02-1A's long axis onto a horizontal plane for Rotation 1, 96 to 116 km. When the elevation angle is positive the spectrometer is pointing into the upper hemisphere. The rocket's position at 106 sec (*) keys to Fig 34.

THIS PAGE IS BEST QUALITY PRACTICABLE
FROM COPY FURNISHED TO DDC

Table 4. Times/Altitudes of Zero, Maximum, and Minimum
Elevation Pointing Angle of IC630.02-1A

Rotation	Time (sec after launch)	Rocket Altitude (km)	Instrument Elevation (degrees)	Instrument Azimuth (geomagnetic)
1	100.9	96.3	0.0	36.9
	109.3	102.2	86.2	304.0
	118.2	107.7	0.0	209.1
	126.6	112.2	-74.9	129.6
2	135.5	116.2	0.0	37.1
	143.7	119.3	85.3	301.0
	152.6	121.9	0.0	210.4
	161.1	123.7	-75.0	125.5
3	170.0	124.9	0.0	37.8
	177.9	125.3	84.0	320.4
	187.1	125.0	0.0	211.0
	195.3	124.1	-77.5	129.5
4	204.5	122.4	0.0	38.3
	212.4	120.2	84.4	308.3
	221.7	116.9	0.0	213.5
	229.6	113.5	-77.5	130.2
5	239.1	108.6	0.0	38.7
	246.9	103.9	83.0	302.8
	256.1	97.6	0.0	214.8
	264.2	91.4	-77.1	123.1
6	273.3	83.7	0.0	39.2
	280.4	77.2	85.0	308.4
	289.6	67.9	0.0	222.3

cycles. To an observer looking W, as for Fig 31, the rocket appears to be rotating counterclockwise. The "plane" of this rotation - actually the pointing is $\pm 8^\circ$ out of plane - is "crabbing," lying some 30° from the 8° -E plane of the trajectory (refer to Fig 32).

The spectrometer completes one spectral scan (compiles a double-sided interferogram) in 1.36 sec. Thus over each $34\frac{1}{2}$ sec rocket rotation it obtains approximately 12 spectra in both the upper and lower hemispheres plus 2 spectra while crossing the earth's limb. Altitudes and times when the indicated maximum, minimum, and zero elevation angles are reached in the six rotations are in Table 4. Near zero elevation angle, when the instrument is viewing aurorally excited air side-on from co-altitude - that is, when the van Rhijn gain is high - its angular sweep rates are $+ 10.75^\circ$ el/sec and $- 2.1^\circ$ az/sec (upswing), and $- 10.37^\circ$ el/sec and $- 1.9^\circ$ az/sec (downswing). Fig 33 is a detailed altitude profile of the HIRIS spectrometer axis' elevation and azimuth pointing over the data-taking period.

As an example (from Rotation 1), when the rocket was at 96.3 km the instrument's elevation angle is 0° at azimuth 37° (E of local magnetic N). At 102.2 km the rocket's axis was nearly vertical (at 3.8° zenith angle), so that the recorded spectrum represents in effect integrated column emissions overhead from that altitude. Earth limb and van Rhijn effect-enhanced data are again obtained from near 107.7 km (118.2 sec), at azimuths centered at 209° . Minimum elevation ($- 74.9^\circ$) is reached at 112.2 km 8.4 sec later, at $129\frac{1}{2}^\circ$ az. The azimuths at which the elevation is 0° increase slowly, as noted previously, in each rotation; the spectrometer points northeast on the upswing, and southwest - back, toward the intense aurora to the S - on downswing.

AURORAL-EXCITATION INTERCEPTS

Meridian photometer scans output quantitative records of visible-auroral emission rates summed over columns extending from the ground

AD-A055 884

PHOTOMETRICS INC LEXINGTON MASS
ASSESSMENT AND EVALUATION OF SIMULATION DATA.(U)
NOV 77 I L KOFSKY, D P VILLANUCCI, G DAVIDSON

F/G 4/1

UNCLASSIFIED

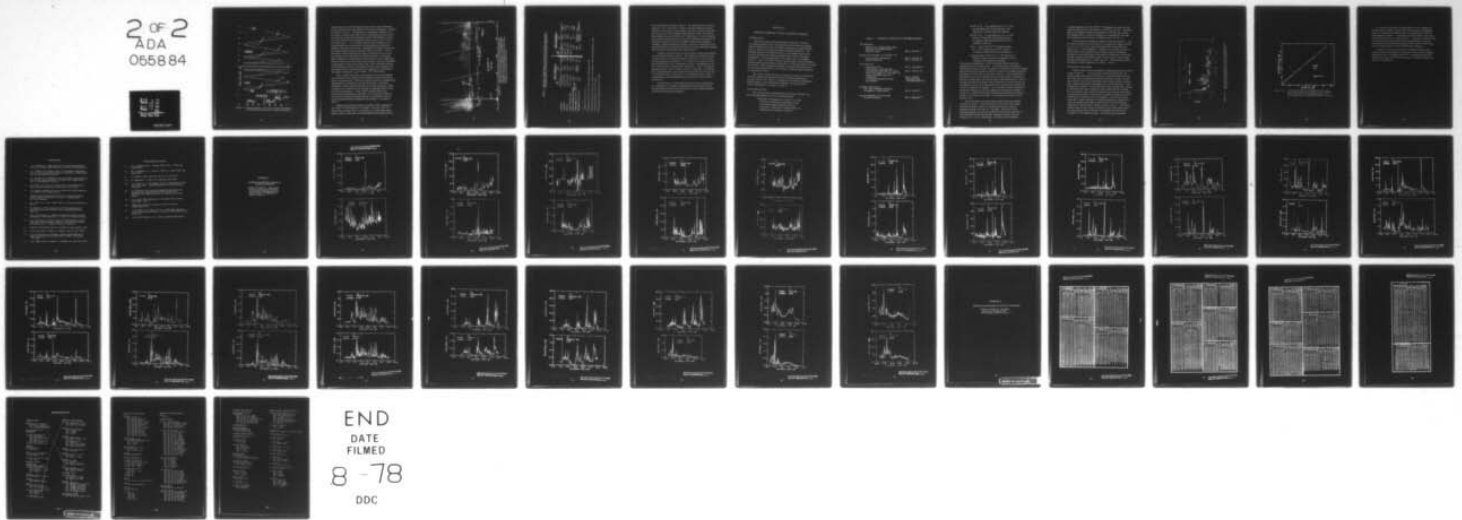
PHM-01-78

DNA-4303F

DNA001-77-C-0208

NL

2 OF 2
ADA
0658 84



END
DATE
FILMED
8-78
DDC

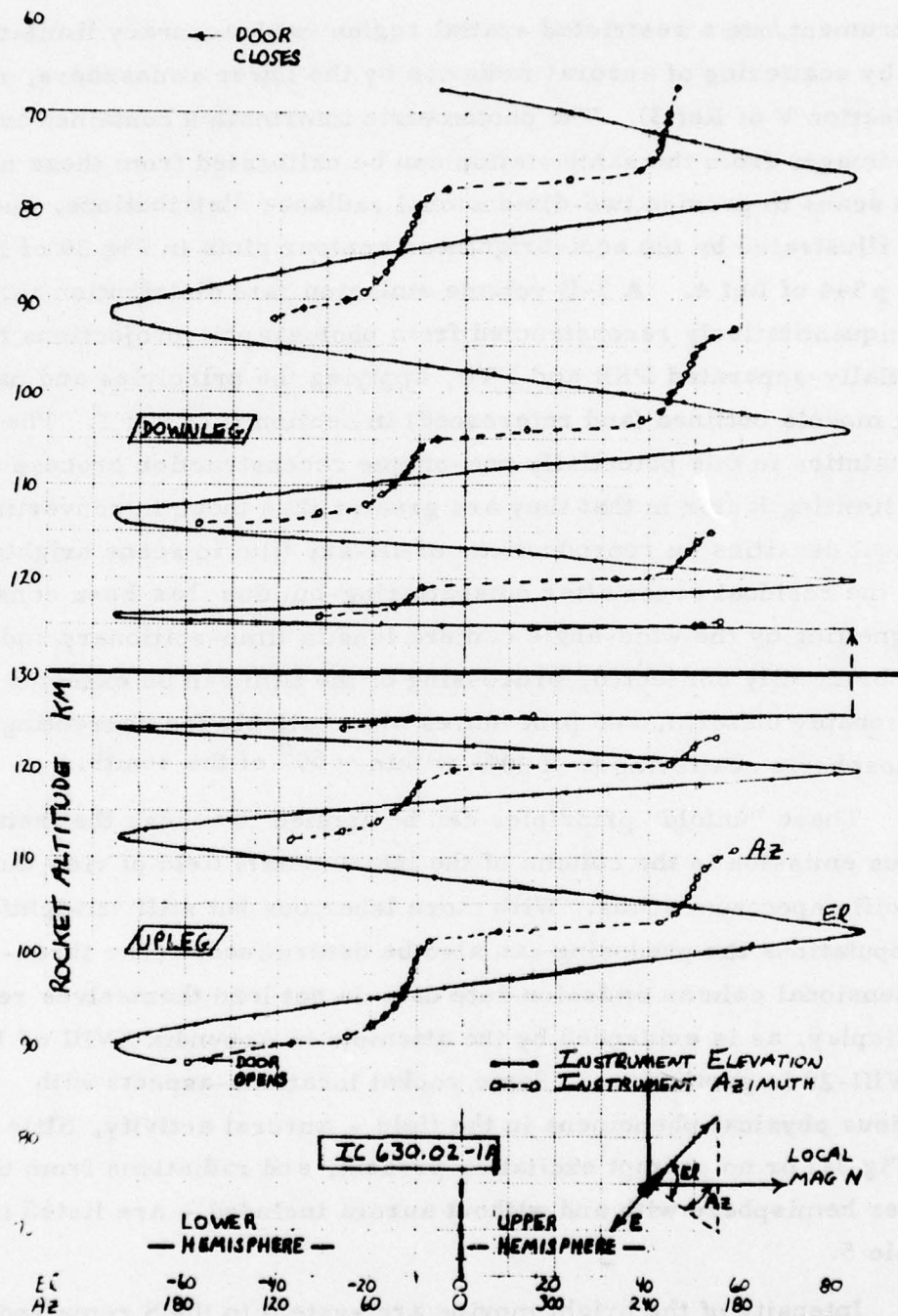
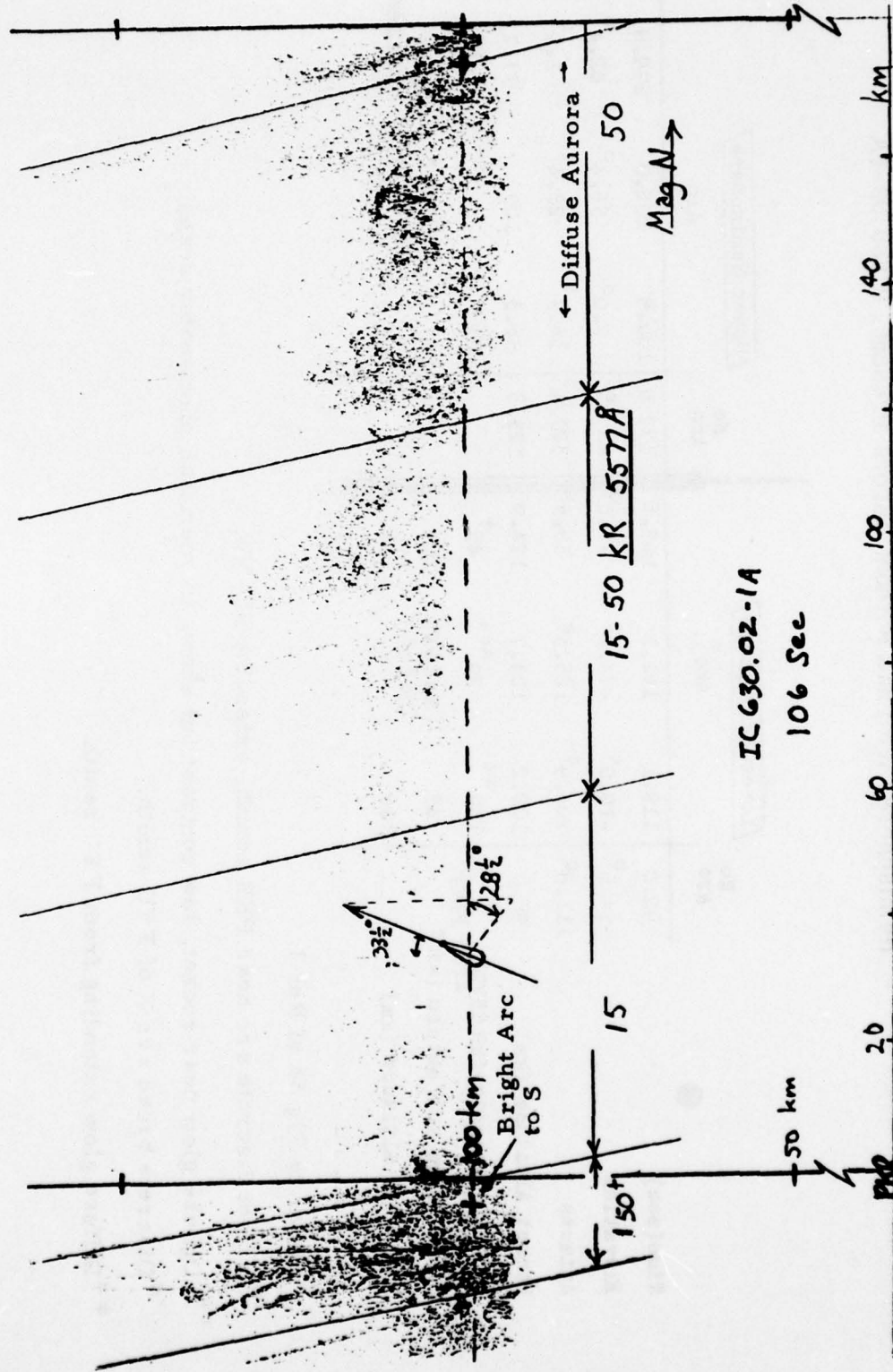


Figure 33. Altitude profiles of elevation and azimuth angles of IC630.02-1A's spectrometer on upleg and downleg.

instrument into a restricted spatial region (with accuracy limitations set by scattering of auroral radiation by the lower atmosphere, reviewed in Section V of Ref 3). The photometric information contained in all-sky images from the same station can be calibrated from these narrow line scans to provide two-dimensional radiance distributions, such as are illustrated by the equi-brightness contour plots in Fig 30 of Ref 1 and p 344 of Ref 4. A 3-D volume emission rate distribution can be semiquantitatively reconstructed from photographic projections to spatially-separated PKR and FYU, applying the principles and particle-flux models outlined (and referenced) in Section II of Ref 1. The uncertainties in this potentially non-unique reconstruction process are the limiting factor, in that they are greater than those in converting optical densities on reproductions of all-sky film to scene brightnesses and the residual error after outscattering-buildup has been considered. (Vignetting by the wide-angle camera lens is time-stationary and thus can be readily corrected, processing of the film can be expected to be reasonably uniform, and procedures are available for correcting for atmospheric scattering to $\leq 30\%$ within $\sim 60^\circ$ of the zenith.)

These "unfold" principles can be applied to assess the instantaneous emission in the column of the instrument's field of view during specific spectrum scans. With more laborious but still straightforward computations the predosing can also be determined. (The three-dimensional column emission rate data do not lend themselves readily to display, as is evidenced by the attempts in Appendix XVIII of Ref 1, p XVIII-28 in particular.) Some rocket locations-aspects with various physical phenomena in the field - auroral activity, little (as in Fig 34) or no prompt excitation present, and radiations from the lower hemisphere with and without aurora included - are listed in Table 5.

Intensity of the bright moving arc system to the S remained at 100-150 kR 5577Å during most of the flight. When the rocket was near 108 km on upleg (119 sec, in Rotation 1), the west limb of this region, narrow at that time, passed through the instrument's field of



IC 630.02-1A
 106 Sec

Figure 34. Spectrometer pointing into the upper hemisphere at 106.0 sec (100.0 km, Rotation 1), with approximate intensities in the meridian plane from PKR of the bright arc to the S and diffuse aurora to the N (refer to column 7 of Table 5), IC630.02-1A.

Table 5. Examples of Spectrometer Pointing Into the Upper and Lower Hemispheres With and Without Aurora Present, IC630.02-1A

	Lower Hemisphere		Upper Hemisphere	
	No Arc	Arc *	No Arc	Arc
Time (sec)	92.8	119.1	169.6	177.9
Elevation	-74.5°	-10.9°	-5.0°	84.0°
Azimuth	111.8°	206.9°	38.5°	320.4°
Rocket Altitude (km)	90.0	108.2	123.7	124.9
Auroral Intensity (kR 5577Å from PKR)	150 **	20 ***	45 †	125.3
Slant Range to Feature (km)	45	(aurora below)	100	60 †
Intercept Altitude (km)	100	116	100	96.3
				100 (rocket "inside" aurora)
				15 ***
				20 ††
				77.7
				279.8
				82.4°
				1.2°

* Refer to Fig 58 of Ref 3.

** Bright discrete arc near PKR zenith, extending SE-NW.

*** Diffuse glow near rocket, low contrast but shows in meridian photometer scans.

† Discrete broad arc N of FYU zenith.

†† Diffuse glow extending from FYU zenith.

view (second entry column in Table 5). The spectrometer's elevation angle was -11° , az was 207° , so that it was intercepting the excited volume ~ 45 km S near 100 km altitude. Earlier in the spin cycle when the rocket was at 100 km altitude (seventh entry column, and Fig 34), little excitation lay in the field at $33\frac{1}{2}^{\circ}$ zenith angle. In later rotations, the northward movement of the rocket plus southward movement of the excitation results in much less favorable viewing of this intensely-radiating, broadened region; the relative increase in separation causes the spectrometer to point generally below the energy deposition altitudes when its field is directed into the southern sector.

At higher rocket altitudes the spectrometer viewed mostly diffuse (20-45 kR zenith radiance) aurora. Near apogee for example a broad ~ 20 kR region lay (principally) below the rocket; at 161 sec when the tumbling payload was pointing at -75° el (third entry column) it views this region and the earth's atmosphere-surface. Approximately 9 sec later (fourth column) elevation had increased to -5° at a NE azimuth, placing a distant (~ 100 km range) 45 kR arc in the field. On downleg, the rocket penetrated a region that had been predosed by Class II+ -III (~ 50 -100 kR) aurora in the period ~ 5 -15 minutes previous. When it reached 80 km, the instantaneous auroral intensity in its zenith was about 20 kR.

As noted above, meridian photometer and all-sky camera data are available for assessing semiquantitatively the prompt and past auroral-particle dosing in the spectrometer's field at these and other rocket aspects/trajectory positions.

SECTION VI

AURORAL INTENSITIES, ICECAP 76 AIRCRAFT PROGRAM

INTRODUCTION

AFGL's IR-Optical Flying Laboratory (USAF NKC-135A S/N 55-3120) performed a series of measurements of the short-wavelength infrared emissions from auroral particle-excited air during the period 22 Feb - 28 Mar 1976, under the program heading ICECAP 76. The principal function of the flight missions is to investigate spatial structure of, and processes leading to, radiation near $2.8\mu\text{m}$ by the upper atmosphere. The Operating Plan for the flight series is Appendix I of Ref 3, Table I-1 of which lists the characteristics of the radiometers, interferometric spectrometers, photometers, and all-sky camera carried by the aircraft. Other background material on the eight night flights in the auroral zone and the similar set of missions conducted under ICECAP 75 is referenced in Table 6.

This section reports the auroral radiances measured in the moving aircraft's zenith by five channels of the narrow-filter photometer of aircraft system E-05, which is coaligned with the infrared radiometers. Characteristics of this sequentially-sampling, thermoelectrically-cooled instrument are in Table I-2 of Ref 3.

DATA, APPLICATION

The air fluorescence-chemiluminescence features reported, and their principal functions in the aircraft program, are

$4278 \text{ \AA } N_2^+$ First Negative (0, 1) band ($7.7, 2.4 \text{ \AA}$):
monitor of column rate of production of ions
by incoming charged particles (refer to
discussion of the ratio of column intensity to
ionization rate in Section V of Ref 3);

Table 6. Reports on ICECAP Aircraft Measurements

1975 Missions

- Instruments, flight paths, data periods, coordination with PKR facilities

Ref 2, Section V

Results from Flight 75-4 (10 Mar 75)

- Preliminary assessment
- Final evaluation

Ref 2, Section III
Ref 3, Section IV

1976 Missions

- Operating Plan
- Instruments, data periods, coordination with DNA 617 radar
- Data from Flight 76-9 (07 Mar 76), 2.8 μ m synthetic spectra & passbands
- 12-channel photometer data, flight paths

Ref 3, Appendix I

Ref 3, Section VI

Ref 4, p 207 ff
THIS SECTION
+ APPENDIXES I&II

**Synthetic Spectra for
NO + OH + thermal radiation,
atmosphere transmission**

Ref 2, Section I

**Optical Method for determining
auroral altitudes**

Ref 3, Appendix II

5577 Å OI $^1S_0 - ^1D_2$ forbidden line (7.9, 3.4 Å):
second indicator of auroral intensity, with
application to energy deposition altitudes;

6300 Å OI $^1D_2 - ^3P_2$ forbidden line (9.2, 5.5 Å):
indicator, when taken with N_2^+ fluorescence,
of altitude of peak energy deposition (refer to
Appendix II of Ref 3);

5198.7 - 5200.5 Å NI $^2D - ^4S$ forbidden doublet
(8.5, 4.5 Å): precursor of NO^+ , measure
of buildup of [NO] in the auroral ionosphere;

Continuum near 5312 Å (10.0, 7.1 Å): measure of
buildup of [NO] in the auroral ionosphere, and of
continuum sky brightness at twilight.

The numbers in parentheses are the full-widths-to-half-maximum-response and area integrals of the individual channel. The absolute calibration procedure includes convolution of the emission feature's spectral shape with that of the sensitivity band as corrected for radiation filling the photometer's 2° full field of view; refer to Ref 23. Some contribution to the signals in the last two channels from air fluorescence is expected on the basis of experience from auroral flights of this photometer in 1968-72. The data from the N_2^2D channel, whose sensitivity is shown in Fig 27, are reasonably accurate, as evidenced by the fact that they follow closely the OI red line radiances as expected. The correction for the contribution of the N_2^+ First Negative (0, 3) band, applying the procedure described in Section IV, is $3R/kR$ 4278 Å band (viewing in the zenith the continuum of Fig 28, if it is indeed a real effect, is not expected to introduce much further error).

The photometer's 12-position filter wheel makes one complete revolution in 24 sec. During this time the aircraft's forward speed advances the fields-of-view, as projected on the typical energy deposition altitude of 100 km, by $\sim 1\frac{1}{2}$ fields. Data from the two additional channels that monitor N_2^+ fluorescence and one sensitive to the 6300 Å line would lower the time resolution for these emission features to 8 or 12 sec respectively. Records are also available

of zenith intensity of the $3466 \text{ \AA} \text{ N}^2\text{P} - ^4\text{S}$ forbidden line, and from the relatively fluorescence-free channel at 5525 \AA (9.0, 4.6 \AA). The latter data can be applied to extend measurement of 5577 \AA aurora-airglow into twilight, and/or measure brightness of the twilight sky (for other than ICECAP auroral missions, as listed in Table 6 of Ref 3).

The forty plots of zenith-sky radiance in the above features - five for each of the seven cross-auroral arc or parallel-arc flights ICECAP 76-3, 4, 5, 6, 9, 10, and 16, plus the Eielson AFB \rightarrow Pease AFB ferry flight 76-17, - are in Appendix I. Appendix II is a listing for each of the seventeen 1976 missions of the aircraft's position and heading, altitude, air and ground speed, and outside air temperature, along with the sun's azimuth and elevation angles from the earth's surface below its flight path (prepared by J. Reed, Ref 24). Data periods and other particulars of these missions are in Table 6 of Ref 3.

REDUCTION PROCEDURE

Typical output from the sequentially-sampling photometer is shown in Fig 76 of Ref 3. To access these interlaced channel data, the signal voltages above dark-current level are manually measured from the strip charts and entered by teletype into AFGL's central computer. Also entered is the control information flight number and date, mission type, channel (identified by wavelength) and its calibration factor, and amplifier gain setting. The program that creates the data file is written so that only those values of gain and output voltage that have changed from the previous entry need be entered for each successive data point. An existing PhotoMetrics program then computes and plots the auroral brightnesses in formats such as in Appendix I. The abscissa (time) scale can be readily adjusted for convenient qualitative comparison to similarly-plotted zenith radiance data from the aircraft's infrared radiometers (whose format is shown in Ref's 2 and 4). The visible radiance data are also stored on punched cards to allow ready access for reprinting or further reduction, for example correction of the continuum or N^2D channels for their air fluorescence components.

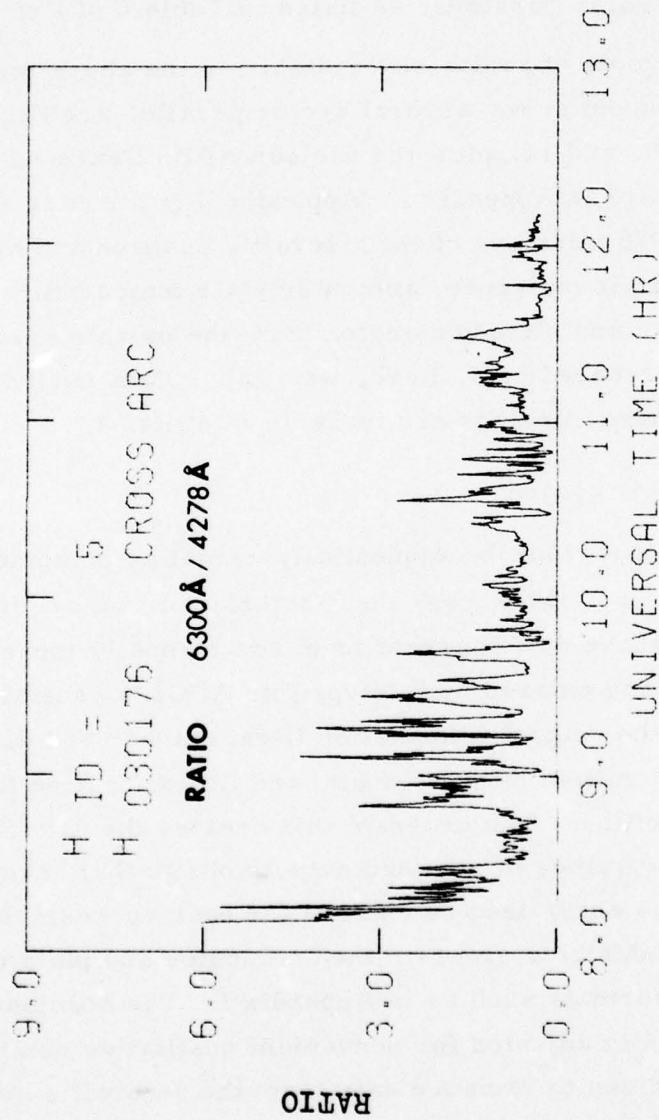


Figure 35. Ratio of column intensities of the OI 6300 Å line to the N₂ First Negative (0, 1) band, ICECAP 76-5.

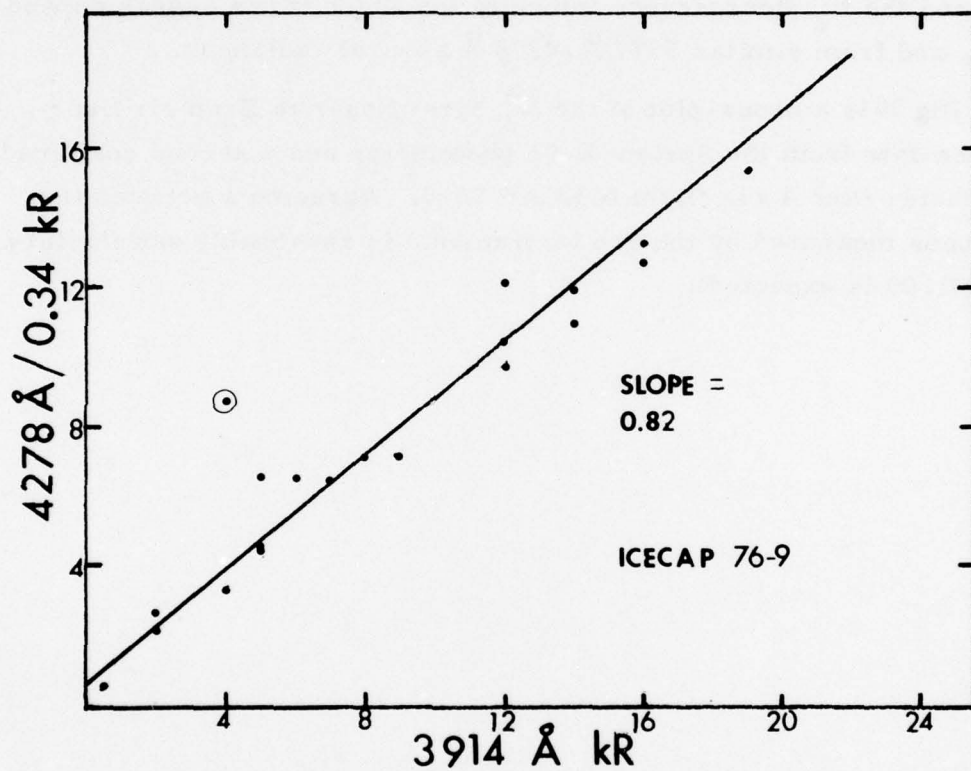


Figure 36. Scatter plot of N_2^+ First Negative fluorescence intensities, with a least-squares fit to the 4278 Å data from the multi-channel photometer. The circled point has been omitted in the fit calculation.

A major such application of these radiances is to computing an altitude profile of volume ionization rate by the primary precipitating electrons, using photon intensity ratios in auroral-emission features (see Appendix II of Ref 3). An example of $6300 \text{ \AA}/4278 \text{ \AA}$ column ratios from the 1976 data files is shown in Fig 35. A program is being written to calculate directly the altitude of peak energy deposition from this ratio and the N_2^+ fluorescence intensity (on which it has a weak dependence), and from similar $5577 \text{ \AA} - 4278 \text{ \AA}$ auroral radiances.

Fig 36 is a cross-plot of the N_2^+ First Negative Band air fluorescence data from the System E-05 photometer and a second coaligned photometer (Ref 4) in flight ICECAP 76-9. Agreement between the radiances measured by the two instruments is reasonably satisfactory (slope 1.00 is expected).

REFERENCES

1. I. L. Kofsky et al., Data Reduction and Auroral Characterizations for ICECAP, HAES Report No. 4, DNA 3511F (10 Apr 75).
2. I. L. Kofsky, R. B. Sluder, and C. A. Trowbridge, Data Reduction and Auroral Characterizations for ICECAP II, HAES Report No. 27, DNA 3789F (25 Oct 75).
3. I. L. Kofsky, D. P. Villanucci, and R. B. Sluder, Data Reduction and Auroral Characterizations for ICECAP III, HAES Report No. 59, DNA 4220F (31 Jan 77).
4. A. T. Stair, Jr., and J. C. Ulwick (ed's), Proceedings of the HAES Infrared Data Review, AFGL-OP-TM-05, Jun 77.
5. J. B. Kumer, Analysis of 4.3 μ m ICECAP Data, HAES Report No. 19, AFCRL-TR-74-0334, (Jul 74).
6. Analysis and Simulation Branch AFCRL Computation Center, Aspect Report for Rocket No. A18.219-1, Aspect Report No. 4598, (undated)
7. A. T. Stair, Jr., and R. Nadile (AFGL), private communication (Oct 77).
8. H. Mitchell, 2.8 Micron Emission Further Examination of DNA/AFGL Data and Probable Causes, Unpublished Report (Feb 77).
9. W. F. Grieder and L. A. Whelan, Geometric Aspects of Rocket Photometry, HAES Report No. 41, AFGL-TR-76-0046 (Feb 76).
10. D. A. Burt and C. S. Davis, Rocket Instrumentation for Icecap 73A Auroral Measurements Program - Black Brant 18.205-1, HAES Report No. 3, AFCRL-TR-74-0195 (Feb 74).
11. Reference Atmosphere CIRA 72, Akademie Verlag, Berlin, 1972.
12. M. H. Rees and D. Luckey, J. Geophys. Res. 71, 5181 (1974).
13. J-C. Gerard and O. E. Harang, in Physics and Chemistry of Upper Atmospheres (ed B. McCormac), Reidel, Dordrecht, 1973, p241.
14. R. H. Eather and S. B. Mende, J. Geophys. Res. 76, 1746 (1971).

REFERENCES (continued)

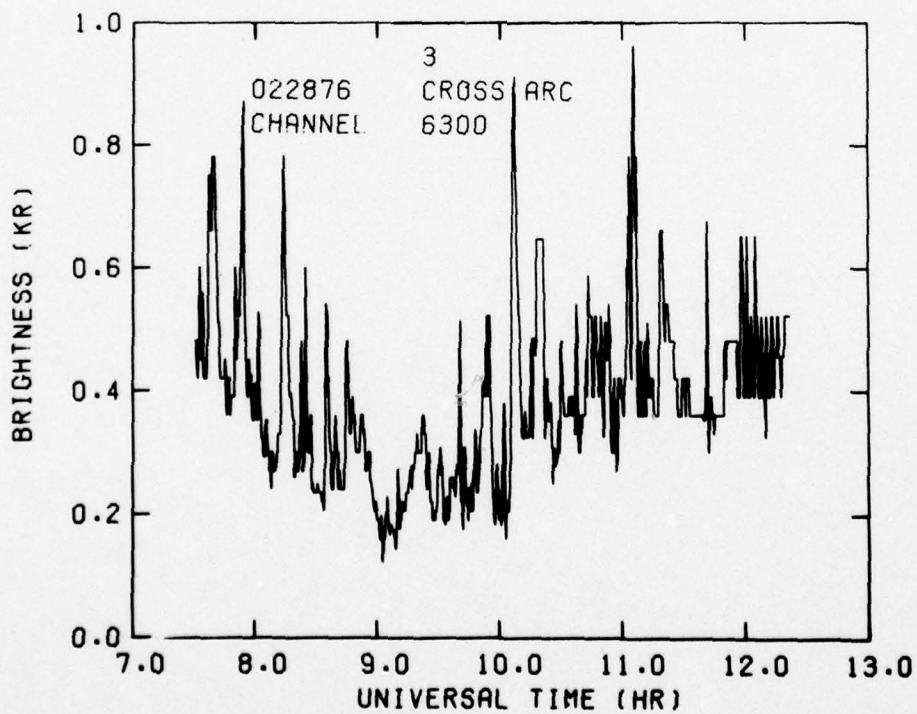
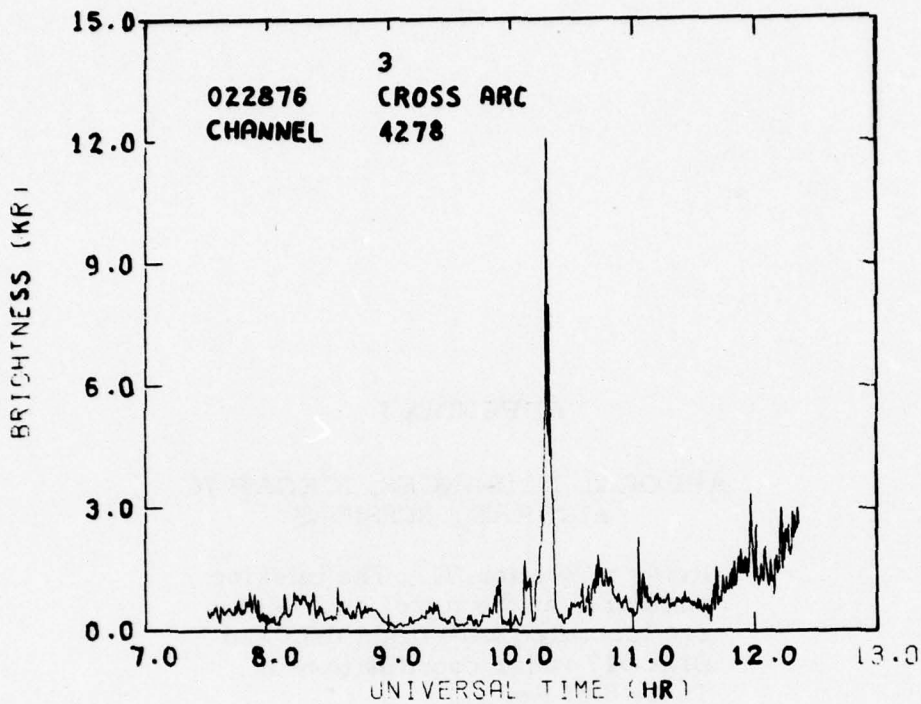
15. R. L. Gattinger and A. Vallance Jones, *Can. J. Phys.* 52, 2343 (1974).
16. W. R. Pendleton, Jr., and R. R. O'Neil, *J. Chem. Phys.* 56, 6260 (1972).
17. A. Vallance Jones, *Space Sci. Rev's.* 11, 826 (1971).
18. H. Nishimura, *J. Phys. Soc. Japan* 21, 1018 (1966).
19. A. T. Stair, Jr., J. W. Rogers, and W. R. Williamson, Quick Look Data Report - HIRIS Experiment, AFGL-OP-TM-02, 15 Apr 76.
20. G. J. Romick, Report on the Geophysical Description and Available Data Associated with Rocket PF-SGT-116 (IC630.02-1A), HAES Report No. 63, AFGL-TR-77-0073, Mar 77.
21. T. M. Watt, HIRIS Experiment - Chatanika Radar Results, DNA 4229T, Jan 77.
22. Aspect and trajectory listings for IC630.02-1A, from AFGL/OPR (1976).
23. I. L. Kofsky, J. D. Geller, and C. A. Trowbridge, Sky Background Measurement Program, AFCRL-70-0012 (PhM-101-69), 30 Nov 69.
24. J. W. Reed (Visidyne, Inc.), private communication (Sep 77).

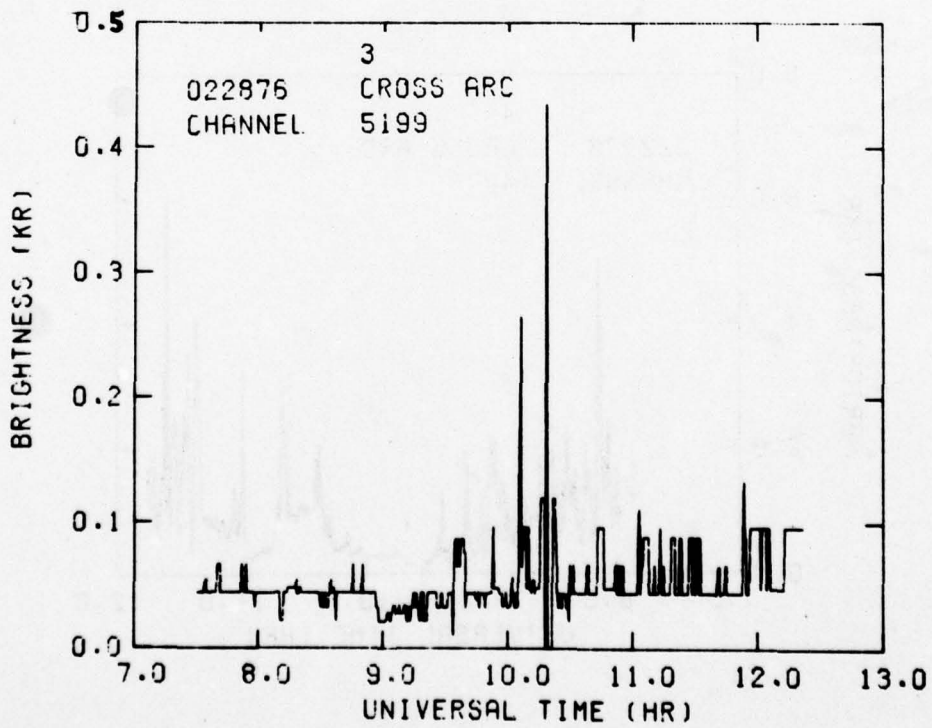
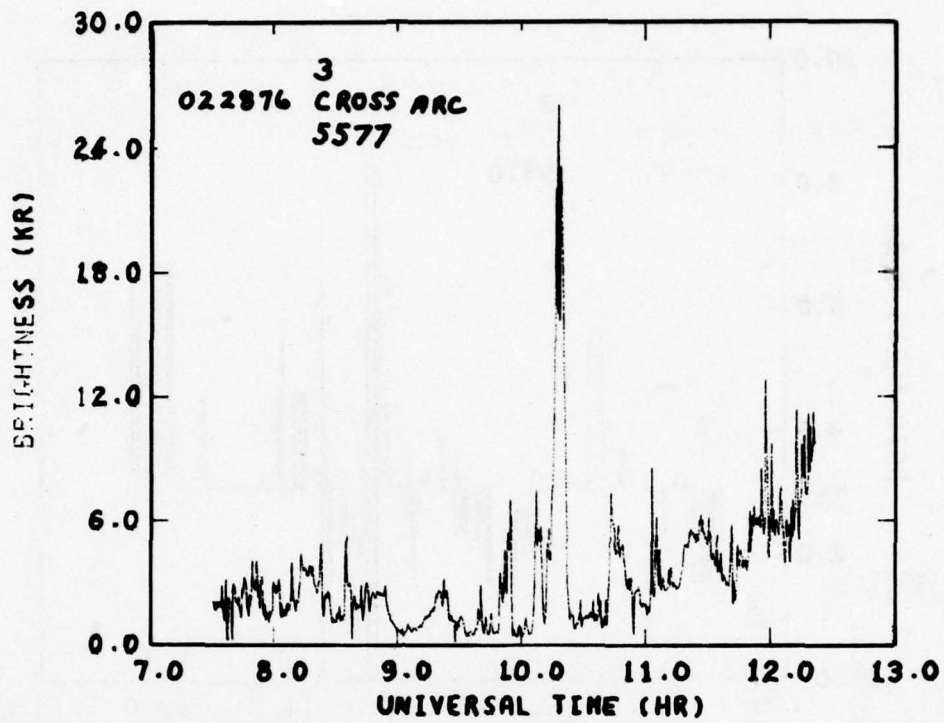
APPENDIX I

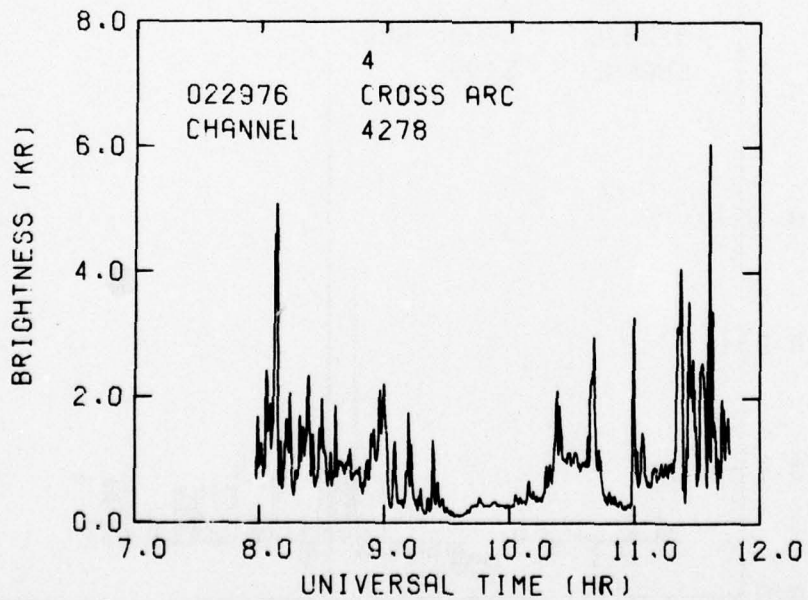
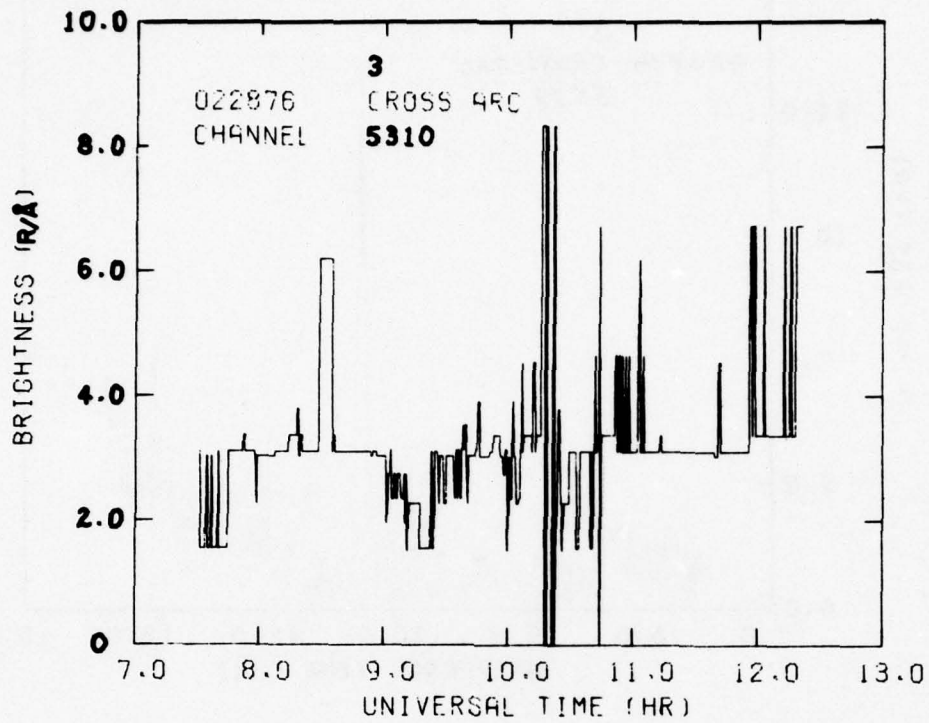
AURORAL RADIANCES, ICECAP 76
AIRCRAFT MISSIONS

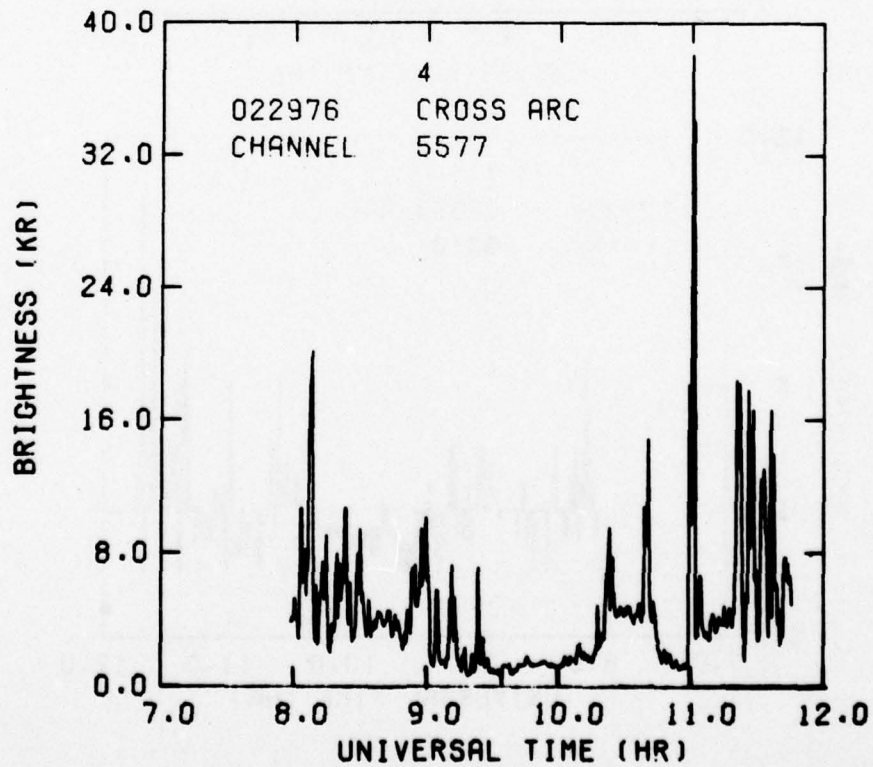
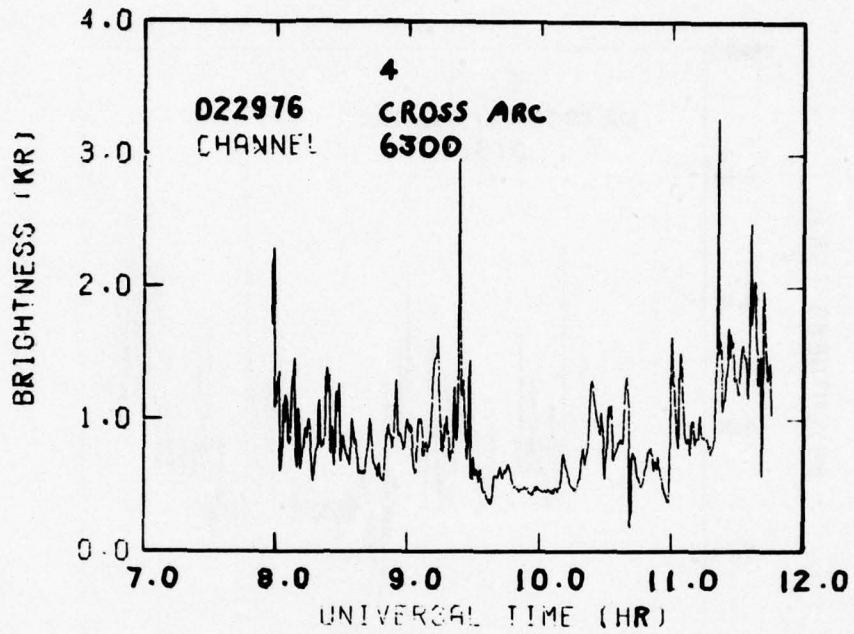
(Refer to Section VI. The mission numbers, at the top of each plot, are identified with flight data and DNA 617 radar coordination in Table 8 of Ref 3.)

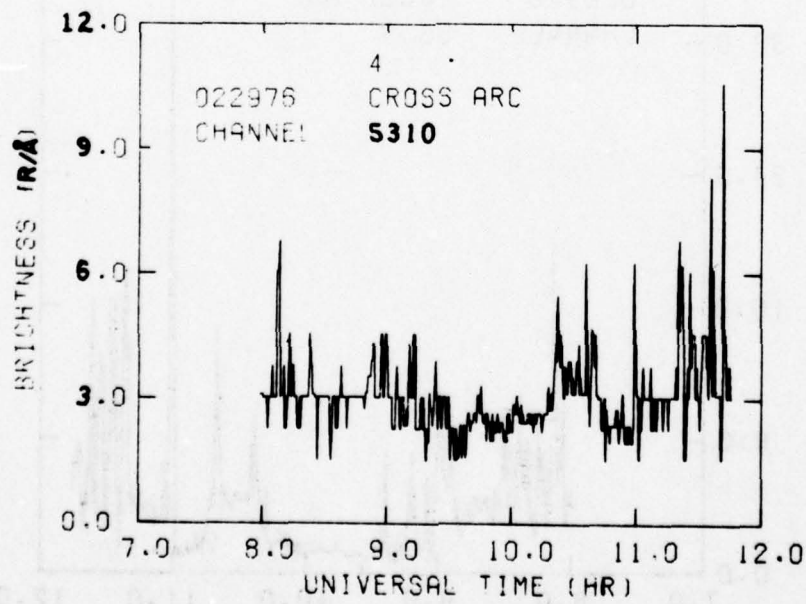
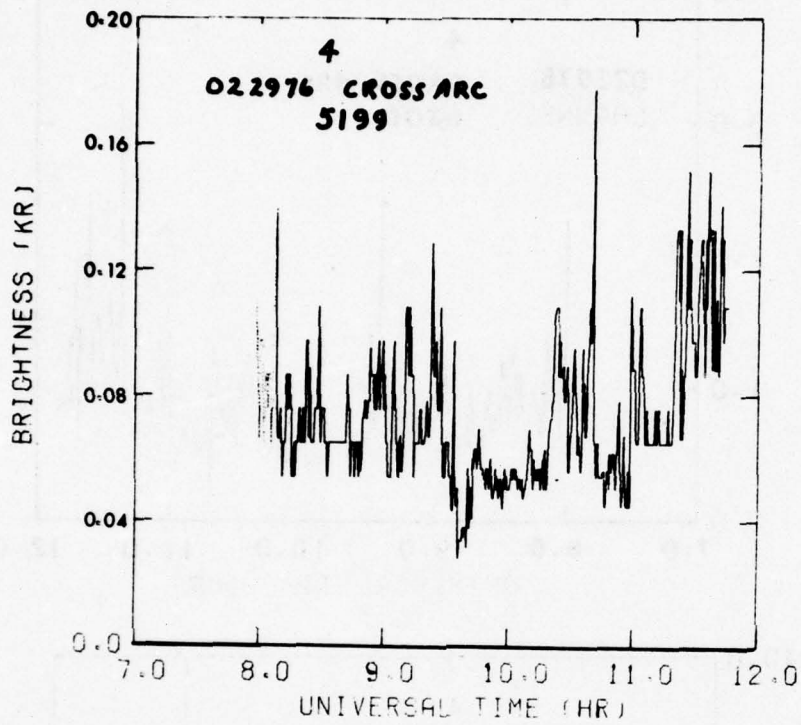
THIS PAGE IS BEST QUALITY PRACTICABLE
FROM COPY FURNISHED TO EDC

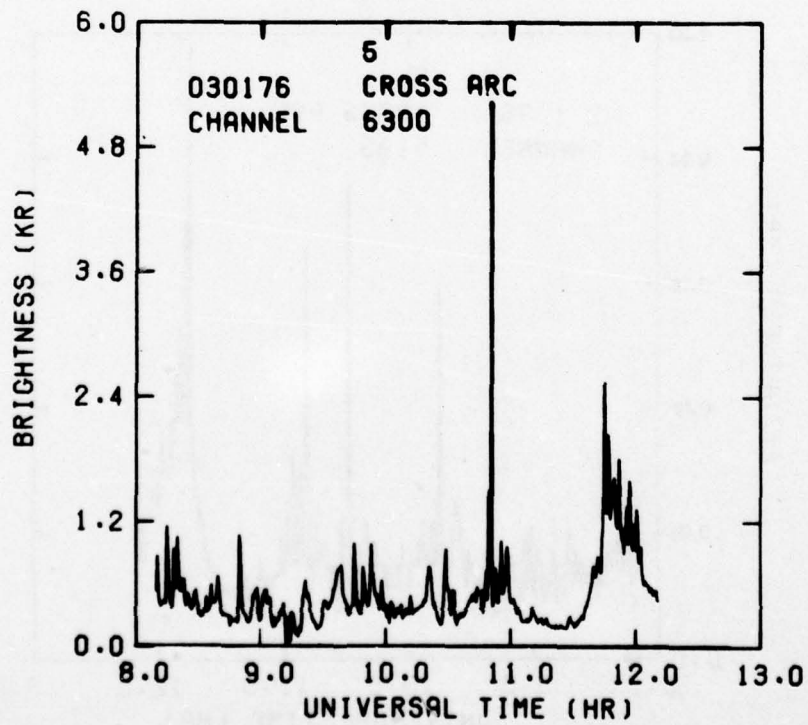
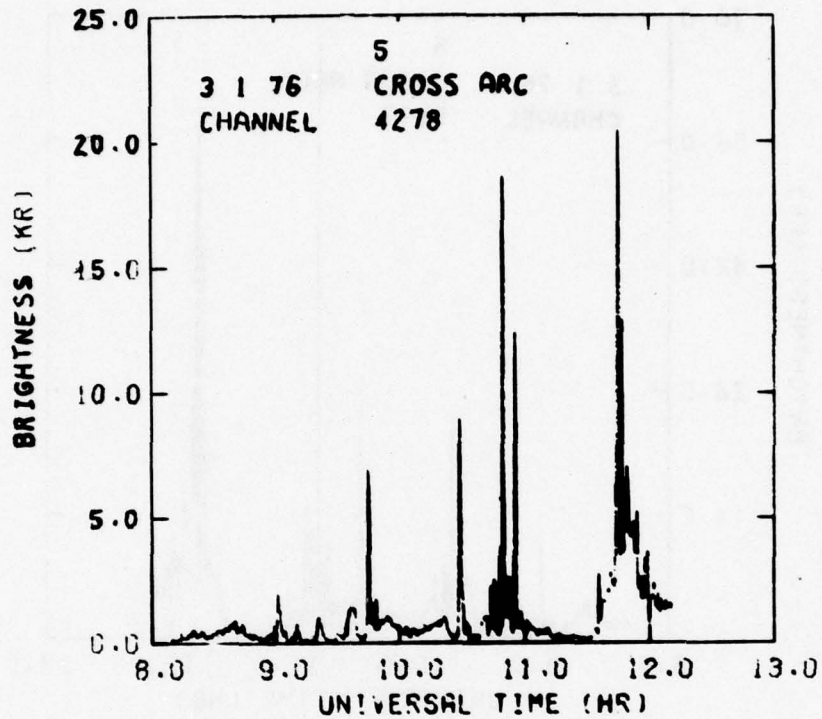


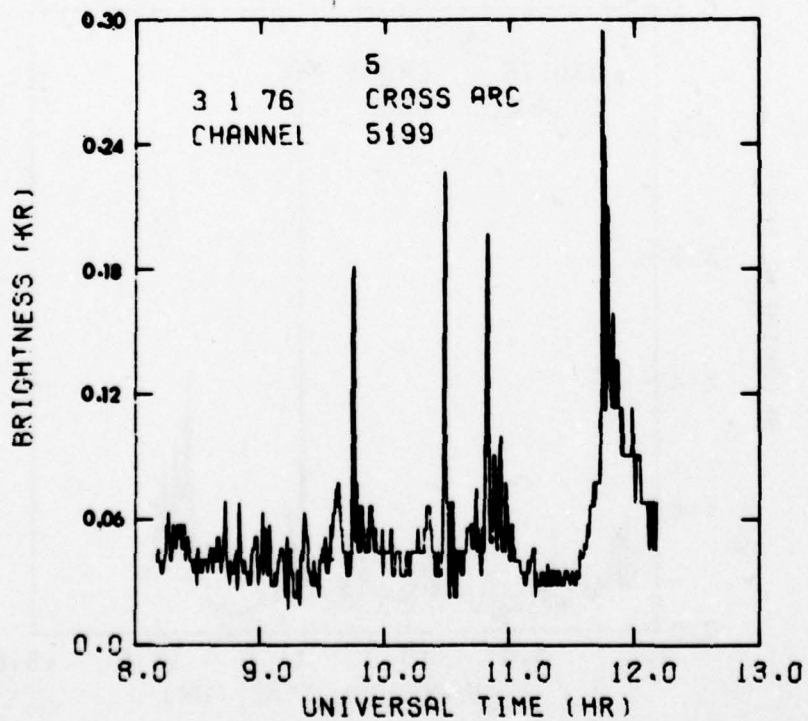
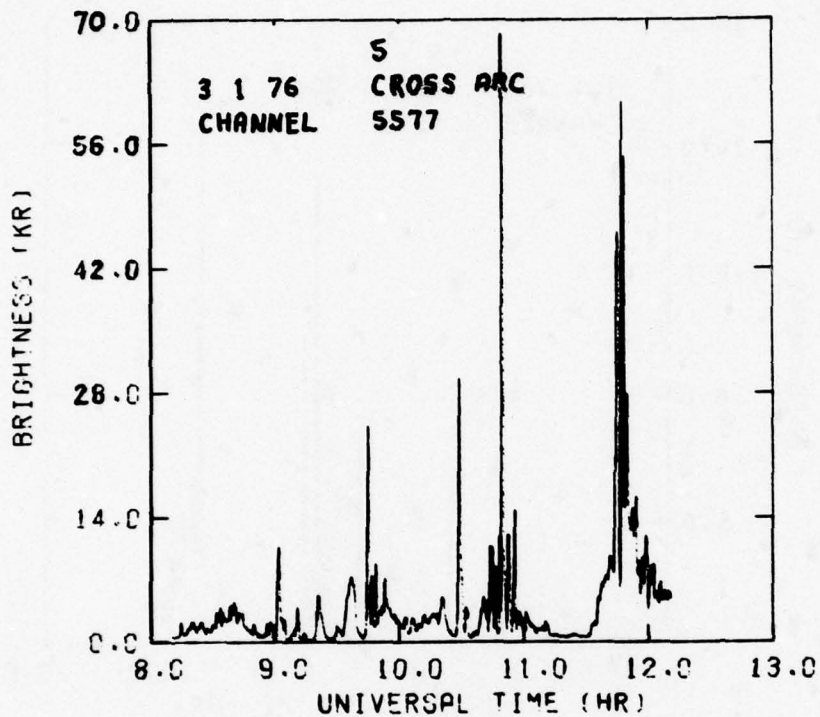


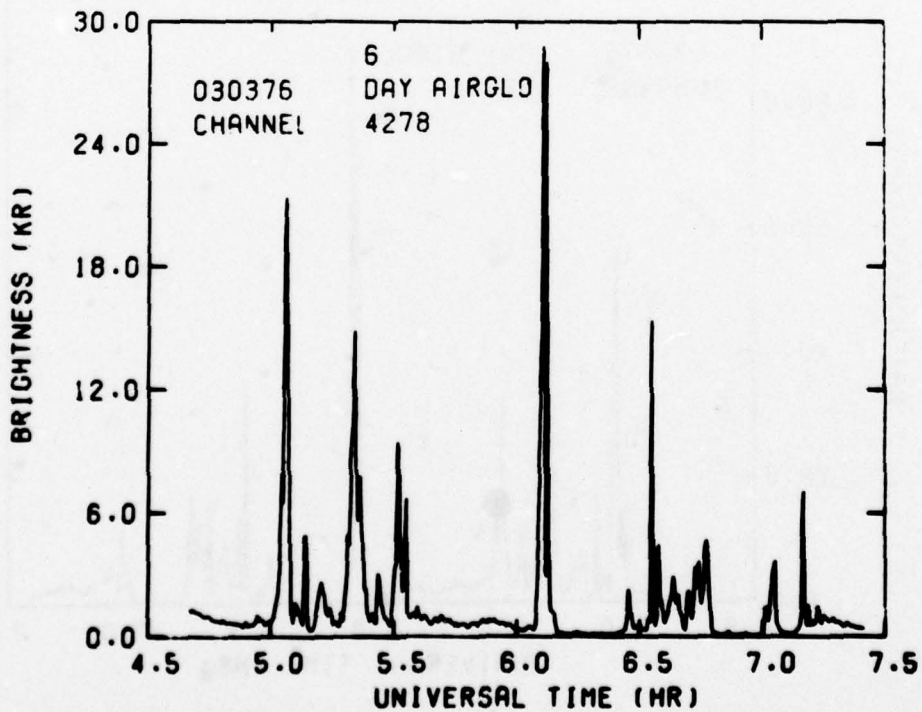
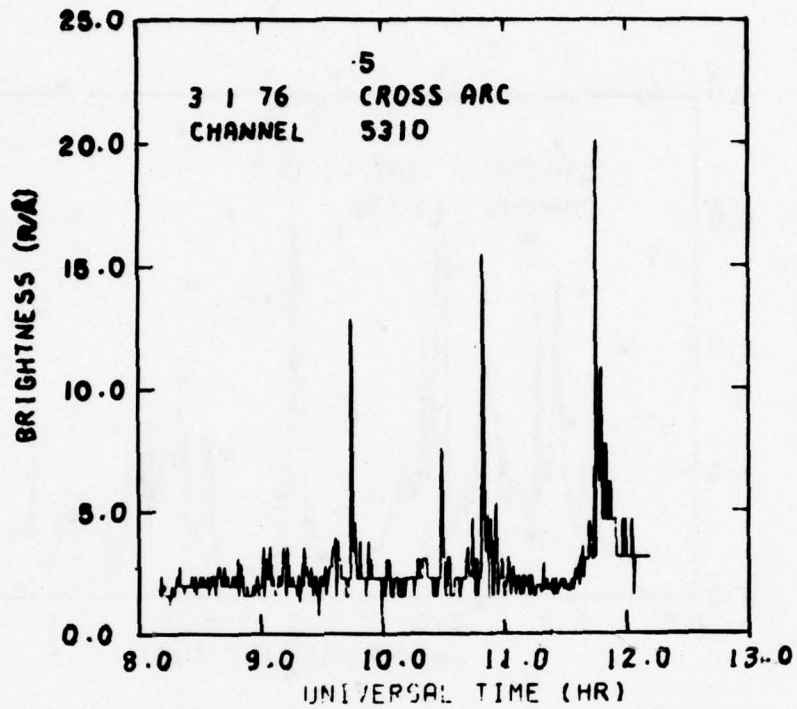


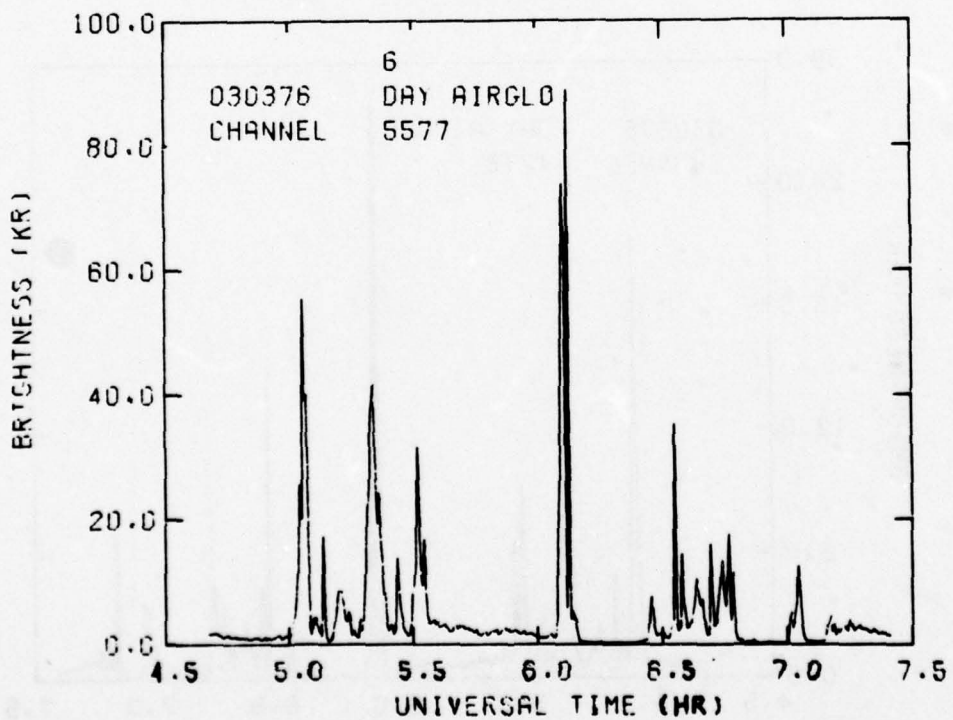
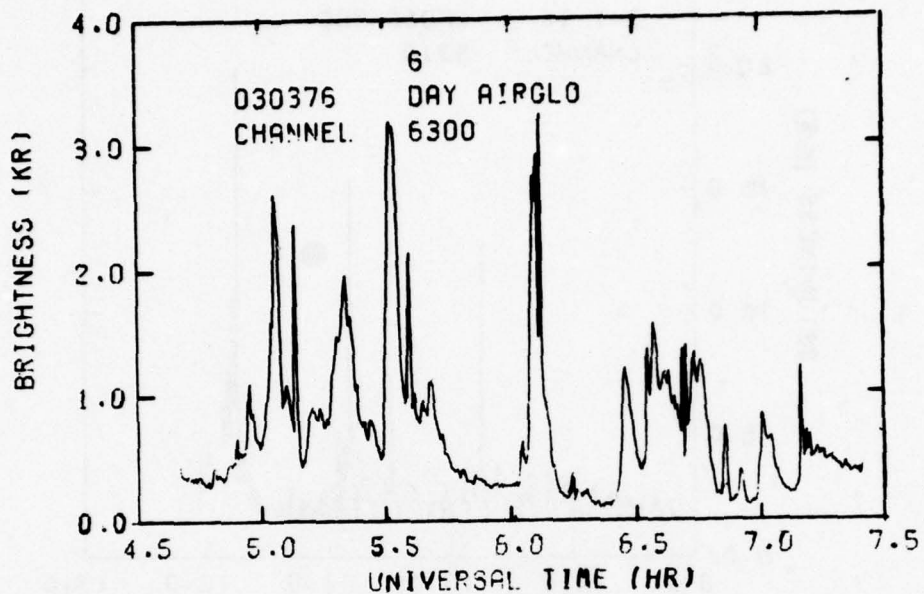




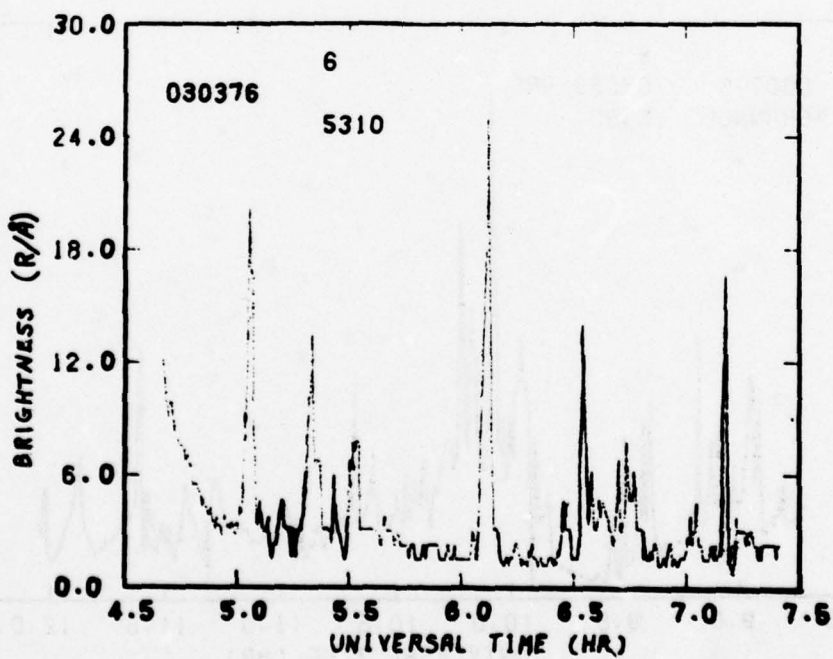
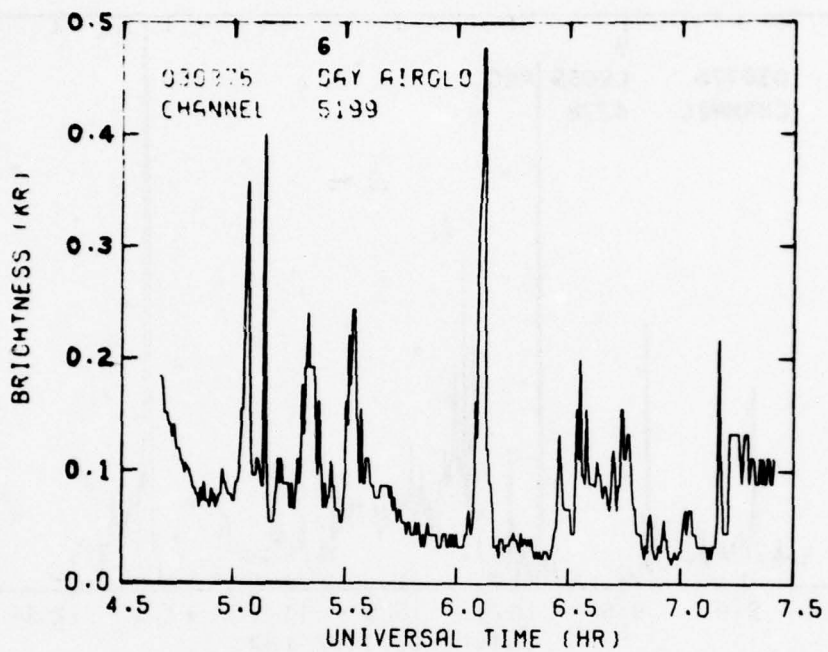




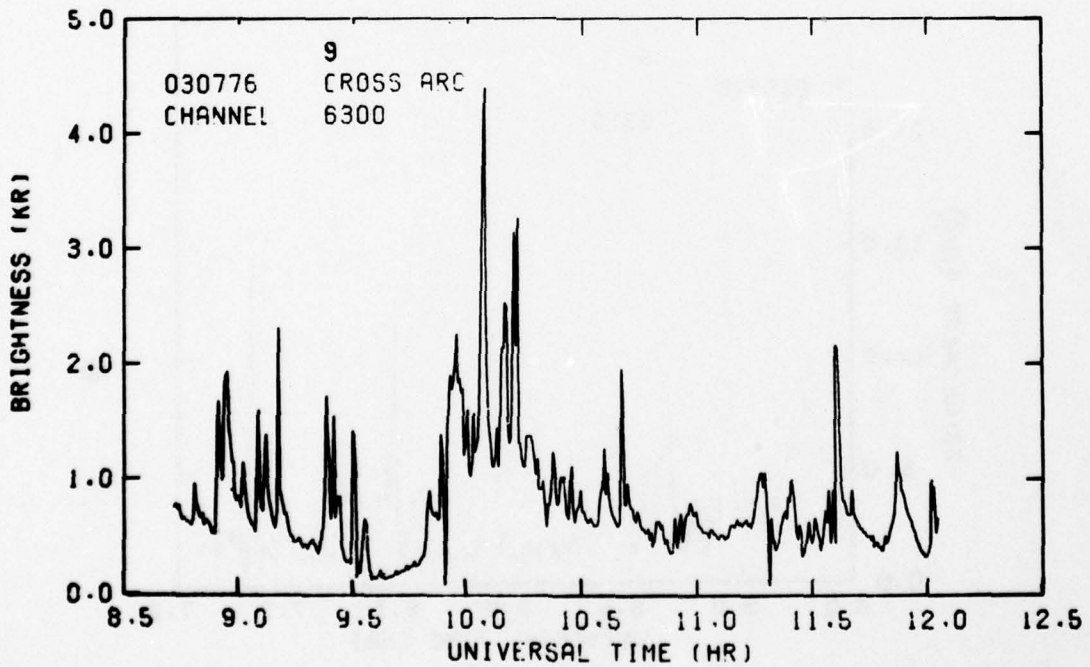
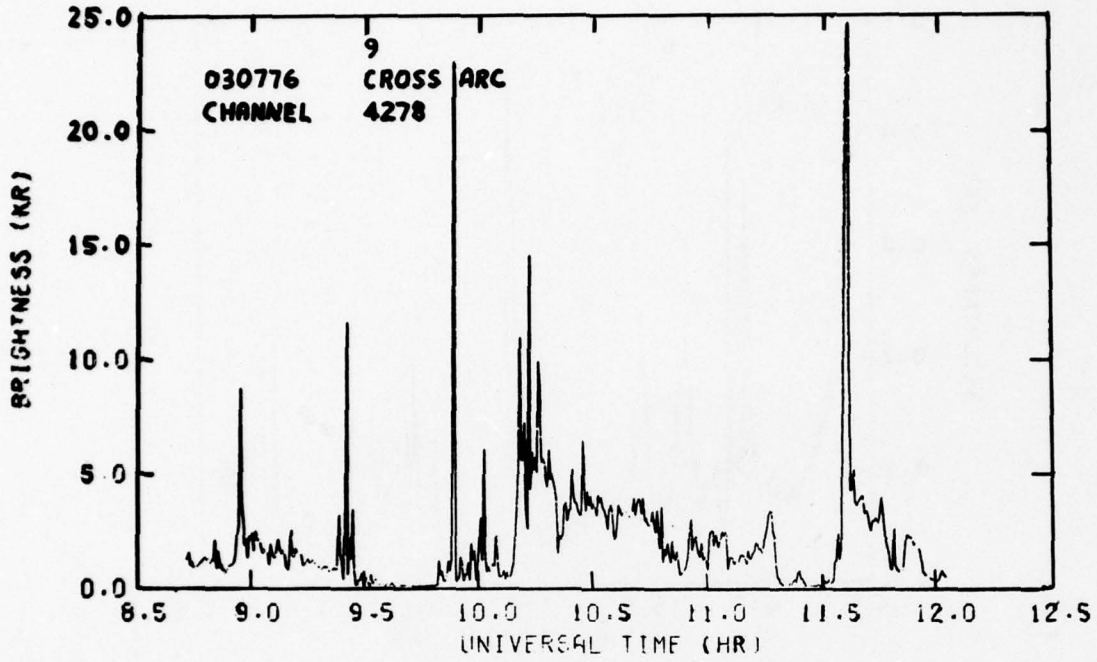




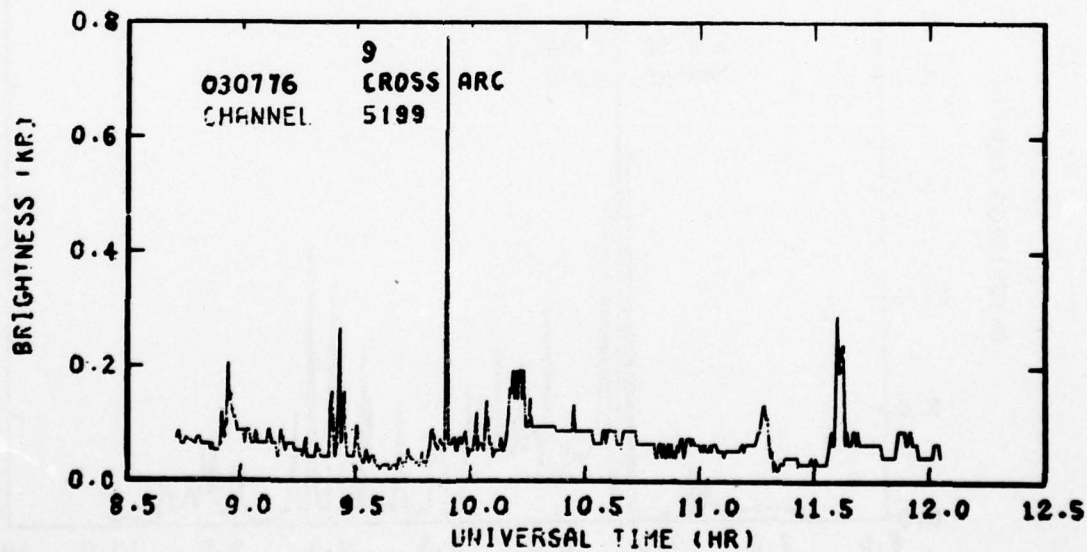
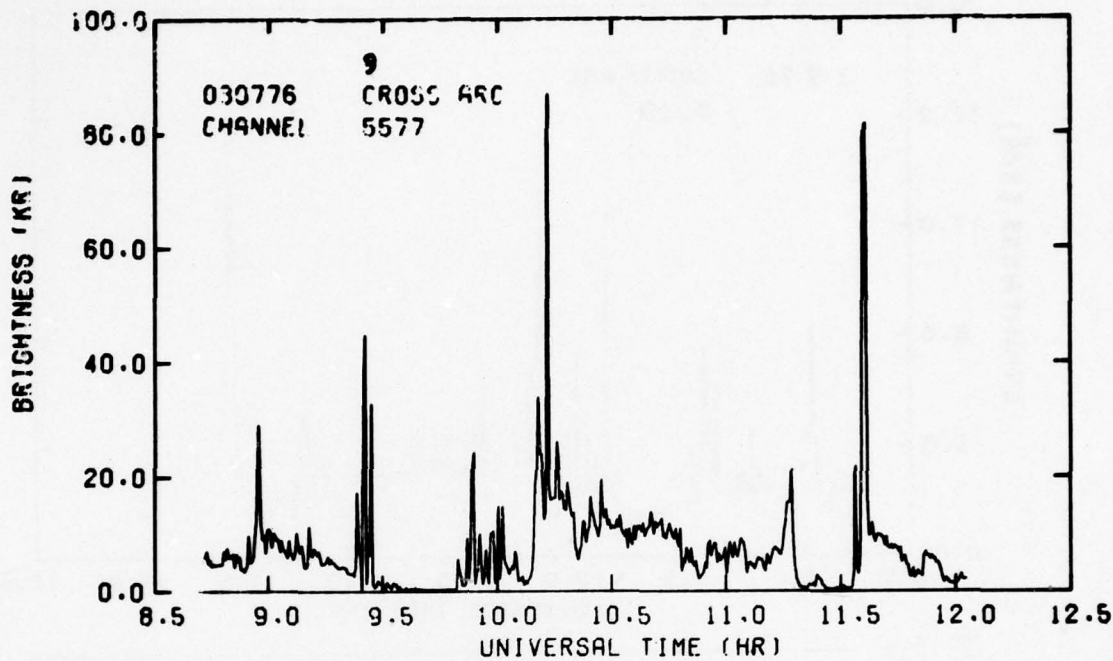
THIS PAGE IS BEST QUALITY PRACTICABLE
FROM COPY FURNISHED TO DDC



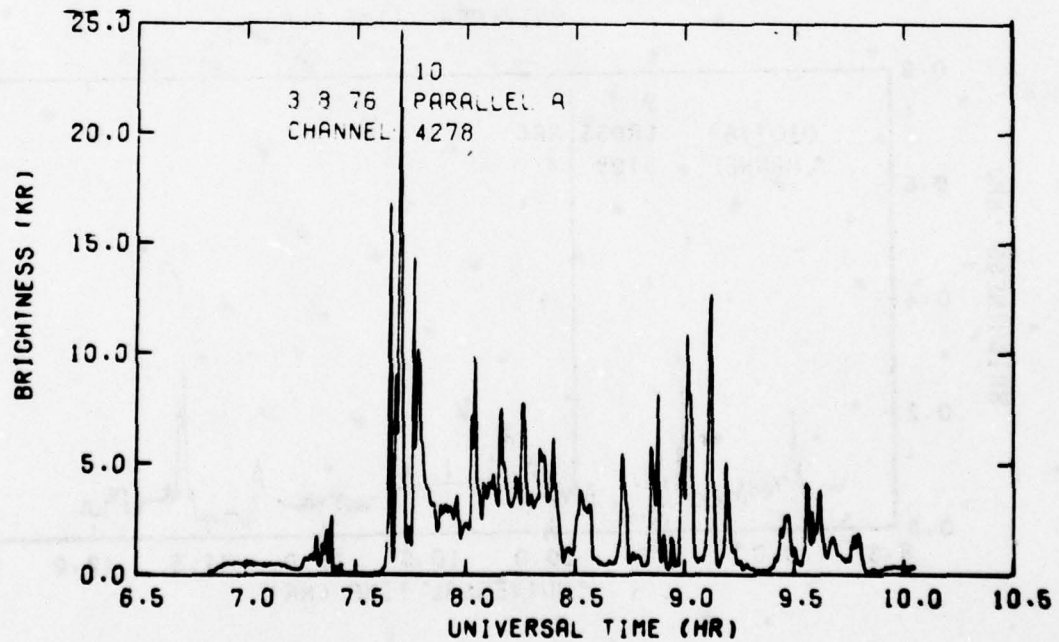
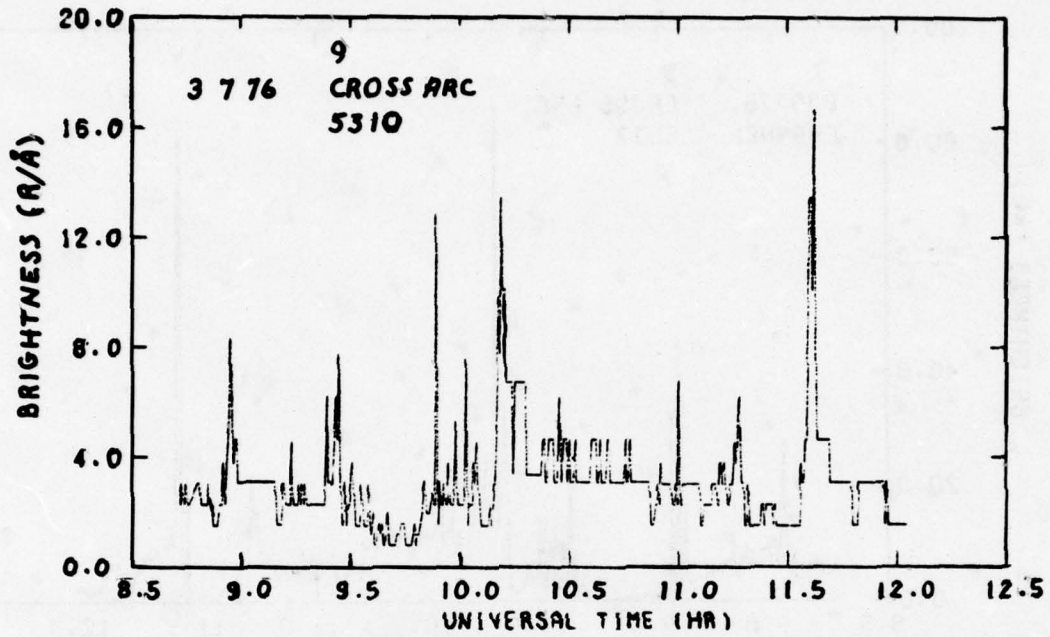
THIS PAGE IS BEST QUALITY PRACTICABLE
FROM COPY FURNISHED TO DDC



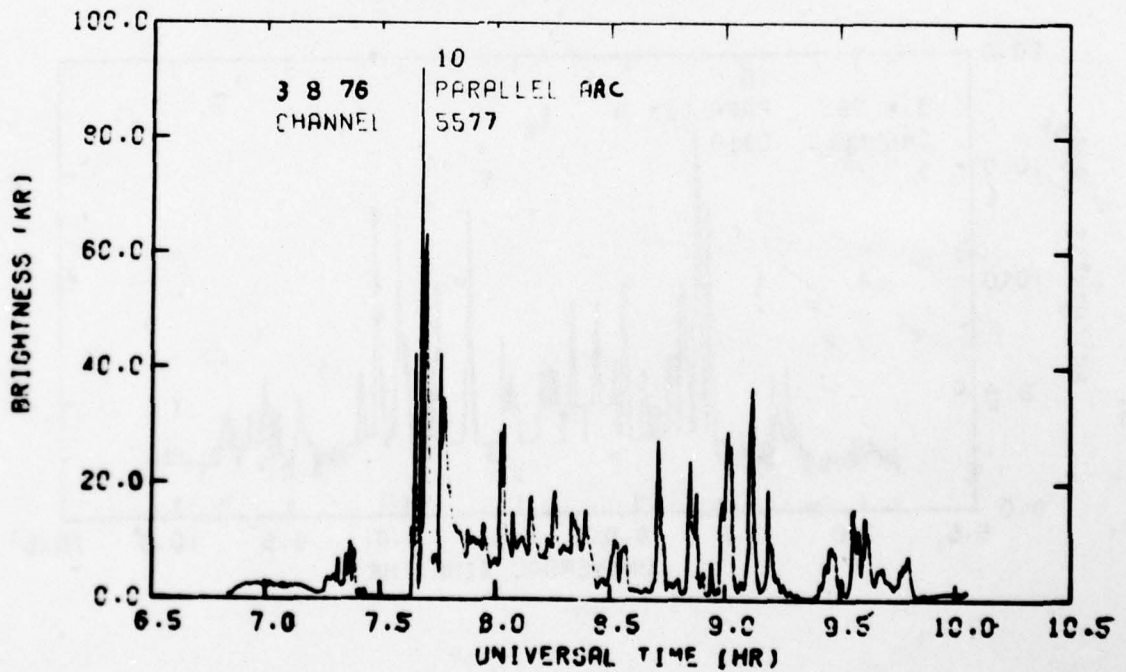
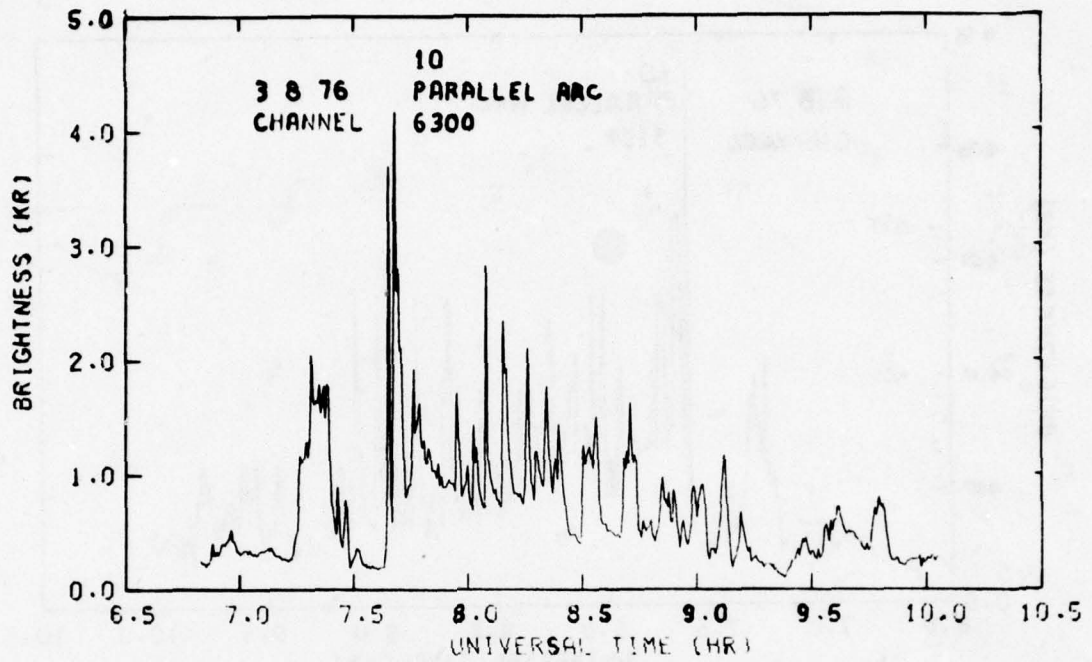
THIS PAGE IS BEST QUALITY PRACTICABLE
FROM COPY FURNISHED TO DDG



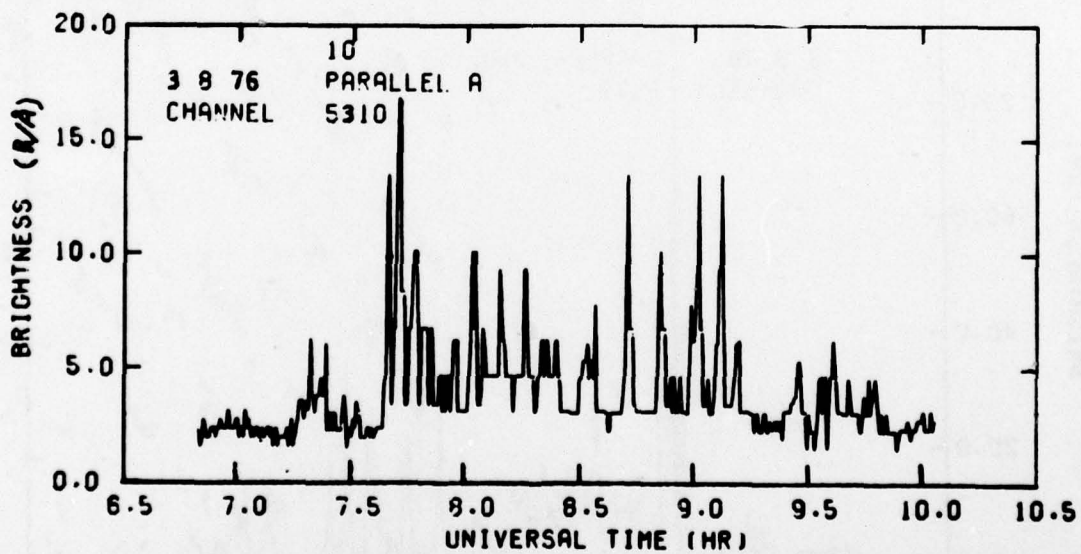
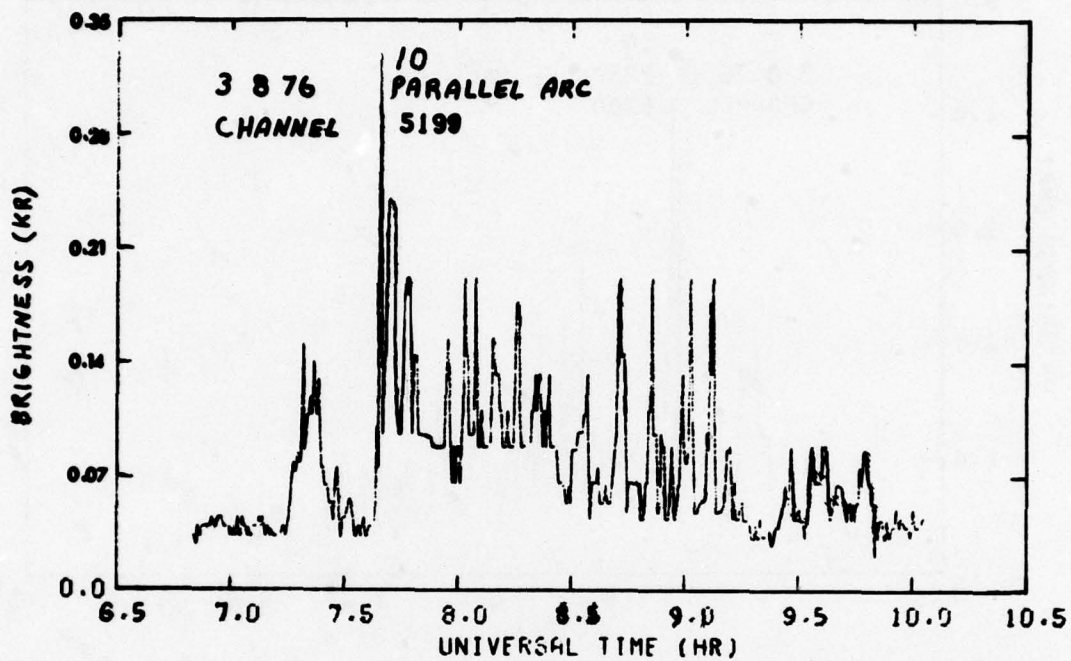
THIS PAGE IS BEST QUALITY PRACTICABLE
FROM COPY FURNISHED TO DDG



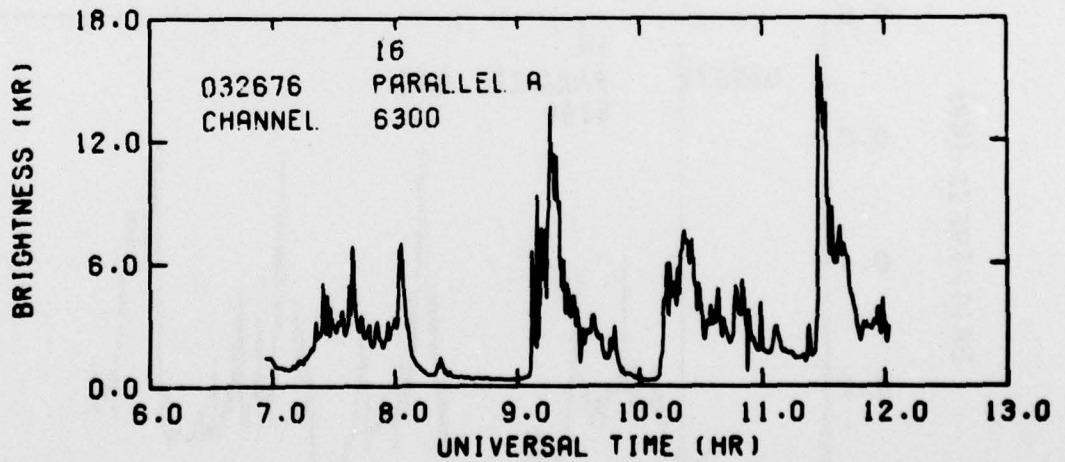
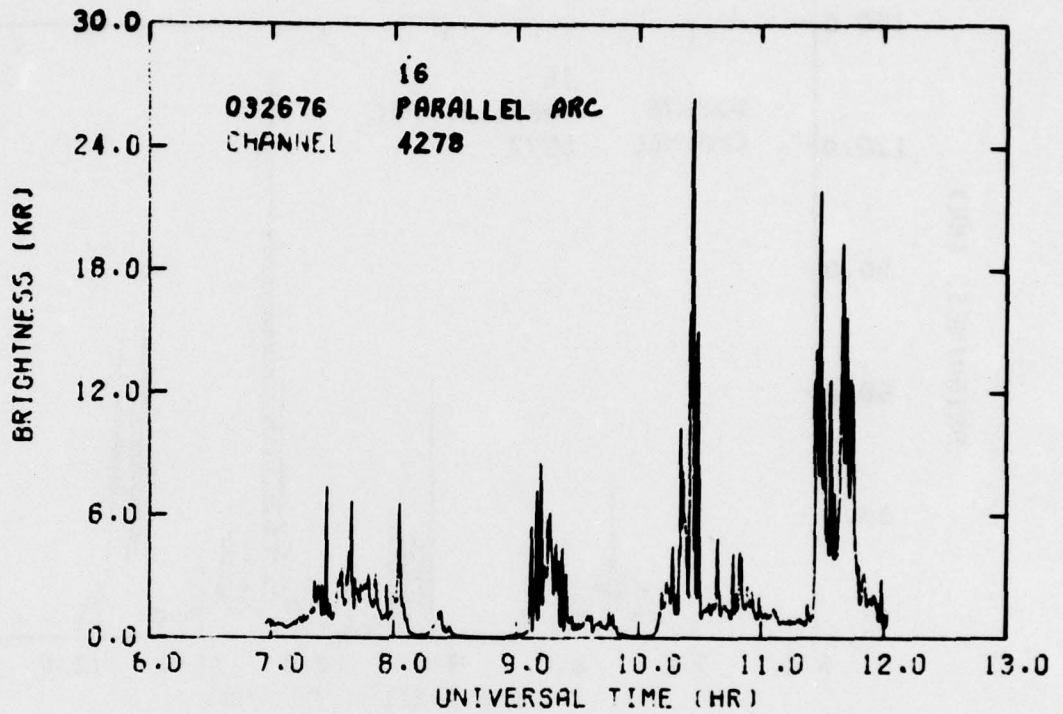
THIS PAGE IS BEST QUALITY PRACTICABLE
FROM COPY FURNISHED TO DBQ



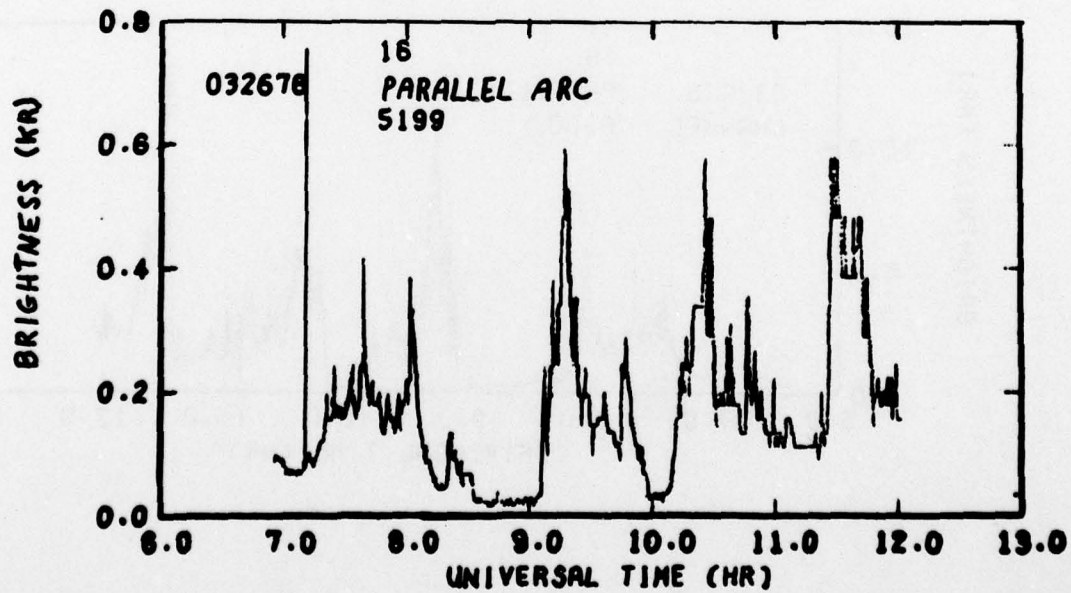
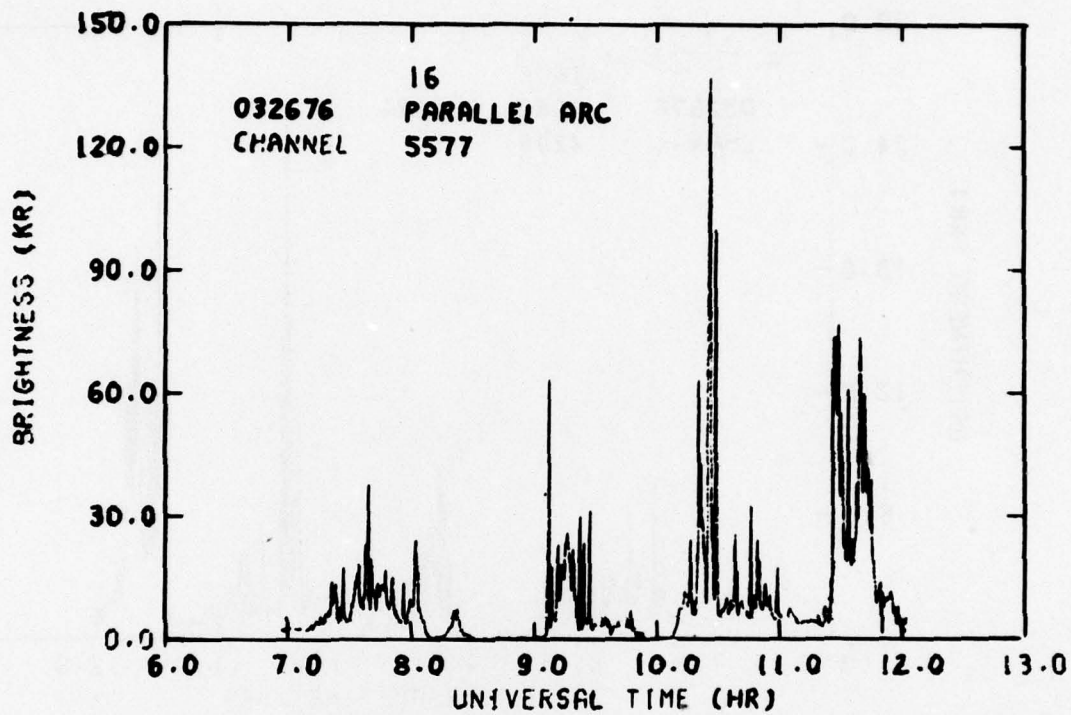
THIS PAGE IS BEST QUALITY PRACTICABLE
FROM COPY FURNISHED TO ADG



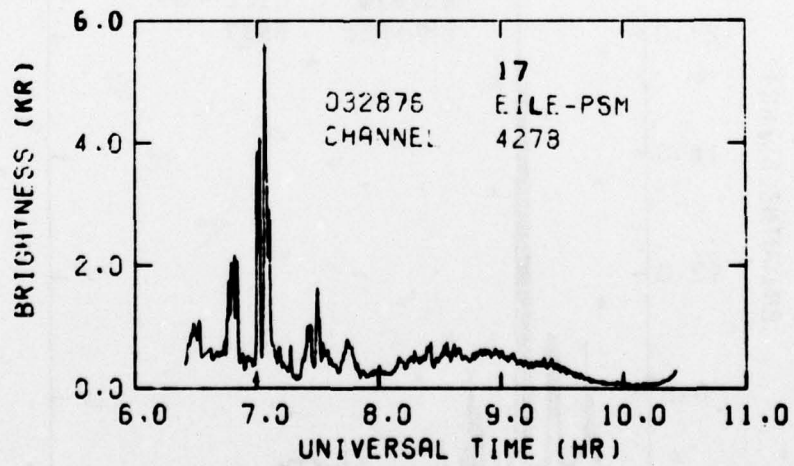
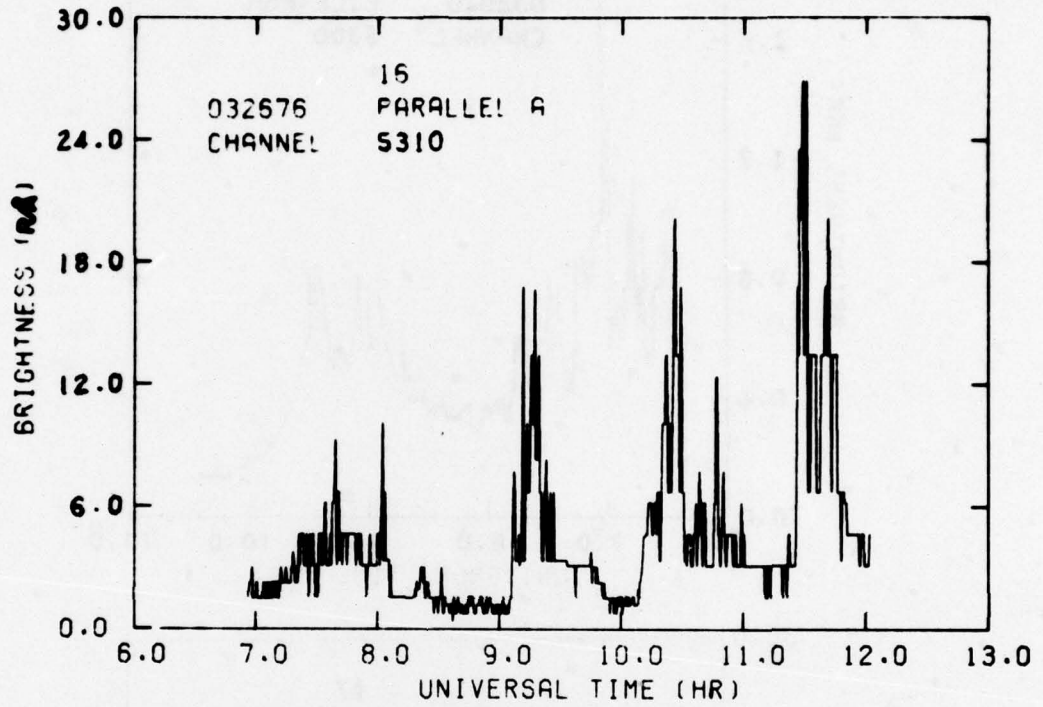
THIS PAGE IS BEST QUALITY PRACTICABLE
FROM COPY FURNISHED TO DDC



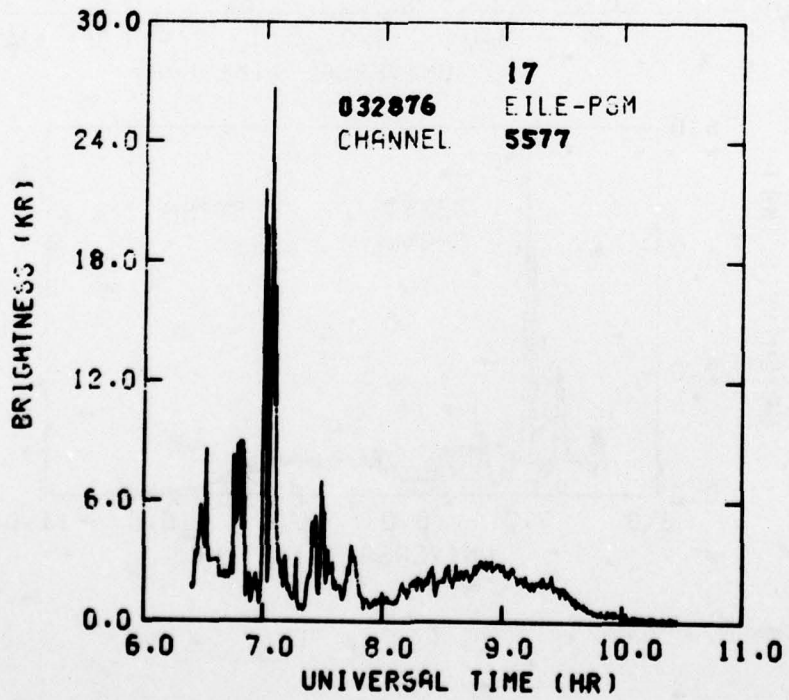
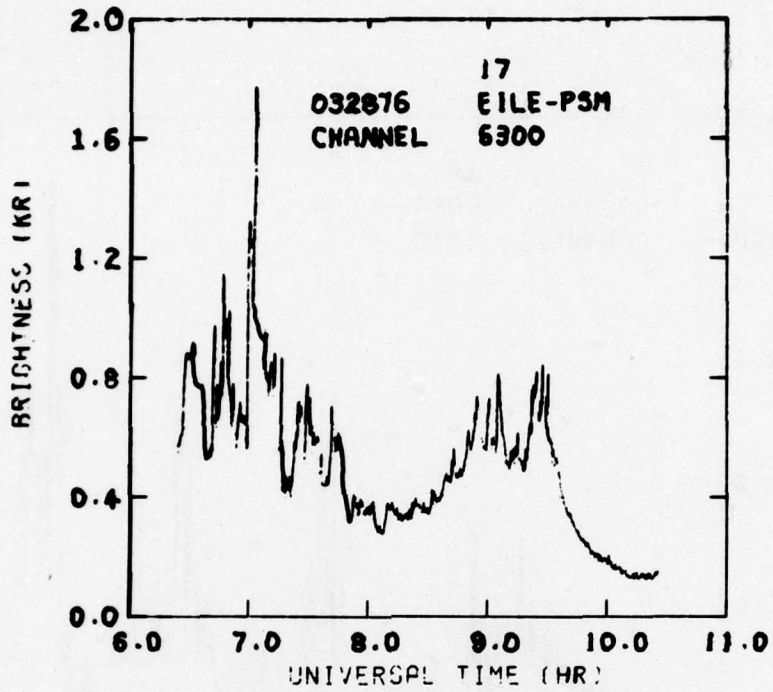
THIS PAGE IS BEST QUALITY PRACTICABLE
FROM COPY FURNISHED TO DDG



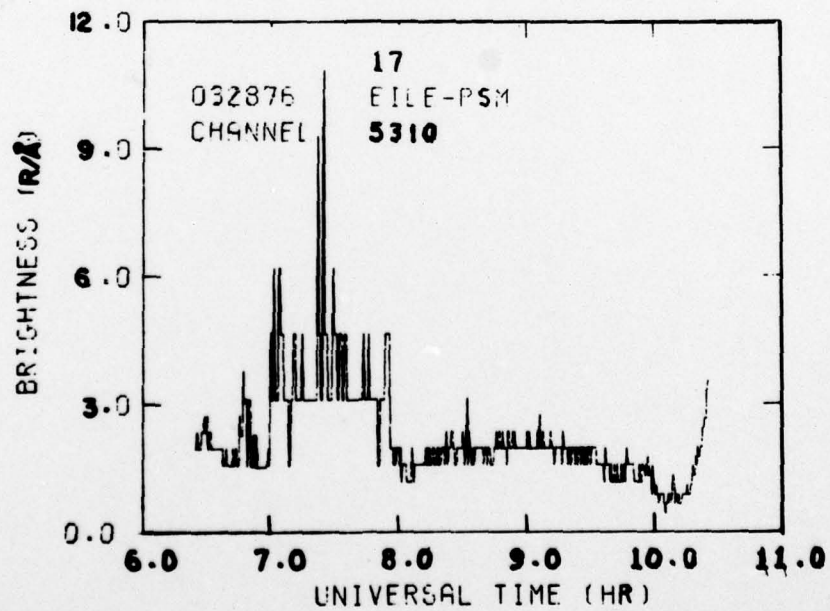
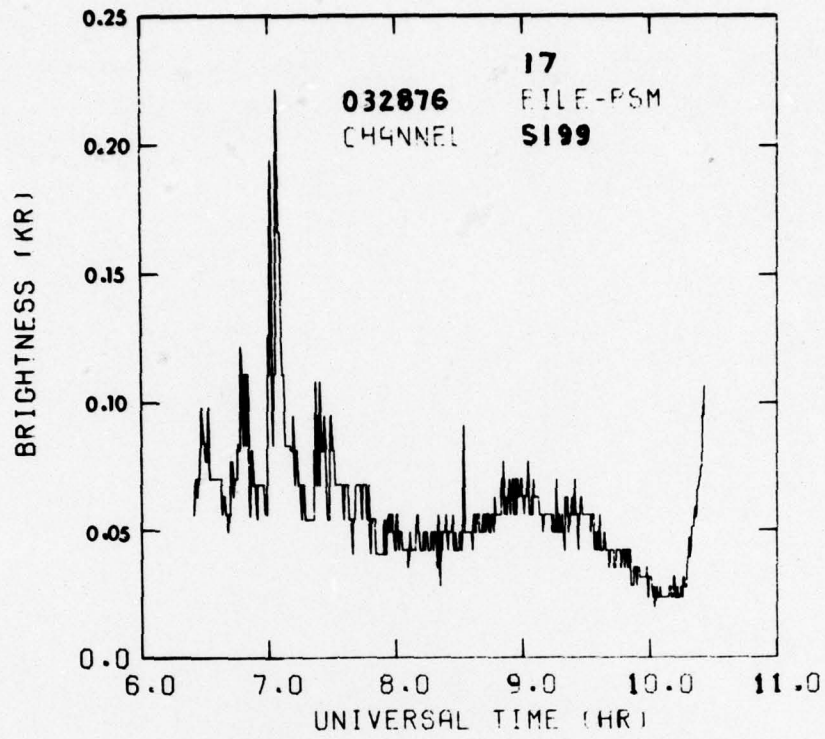
THIS PAGE IS BEST QUALITY PRACTICABLE
FROM COPY FURNISHED TO DDG



THIS PAGE IS BEST QUALITY PRACTICABLE
FROM COPY FURNISHED TO DDG



THIS PAGE IS BEST QUALITY PRACTICABLE
FROM COPY FURNISHED TO DDC



THIS PAGE IS BEST QUALITY PRACTICABLE
FROM COPY FURNISHED TO DDC

APPENDIX II

POSITION AND HEADING OF ICECAP 76 AIRCRAFT

(Refer to Section VI. The flight numbers are identified with mission type in Table 6 of Ref 3.)

THIS PAGE IS BEST QUALITY PRACTICABLE
FROM COPY FURNISHED TO DDG

MISSION: **ICECAP 76-1** EN/ENL DATE: **22 FEB 1976**

TIME	LATITUDE		LONGITUDE		ALT	HEADING		SPEED		SOLAR ANGLE	
	N	W	N	E		MAG	TRUE	KTAS	KTGS	ELEV.	AZIM.
1525	42 05	70 17	170							29.5	158.8
1535	42 07	70 18								30.0	159.8
1540	42 26	70 53	280			321	308	450	420	26.3	165.6
1550	46 22	70 15	280			327	314	450	420	27.3	162.9
1630	50 01	83 04	300			327	308	450	420	27.6	168.8
1647	51 32	84 57	310			311	307	450	420	26.6	164.7
1710	53 00	87 46	310			314	313	450	380	26.6	165.1
1720	53 41	87 20	310			311	313	450	370	26.1	166.0
1750	55 26	93 27	350			305	313	450	340	23.8	161.9
1805	56 12	95 33	350			308	316	450	330	23.3	171.6
1825	57 27	97 35	350			216	302	450	325	22.1	174.6
1840	58 04	100 05	350			223	301	450	320	21.5	176.3
1840	61 26	109 23	350			248	280	450	320	18.3	182.3
2020	62 32	118 26	350			245	278	450	320	17.8	182.2
2040	63 06	123 20	350			243	278	460	320	16.6	183.0
2100	64 05	129 31	350			240	274	450	320	16.1	183.1
2130	64 57	136 12	350			239	270	450	320	15.8	183.9
2135	64 16	138 14	350			234	266	450	320	15.4	182.1
2225	64 40	147 06	350							15.0	183.3

MISSION: **ICECAP 76-2** EN/ENL DATE: **26 FEB 1976**

TIME	LATITUDE		LONGITUDE		ALT	HEADING		SPEED		SOLAR ANGLE	
	N	W	N	E		MAG	TRUE	KTAS	KTGS	ELEV.	AZIM.
1515	64 40	147 06	350							13.0	183.3
1545	65 11	147 30	350			18.0	209	450	410	10.1	189.8
1600	65 12	147 30	350			350	250	480	420	3.4	193.0
1610	66 10	146 30	350			358	239	500	440	4.9	196.6
1620	67 16	144 30	350			355	226	500	440	5.4	198.9
1630	67 16	144 30	350			178	209	480	450	4.9	192.3
1640	66 12	146 15	350			178	207	480	440	3.9	198.1
1650	65 03	147 30	350			178	206	400	440	3.2	199.2
1705	64 04	148 05	350			175	203	395	435	2.5	195.2
1710	64 00	148 12	350			357	025	500	440	1.3	197.8
1720	65 00	147 30	350			357	026	500	435	0.1	191.0
1730	66 04	146 15	350			358	028	500	432	0.9	184.5
1746	67 16	144 30	350			358	026	500	430	1.9	180.8
1750	67 16	144 30	350			178	207	390	440	2.5	191.4
1800	66 12	146 12	350			357	028	500	430	4.2	193.5
1810	66 17	146 16	350			360	032	500	435	5.0	197.6
1829	67 16	144 30	350			179	209	380	435	5.8	199.9
1839	66 11	146 00	350			180	209	380	435	6.8	198.8
1849	66 11	146 00	350			174	203	360	430	7.7	191.0
1900	64 04	148 08	350			176	203	400	430	8.9	193.6
1911	64 04	148 08	350			360	028	500	440	9.8	195.4
1921	65 08	147 28	350			357	028	500	435	10.3	199.3
1931	66 12	146 00	350			358	028	500	430	10.4	199.3
1941	67 16	144 31	350			358	029	500	430	10.4	199.3
1950	67 15	144 35	350			178	209	400	440	10.8	199.9
2000	66 14	146 00	350			180	209	380	440	11.2	199.0
2010	65 13	147 27	350			179	208	380	435	11.0	199.6
2020	64 03	149 00	350			176	209	380	430	10.3	199.6
2025	64 08	149 06	350			357	027	500	430	10.3	199.0
2030	65 12	148 00	350			357	027	500	430	10.1	198.7
2040	66 29	147 00	350			357	027	500	430	10.2	199.3
2045	66 25	147 00	350			172	209	400	440	10.3	199.0
2055	64 40	147 06	350			181	209	400	430	10.3	199.3

MISSION: **ICECAP 76-3** EN/ENL DATE: **28 FEB 1976**

TIME	LATITUDE		LONGITUDE		ALT	HEADING		SPEED		SOLAR ANGLE	
	N	W	N	E		MAG	TRUE	KTAS	KTGS	ELEV.	AZIM.
0704	64 40	147 06	350								
0730			350								
0801	65 08	147 30	350			010	038	450			
0811	66 12	146 00	350			357	028	495	440		
0821	67 14	144 24	350			357	028	495	440		
0831	67 16	144 30	350			177	208	402	440		
0841	66 12	146 07	350			178	207	403	440		
0851	65 09	147 30	350			175	202	410	440		
0901	64 02	148 46	350			177	204	410	440		
0910	64 05	148 55	350			004	031	490	440		
0920	65 06	147 25	350			003	032	490	440		
0930	66 10	146 05	350			358	029	493	440		
0940	67 12	144 40	350			352	025	490	440		
0950	67 20	143 10	350			353	026	492	430		
0950	68 06	142 00	350			353	026	492	430		
1005	67 48	141 12	250			179	213	400	440		
1016	67 07	143 45	350			182	213	402	440		
1026	66 00	145 46	350			172	202	410	440		
1036	65 00	147 04	350			172	202	410	440		
1041	65 00	146 45	350			002	032	490	440		
1051	65 56	144 55	350			345	021	445	440		
1101	67 04	143 48	350			345	015	445	440		
1110	67 06	143 52	350			177	208	430	440		
1120	66 02	145 25	350			174	209	420	450		
1130	65 01	146 53	350			176	204	410	440		
1140	63 55	148 16	350			042	070	410	460		
1220	64 40	147 06	350								

MISSION: **ICECAP 76-4** EN/ENL DATE: **29 FEB 1976**

TIME	LATITUDE		LONGITUDE		ALT	HEADING		SPEED		SOLAR ANGLE	
	N	W	N	E		MAG	TRUE	KTAS	KTGS	ELEV.	AZIM.
0723	64 40	147 06	350								
0808			350								
0824	64 32	148 08	350			177	205	440	445		
0830	64 40	147 48	350			360	028	490	430		
0836	64 40	147 48	350			187	204	440	420		
0836	64 03	148 47	350			271	298	490	450		
0846	64 30	148 55	350			003	029	490	440		
0856	65 35	149 45	350			359	027	490	435		
0906	66 42	149 12	350			001	031	485	438		
0916	67 47	146 46	350			259	030	460	440		
0926	68 50	145 10	350			358	029	490	440		
0936	68 55	145 00	350			179	210	410	440		
0946	67 30	146 38	350			178	208	435	440		
0956	66 48	148 28	350			178	208	435	440		
1006	65 45	149 45	350			176	203	445	440		
1016	64 40	151 00	350			171	196	460	440		
1026	63 40	152 05	350			171	196	460	440		
1036	62 38	153 15	350			004	030	490	450		
1045	64 38	150 57	350			005	021	470	440		
1055	65 10	149 35	350			183	211	450	430		
1109	64 53	150 30	350			183	211	450	440		
1115	64 58	151 50	350			011	038	460	450		
1120	64 40	150 52	350			004	032	465	450		
1130	65 26	149 20	350								
1200	64 40	147 06	350								

THIS PAGE IS BEST QUALITY PRACTICABLE
FROM COPY FURNISHED TO DDG

THIS PAGE IS BEST QUALITY PRACTICABLE FROM COPY FURNISHED TO DDC

MISSION: ICE CAP 76-5 EIL/R/W DATE: 4 MARCH 1976													
TIME	LATITUDE N	LONGITUDE W	ALT. FT.	CLAS.	HEADING		SPEED		SOLAR ANGLE		ELEV. FT.	AZIM.	L
					TRUE	MAG	TR. AIR	GND	ELV. FT.	AZIM.			
Z			FL.				RTS	RTS					
0753	64 40	147 06	340		370		770		136.4				
0808	65 00	147 18	350		360		770		136.4				
0824	65 11	147 29	350		350		770		136.4				
0830	65 12	147 30	350		350		770		136.4				
0846	65 22	147 40	350		350		770		136.4				
0858	65 32	147 50	350		350		770		136.4				
0910	65 42	148 00	350		350		770		136.4				
0920	65 52	148 10	350		350		770		136.4				
0930	66 02	148 20	350		350		770		136.4				
0944	66 12	148 30	350		350		770		136.4				
0958	66 22	148 40	350		350		770		136.4				
1012	66 32	148 50	350		350		770		136.4				
1020	66 42	149 00	350		350		770		136.4				
1030	66 52	149 10	350		350		770		136.4				
1044	67 02	149 20	350		350		770		136.4				
1058	67 12	149 30	350		350		770		136.4				
1110	67 22	149 40	350		350		770		136.4				
1124	67 32	149 50	350		350		770		136.4				
1138	67 42	150 00	350		350		770		136.4				
1151	67 52	150 10	350		350		770		136.4				
1201	68 02	150 20	350		350		770		136.4				
1215	68 12	150 30	350		350		770		136.4				
1229	68 22	150 40	350		350		770		136.4				

MISSION: ICE CAP 76-7 EIL/R/W DATE: 4 MARCH 1976													
TIME	LATITUDE N	LONGITUDE W	ALT. FT.	CLAS.	HEADING		SPEED		SOLAR ANGLE		ELEV. FT.	AZIM.	L
					TRUE	MAG	TR. AIR	GND	ELV. FT.	AZIM.			
Z			FL.				RTS	RTS					
0910	64 40	147 06	340		370		770		136.4				
0937	65 06	147 50	330		360		770		136.4				
0951	65 23	148 00	330		360		770		136.4				
1010	65 40	148 08	330		360		770		136.4				
1031	65 50	148 18	330		360		770		136.4				
1042	66 02	148 28	330		360		770		136.4				
1100	66 12	148 38	330		360		770		136.4				
1116	66 22	148 48	330		360		770		136.4				
1136	66 32	148 58	330		360		770		136.4				
1146	66 42	149 08	330		360		770		136.4				
1200	66 52	149 18	330		360		770		136.4				
1212	67 02	149 28	330		360		770		136.4				
1241	67 12	149 38	330		360		770		136.4				
1302	67 22	149 48	330		360		770		136.4				
1340	67 32	149 58	330		360		770		136.4				

MISSION: ICE CAP 76-5 R/V/EIL DATE: 4 MARCH 1976													
TIME	LATITUDE N	LONGITUDE W	ALT. FT.	CLAS.	HEADING		SPEED		SOLAR ANGLE		ELEV. FT.	AZIM.	L
					TRUE	MAG	TR. AIR	GND	ELV. FT.	AZIM.			
Z			FL.				RTS	RTS					
1543	63 54	147 15	370		370		465		172.0				
1612	65 18	147 30	370		370		465		172.0				
1630	65 28	147 40	370		370		465		172.0				
1645	65 38	147 50	370		370		465		172.0				
1700	65 48	148 00	370		370		465		172.0				
1715	65 58	148 10	370		370		465		172.0				
1732	66 08	148 20	370		370		465		172.0				
1745	66 18	148 30	370		370		465		172.0				
1800	66 28	148 40	370		370		465		172.0				
1812	66 38	148 50	370		370		465		172.0				
1830	66 48	149 00	370		370		465		172.0				
1846	66 58	149 10	370		370		465		172.0				
1903	67 08	149 20	370		370		465		172.0				
1915	67 18	149 30	370		370		465		172.0				
1930	67 28	149 40	370		370		465		172.0				
1945	67 38	149 50	370		370		465		172.0				
1958	67 48	150 00	370		370		465		172.0				
2005	67 58	150 10	370		370		465		172.0				
2032	68 08	150 20	370		370		465		172.0				
2045	68 18	150 30	370		370		465		172.0				
2055	68 28	150 40	370		370		465		172.0				
2104	68 38	150 50	370		370		465		172.0				
2125	68 48	151 00	370		370		465		172.0				

MISSION: ICE CAP 76-6 EIL/EIL DATE: 3 MARCH 1976													
TIME	LATITUDE N	LONGITUDE W	ALT. FT.	CLAS.	HEADING		SPEED		SOLAR ANGLE		ELEV. FT.	AZIM.	L
					TRUE	MAG	TR. AIR	GND	ELV. FT.	AZIM.			
Z			FL.				RTS	RTS					
0105	64 40	147 06	370		370		465		172.0				
0136	65 02	147 29	370		370		465		172.0				
0155	65 12	147 39	370		370		465		172.0				
0209	65 22	147 49	370		370		465		172.0				
0225	65 32	147 59	370		370		465		172.0				
0245	65 42	148 09	370		370		465		172.0				
0265	65 52	148 19	370		370		465		172.0				
0285	66 02	148 29	370		370		465		172.0				
0305	66 12	148 39	370		370		465		172.0				
0325	66 22	148 49	370		370		465		172.0				
0345	66 32	148 59	370		370		465		172.0				
0365	66 42	149 09	370		370		465		172.0				
0385	66 52	149 19	370		370		465		172.0				
0405	67 02	149 29	370		370		465		172.0				
0425	67 12	149 39	370		370		465		172.0				
0445	67 22	149 49	370		370		465		172.0				
0465	67 32	149 59	370		370		465		172.0				
0485	67 42	150 09	370		370		465		172.0				
0505	67 52	150 19	370		370		465		172.0				
0525	68 02	150 29	370		370		465		172.0				
0545	68 12	150 39	370		370		465		172.0				
0565	68 22	150 49	370		370		465		172.0				
0585	68 32	150 59	370		370		465		172.0				
0605	68 42	151 09	370		370		465		172.0				
0625	68 52	151 19	370		370		465		172.0				
0645	69 02	151 29	370		370		465		172.0				
0665	69 12	151 39	370		370		465		172.0				
0685	69 22	151 49	370		370		465		172.0				
0705	69 32	151 59	370		370		465		172.0				
0725	69 42	152 09	370		370		465		172.0				
0745	69 52	152 19	370		370		465		172.0				
0765	70 02	152 29	370		370		465		172.0				
0785	70 12	152 39	370		370		465		172.0				
0805	70 22	152 49	370		370		465		172.0				
0825	70 32	152 59	370		370		465		172.0				
0845	70 42	153 09	370		370		465		172.0				
0865	70 52	153 19	370		370		465		172.0				
0885	71 02	153 29	370		370		465		172.0				
0905	71 12	153 39	370		370		465		172.0				
0925	71 22	153 49	370		370		465		172.0				
0945	71 32	153 59	370		370		465		172.0				
0965	71 42	154 09	370		370		465		172.0				
0985	71 52	154 19	370		370		465		172.0				
1005	72 02	154 29	370		370		465		172.0				
1025	72 12	154 39	370		370		465		172.0				
1045	72 22	154 49	370		370		465		172.0				
1065	72 32	154 59	370		370		465		172.0				
1085	72 42	155 09	370		370		465		172.0				
1105	72 52	155 19	370		370		465		172.0				
1125	73 02	155 29	370		370		465		172.0				
1145	73 12	155 39	370		370		465		172.0				
1165	73 22	155 49	370		370		465		172.0				
1185	73 32	155 59	370		370		465		172.0				
1205	73 42	156 09	370		370		465		172.0				
1225	73 52	156 19	370		370		465		172.0				
1245	74 02	156											

THIS PAGE IS BEST QUALITY PRACTICABLE
FROM COPY FURNISHED TO DDG

MISSION: ICE CAP 76-16 EN/UIL DATE: 26 MARCH 1976

TIME	LATITUDE			LONGITUDE			ALT. FT.	DPT. TEMP.	HEADING			SPEED		SOLAR ANGLE	
	N	°	'	W	°	'			TRUE	MAG	TRUE	TR. AIR	GRD	ELEV.	AZIM.
0630	64	40		147	06		310							-13.4	306.9
0648	64	05		149	48				182	209	420	420		-14.8	309.5
0659	62	58		150	00		350	315	181	206	450	420		16.0	310.7
0709	61	51		151	08		350	310	181	206	470	440		-17.2	314.9
0719	61	51		151	08		350	310	359	024	430	440		18.1	314.4
0726	62	42		150	10		350	310	359	024	430	440		18.3	317.2
0730	62	31		150	00		350	310	181	206	450	420		18.8	316.4
0738	61	48		150	35		350	310	181	206	450	420		-14.8	319.6
0740	61	52		151	11		350	310	359	024	430	445		-19.7	319.6
0750	62	58		150	00		350	310	360	027	420	440		-19.9	323.5
0800	64	00		149	45		350	310	360	028	420	440		20.0	327.6
0810	65	06		147	27		350	310	359	028	420	430		-19.9	321.8
0820	66	12		146	02		350	310	359	030	440	455		-14.6	336.0
0830	67	15		144	25		350	310	358	030	440	450		-19.2	340.5
0840	68	18		142	57		350	310	357	031	430	440		-18.7	344.8
0844	-	-	-	-	-	-	350	-	-	-	-	-	-	-	-
0848	68	24		142	24		350	310	171	213	460	440		-18.5	347.4
0851	68	18		142	54		350	310	181	213	470	440		-18.9	347.7
0901	67	18		144	30		350	310	181	212	470	440		-20.0	348.6
0905	66	51		145	10		350	310	-	-	-	-	-	-	-
0915	66	40		147	50		350	310	225	255	425	400		-20.6	348.7
0927	66	28		151	10		350	310	200	222	410	395		-20.2	348.3
0935	65	50		152	10		350	310	180	206	405	390		-21.4	349.1
0940	65	21		152	35		350	310	100	126	405	400		-22.0	350.3
0950	64	42		150	20		350	310	109	150	405	405		-22.9	355.2
0958	62	58		148	55		350	310	182	213	440	435		-33.7	359.1
1008	63	02		149	50		350	310	185	210	455	430		-24.6	360.7
1013	-	-	-	-	-	-	350	-	-	-	-	-	-	-	-
1018	62	48		151	20		350	310	287	313	450	410		-24.8	361.8
1025	62	20		152	25		350	310	270	245	410	390		-14.3	362.6
1034	63	54		154	30		350	310	270	245	410	390		-23.7	362.8
1044	63	47		152	38		350	310	075	100	410	425		-23.7	367.4
1052	63	41		150	33		350	310	050	076	420	425		-23.5	372.0
1058	63	50		148	58		350	310	185	211	450	430		-23.0	375.1
1108	62	59		149	45		350	310	186	212	455	430		-23.6	377.2
1119	61	54		151	18		350	310	210	242	455	430		-24.4	378.7
1127	61	04		151	20		350	310	215	240	480	430		-24.9	380.9
1135	61	09		152	55		350	310	275	299	450	430		-24.8	381.3
1141	61	45		153	04		350	310	005	020	465	470		-24.0	382.7
1153	62	52		150	55		350	310	020	046	420	430		-21.9	387.9
1202	63	43		149	05		350	310	013	040	405	420		-20.5	388.0
1245	64	40		147	06		LAND								

MISSION: ICE CAP 76-17 EN/PSM DATE: 26 MARCH 1976

TIME	LATITUDE			LONGITUDE			ALT. FT.	DPT. TEMP.	HEADING			SPEED		SOLAR ANGLE	
	N	°	'	W	°	'			TRUE	MAG	TRUE	TR. AIR	GRD	ELEV.	AZIM.
0558	64	40		147	06		370							-9.1	399.3
0615	63	40		143	05		290		075	106	450	455		-13.3	396.9
0645	62	48		135	52		290		080	112	458	450		-19.8	321.9
0715	62	44		128	09		290		080	114	450	450		-22.4	327.2
0730	61	50		124	21		290		089	121	450	450		-24.3	345.2
0800	59	58		117	46		390		102	120	450	440		-26.9	361.3
0830	57	52		112	10		330		112	136	465	460		-24.2	366.1
0845	56	18		109	48		330		086	108	460	450		-28.3	323.1
0850	55	26		108	27		330		094	110	462	460		-27.3	326.8
0920	54	22		100	21		330		097	108	465	470		-23.3	345.4
1000	53	22		92	52		330		103	104	470	470		-17.0	358.3
1020	52	26		87	12		330		102	100	460	450		-17.0	371.3
1100	51	43		80	50		330		102	096	460	470		-14.9	382.5
1127	51	03		76	00		330		100	172	460	410		-4.5	392.5
1147	49	59		74	18		330		101	163	465	370		-9.6	396.6
1245	42	05		70	49		LAND								

DISTRIBUTION LIST

DEPARTMENT OF DEFENSE

Director
Defense Advanced Rsch. Proj. Agency
ATTN: LTC W. A. Whitaker
ATTN: Strategic Technology Office
ATTN: Nuclear Monitoring Research

Defense Documentation Center
Cameron Station
12 cy ATTN: TC

Director Defense Nuclear Agency
ATTN: TISI Archives
ATTN: RAAE, MAJ John Clark
ATTN: RAEV, Harold C. Fitz, Jr.
ATTN: DDST
ATTN: RAAE, MAJ James W. Mayo
3 cy ATTN: TITL, Tech. Lib.
2 cy ATTN: RAAE, Charles A. Blank

Commander
Field Command
Defense Nuclear Agency
ATTN: FCPR

Chief
Livermore Divison, Fld. Command DNA
Lawrence Livermore Laboratory
ATTN: FCPRL

Under Secy. of Def. for Rsch. & Engrg.
ATTN: S&SS(OS)

DEPARTMENT OF THE ARMY

Commander/Director
Atmospheric Sciences Laboratory
U.S. Army Electronics Command
ATTN: DELAS-AE-M, F. E. Niles
ATTN: H. Ballard
ATTN: DRSEL-BL-SY-S, D. Snider
ATTN: R. Rosen

Commander
Harry Diamond Laboratories
2 cy ATTN: DELHD-NP, F. N. Wizenitz

Commander
U.S. Army Nuclear Agency
ATTN: MONA-WE, J. Berberet

Director
BMD Advanced Tech. Center
ATTN: ATC-O, W. Davies
ATTN: ATC-T, Melvin T. Capps

Dep. Chief of Staff for Rsch. Dev. & Acq.
ATTN: NCB Division
ATTN: DAMA-CSZ-C
ATTN: Dama-WSZ-C

Chief of Engineers
ATTN: Fernand DePersin

DEPARTMENT OF THE ARMY (Continued)

Dep. Chief of Staff for Ops. & Plans
ATTN: DAMO-DDL, COL. D. W. Einsele
ATTN: Div. of Chem. & Nuc. Ops.

Director
U.S. Army Ballistic Research Labs.
ATTN: Tech. Lib., E. Baicy
ATTN: John Mester
ATTN: J. Heimerl
ATTN: M. Kregl

Commander
U.S. Army Electronics Command
ATTN: DRSEL-PL-ENV, Hans A. Bomke
ATTN: DRSEL
ATTN: Stanley Kronenberg
ATTN: DRSEL-RD-P
ATTN: DRSEL-TL-IR, E. T. Hunter
ATTN: Inst. for Exploratory Rsch.
ATTN: Weapons Effects Section

Commander
U.S. Army Foreign Science & Tech. Ctr.
ATTN: Robert Jones

Commander
U.S. Army Material Dev. & Rdns. Cmd.
ATTN: DRXCD-TL
ATTN: DRCCDC, J. A. Bender

Commander
U.S. Army Missile Command
ATTN: DRSMI-ABL
ATTN: Chief, Doc. Section
ATTN: DRSMI-XS, Chief Scientist

Chief
U.S. Army Research Office
ATTN: CRDARD-CCS, Hermann Robl
ATTN: CRDARD-P, Robert Mace

DEPARTMENT OF THE NAVY

Chief of Naval Research
ATTN: Code 421, B. R. Junker
ATTN: Code 461, Jacob Warner
ATTN: Code 461, R. G. Joiner

Commander
Naval Ocean Systems Center
ATTN: Code 2200 1, Verne E. Hildebrand
ATTN: Code 2200, Ilan Rothmuller
ATTN: Code 2200, Jurgan Richter
ATTN: Code 2200, William F. Moler
ATTN: Code 2200, Richard Pappert
ATTN: Tech. Lib. for T. J. Keary
ATTN: Code 2200, Herbert Hughes

Superintendent (Code 1424)
Naval Postgraduate School
ATTN: Code 2124, Tech. Reports Librarian

DEPARTMENT OF THE NAVY (Continued)

Director

Naval Research Laboratory

ATTN: Douglas P. McNutt
ATTN: Code 7701, Jack D. Brown
ATTN: Code 7709, Wahab Ali
ATTN: Code 7750, Darrell F. Strobel
ATTN: Code 7700, Timothy P. Coffey
ATTN: Code 7750, Paul Julienne
ATTN: Code 2600, Tech. Lib.
ATTN: Code 7127, Charles Y. Johnson
ATTN: Code 7120, W. Neil Johnson
ATTN: Code 7750, J. Davis
ATTN: Code 7750, Klaus Hein
ATTN: Code 7750, Joel Feddler
ATTN: Code 2027, Tech. Lib.
ATTN: Code 7750, S. L. Ossakow
ATTN: Code 7730, Edgar S. McClean

Officer-in-Charge

Naval Surface Weapons Center

ATTN: Code WA501, Navy Nuc. Prgms. Off.
ATTN: Code WX21, Tech. Lib.
ATTN: D. J. Sand
ATTN: L. Rudlin

Commanding Officer

Naval Intelligence Support Center

ATTN: Doc. Con.
ATTN: Code 40A, E. Blase

Commander

Naval Weather Service Command

ATTN: Mr. Martin

DEPARTMENT OF THE AIR FORCE

AF Geophysics Laboratory, AFSC

5 cy ATTN: OPR, Alva T. Stair
5 cy ATTN: LKB, Kenneth S. W. Champion
2 cy ATTN: OPR-1, R. Murphy
2 cy ATTN: OPR-1, J. Kennealy
5 cy ATTN: OPR, J. Ullwick

AF Weapons Laboratory, AFSC

ATTN: CA
ATTN: Col G. J. Freyer
2 cy ATTN: DYM
5 cy ATTN: DYC
5 cy ATTN: SUL
5 cy ATTN: DYT

Commander

ASD

ATTN: ASD-YH-EX, Lt Col Robert Leverette

SAMSO/SZ

ATTN: SZJ, Maj Lawrence Doan

AFTAC

5 cy ATTN: TD
2 cy ATTN: Tech. Lib.

Hq. USAF

ATTN: DLS
ATTN: DLCAW
ATTN: DTL
ATTN: DLXP
ATTN: SDR
ATTN: Tech. Lib.

DEPARTMENT OF THE AIR FORCE (Continued)

SAMSO/AW

ATTN: AW

DEPARTMENT OF ENERGY

Division of Military Application

ATTN: Doc. Con. for Major D. A. Haycock
ATTN: Doc. Con. for Colonel T. Gross
ATTN: Doc. Con. for David Slade
ATTN: Doc. Con. for Donald I. Gale
ATTN: Doc. Con. for F. S. Ross

Los Alamos Scientific Laboratory

ATTN: Doc. Con. for R. A. Jeffries
ATTN: Doc. Con. for C. R. Mehl
ATTN: Doc. Con. for G. Rood
ATTN: Doc. Con. for H. V. Sego
ATTN: Doc. Con. for D. Steinhaus
ATTN: Doc. Con. for J. Judd
ATTN: Doc. Con. for T. Bieniewski
ATTN: Doc. Con. for D. M. Rohrer
ATTN: Doc. Con. for Martin Tierney
ATTN: Doc. Con. for Marge Johnson
ATTN: Doc. Con. for John S. Malik
ATTN: Doc. Con. for William Maier
ATTN: Doc. Con. for S. Rockwood
ATTN: Doc. Con. for Donald Kerr
ATTN: Doc. Con. for W. D. Barfield
ATTN: Doc. Con. for Reference Library
ATTN: Doc. Con. for W. M. Hughes
ATTN: Doc. Con. for E. W. Jones, Jr.
ATTN: Doc. Con. for John Zinn
ATTN: Doc. Con. for E. S. Bryant

University of California

Lawrence Livermore Laboratory

ATTN: G. R. Haugen
ATTN: A. Kaufman
ATTN: D. J. Wuebbles
ATTN: J. F. Tinney
ATTN: Julius Chang
ATTN: Tech. Info. Dept.
ATTN: W. H. Duewer

Sandia Laboratories

ATTN: Doc. Con. for W. D. Brown
ATTN: Doc. Con. for Org. 9220
ATTN: Doc. Con. for Craig Hudson
ATTN: Doc. Con. for J. C. Eckardt
ATTN: Doc. Con. for C. W. Gwyn
ATTN: Doc. Con. for D. A. Dahlgren
ATTN: Doc. Con. for M. L. Kramm
ATTN: Doc. Con. for T. Wright
ATTN: Doc. Con. for Charles Williams
ATTN: Doc. Con. for Sandia Rpt. Coll.
ATTN: Doc. Con. for Doc. Con. Div.

Sandia Laboratories

Livermore Laboratory

ATTN: Doc. Con. for Thomas Cook

Department of Energy

Div. of Hqs. Services, Library Branch, G-043

ATTN: Doc. Con. for D. Kohlsted
ATTN: Doc. Con. for J. D. LaFleur
ATTN: Doc. Con. for Class. Tech. Lib.
ATTN: Doc. Con. for George Regosa
ATTN: Doc. Con. for Rpts. Section
ATTN: Doc. Con. for R. Kandel
ATTN: Doc. Con. for H. H. Kurzweg

DEPARTMENT OF ENERGY (Continued)

Argonne National Laboratory
Records Control

ATTN: Doc. Con. for A. C. Wall
ATTN: Doc. Con. for S. Gabelnick
ATTN: Doc. Con. for J. Berkowitz
ATTN: Doc. Con. for Lib. Svcs. Rpts. Sec.
ATTN: Doc. Con. for Len Liebowitz
ATTN: Doc. Con. for David W. Green
ATTN: Doc. Con. for Gerald T. Reedy

OTHER GOVERNMENT AGENCY

Department of Commerce
Office of Telecommunications
Institute for Telecom Science
ATTN: William F. Utlaut

DEPARTMENT OF DEFENSE CONTRACTORS

Aero-Chem Research Laboratories, Inc.
3 cy ATTN: A. Fontijn

Aerodyne Research, Inc.
ATTN: M. Camac
ATTN: F. Bien

Aerospace Corporation
ATTN: Harris Mayer
ATTN: Thomas D. Taylor
ATTN: R. D. Rawcliffe
ATTN: R. Grove
ATTN: R. J. McNeal

University of Denver
Colorado Seminary
Denver Research Institute
ATTN: Sec. Officer for Mr. Van Zyl
ATTN: Sec. Officer for David Murcay

General Electric Company
TEMPO-Center for Advanced Studies
ATTN: Warren S. Knapp
5 cy ATTN: DASIAC, Art Feryok

General Research Corporation
ATTN: John Ise, Jr.

Geophysical Institute
University of Alaska
ATTN: T. N. Davis
3 cy ATTN: Neal Brown

Honeywell Incorporated
Radiation Center
ATTN: W. Williamson

HSS Incorporated
ATTN: A. H. Tuttle

Institute for Defense Analyses
ATTN: Hans Wolfhard
ATTN: Ernest Bauer

DEPARTMENT OF DEFENSE CONTRACTORS (Continued)

Lockheed Missiles and Space Co. Inc.
ATTN: Billy M. McCormac, Dept. 52-54
ATTN: John B. Cladis, Dept. 52-12
ATTN: J. B. Reagan, Dept. 52-12
ATTN: John Kumer
ATTN: Martin Walt, Dept. 52-10
ATTN: Richard G. Johnson, Dept. 52-12
ATTN: Robert D. Sears, Dept. 52-14
ATTN: Tom James

Mission Research Corporation
ATTN: P. Fischer
ATTN: D. Archer

Photometrics, Inc.
3 cy ATTN: I. L. Kofsky/D. P. Villanucci/G. Davidson

Physical Dynamics, Inc.
ATTN: Joseph B. Workman

Physical Sciences, Inc.
ATTN: Kurt Wray

R & D Associates
ATTN: Robert E. Lelevier
ATTN: Forrest Gilmore

R & D Associates
ATTN: Herbert J. Mitchell

Science Applications, Inc.
ATTN: Daniel A. Hamlin

Space Data Corporation
ATTN: Edward F. Allen

SRI International
ATTN: M. Baron
ATTN: Ray L. Leadabrand
ATTN: Walter G. Chesnut

SRI International
ATTN: Warren W. Berning

Technology International Corporation
ATTN: W. P. Boquist

Utah State University
ATTN: D. Burt
ATTN: Kay Baker
ATTN: C. Wyatt
ATTN: Doran Baker

Visidyne, Inc.
ATTN: L. Katz
ATTN: William Reidy
ATTN: Henry J. Smith
ATTN: Charles Humphrey
ATTN: J. W. Carpenter
ATTN: T. C. Degges